Instabilities and elastic waves in microstructured soft composites

Jian Li

Instabilities and elastic waves in microstructured soft composites

Research thesis

In Partial Fulfillment of the Requirements for the Degree of Doctor of Philosophy

Jian Li

Submitted to the Senate of the Technion - Israel Institute of Technology

Elul 5778, August 2019, Haifa

The Research Thesis was Done
Under the Supervision of Stephan Rudykh
in the Faculty of Aerospace Engineering

Acknowledgements

I would like to thank my parents, Youhua and Pingchang, and my sister Yuan for their unconditional encouragement and support. I would like to thank my wife Shu Dai and our son Junnan for their endless love.

I would like to express my deepest gratitude to Stephan Rudykh, for his professional guidance, constant encouragement and support throughout my doctoral studies.

I would like to thank Viacheslav Slesarenko, Pavel I. Galich, Tarkes Dora Pallicity, and Artemii Goshkoderia for fruitful discussions.

I would like to thank the Faculty of Aerospace Engineering, especially the support from Dean Itzchak Frankel.

The generous financial help of the Technion – Israel Institute of Technology and the Lady Davis Fellowship is gratefully acknowledged.

The research was partially supported by the Israel Science Foundation.

List of publications

1. Li J, Slesarenko V, Rudykh S. Microscopic instabilities and elastic wave propagation in finitely deformed laminates with compressible hyperelastic phases. Eur J Mech - A/Solids 2019;73:126–36.
2. Li J, Slesarenko V, Galich PI, Rudykh S. Instabilities and pattern formations in 3D-printed deformable fiber composites. Compos Part B Eng 2018;148:114–22.
3. Li J, Pallicity TD, Slesarenko V, Goshkoderia A, Rudykh S. Domain Formations and Pattern Transitions via Instabilities in Soft Heterogeneous Materials. Adv Mater 2019;31:1807309.
4. Li J, Slesarenko V, Rudykh S. Auxetic multiphase soft composite material design through instabilities with application for acoustic metamaterials. Soft Matter 2018;14:6171–80.
5. Li J, Rudykh S. Tunable microstructure transformations and auxetic behavior in 3D-printed multiphase composites: The role of inclusion distribution. Compos Part B Eng 2019;172:352–62.
6. Li J, Slesarenko V, Galich PI, Rudykh S. Oblique shear wave propagation in finitely deformed layered composites. Mech Res Commun 2018;87:21–8.

Contents

Abstract **1**

List of abbreviations **3**

1 Preamble **4**

1.1 Elastic instability 5

1.1.1 Hyperelastic fiber composites 5

1.1.2 Soft porous materials 7

1.2 Elastic wave propagation in soft materials 10

1.2.1 Homogeneous materials 10

1.2.2 Periodic composites 11

1.3 Methodology 14

1.3.1 Nonlinear elasticity 14

1.3.2 Small amplitude motions superimposed on large deformation 15

1.3.3 Bloch-Floquet analysis for elastic waves in finitely deformed periodic composites 16

1.3.4 Bloch-Floquet instability analysis and post-buckling analysis 18

2 Microscopic instabilities and elastic wave propagation in finitely deformed laminates with compressible hyperelastic phases 20

2.1 Introduction 21

2.2 Simulations 24

2.3 Results and discussion 26

2.3.1 Instabilities in finitely deformed compressible layered composite 26

2.3.2 Elastic waves in finitely deformed compressible layered composite 34

2.4 Summary 45

3 Instabilities and pattern formations in 3D fiber composites 47

3.1 Introduction 48

3.2 Experiments and simulations 51

3.3 Results and discussion 53

3.3.1 Buckling of a single stiff fiber embedded in a soft matrix 53

3.3.2 Buckling of composites with periodically distributed fibers 59

3.4 Summary 65

4 Domain formations and pattern transitions via instabilities in soft heterogeneous materials 67

4.1 Introduction 68

4.2 Experiments and simulations 69

4.3 Results and discussion 71

4.4 Summary 82

5 Instability-induced pattern transformations in multiphase soft composites 84

5.1 Introduction 85

5.2 Experiments and simulations 86

5.3 Results and discussion 88

5.4 Summary 99

6 Tunable microstructure transformations and auxetic behavior in multiphase composites: the role of inclusion distribution 100

6.1 Introduction 101

6.2 Specimen design and fabrication, and experimental testing 104

6.3 Simulations 106

6.4 Results and discussion 109

6.5 Summary 123

7 Oblique wave propagation in finitely deformed layered composite 125

7.1 Introduction 126

7.2 Simulations 128

7.3 Results and discussion 131

7.4 Summary 139

8 Conclusions and discussion 141

Appendix **146**

A. Approximation of the effective stiffness K of Winkler foundation model for incompressible material 147

B. The energy landscape and instability of particulate composite 151

C. Visualization of deformed configuration 155

D. Effect of matrix volume fraction on composite effective Young's modulus 156

E. Evaluation of Poisson's ratio 157

F. Calculation of the effective Poisson's ratio 158

G. Comparisons of long wave estimates and Bloch wave numerical analyses .. 160

Bibliography 162

Abstract

This thesis presents a study of elastic instabilities and small-amplitude elastic waves in microstructured soft composites undergoing large deformations. Macroscopic and microscopic instabilities in soft composites with periodic microstructures are detected through numerical Bloch-Floquet analysis, and experiments on 3D-printed samples. In this thesis, I investigated the instabilities in periodic microstructured soft systems including

(i) Layered composites: I examined the role of phase compressibility on the onset of instability in compressible layered composites. I found that compressible layered composites require larger strains to trigger mechanical instabilities.

(ii) 3D fiber composite: I studied the elastic instabilities in 3D fiber composites with various fiber distributions. In periodically distributed fiber composites with the square in-plane periodicity, I experimentally observed that an increase in fiber volume fraction can result in a transition of the instability-induced patterns from small wavelength wavy pattern to the long-wave mode. I found that the composites with rectangular fiber periodicity exhibit cooperative buckling mode developing in the direction, where the fibers are closer to each other. Moreover, I derived a closed-form expression to predict the dependence of buckled wavelength on shear modulus contrast for single fiber composite.

(iii) Particulate composite: I investigated instability-induced domain formations and pattern transitions in particulate composites with stiff inclusions periodically embedded in a soft elastomeric matrix. I experimentally observed that the formation

of microstructures with antisymmetric domains, and their geometrically tailored evolution into cooperative patterns of inclusions rearranged in wavy chains. I found that the domain patterns are realized in the composites for which macroscopic instabilities are predicted. I showed that these switchable patterns can be tailored by tuning composite microstructures.

(iv) Auxetic multiphase composite: I considered the instability phenomena in multiphase composites consisting of circular voids and stiff inclusions periodically distributed in a soft elastomer. I experimentally realized instability-induced pattern transformations in 3D-printed composites. I observed that composite microstructures rearrange into new morphologies, resulting in the closure of voids and giving rise to auxetic behaviors. I showed that distinct new patterns and auxetic behaviors can be tailored through altering the distribution of inclusions and loading direction.

Furthermore, I illustrated an application of employing instability-induced pattern transformations to manipulate small-amplitude elastic wave propagation. I showed that the buckled patterns in multiphase composites open new band gaps in remarkable low-frequency ranges. I found that the instability-induced wavy patterns give rise to the tunability of the widths and locations of shear wave band gaps in neo-Hookean laminates. Finally, I examined the oblique shear wave propagation in the finitely deformed layered composites. I observed the closure of band gaps in layered composites when the propagation direction deviates – even slightly – from the normal (i.e., perpendicular to the layer) direction.

List of abbreviations

BG – Band gap

CCD – Charge-coupled device

DM – Digital material

IBZ – Irreducible Brillouin zone

LC – Layered composite

NPR – Negative Poisson’s ratio

PBG – Pressure wave band gap

SBG – Shear wave band gap

TP – TangoPlus

Chapter 1

Preamble

Soft composites can develop large deformations in response to various external stimuli [1–5], thus providing rich opportunities for the design of responsive and reconfigurable materials. Moreover, the performance of soft composites can be further empowered via the instability phenomenon giving rise to dramatic microstructural changes. This approach holds the potential for applications in vibration mitigation [6], flexible electronics [7], sensors [8], actuators [9], and adhesive systems [10]. Motivated by the fundamental understanding of the underlying phenomena, this thesis examines elastic instabilities in microstructured soft composites. In particular, the instability phenomena in (i) layered composites [11], (ii) 3D fiber composites [12], (iii) particulate composites [13] and (iv) multiphase composites [14,15] are investigated. Moreover, this thesis illustrates the potential applications of employing large deformations to manipulate small-amplitude elastic wave propagation in these soft materials [11,14,16].

1.1 Elastic instability

Elastic instability is historically associated with the failure that should be prevented in engineering designs [17]. Recently, however, the concept of harnessing elastic instabilities to enable novel materials and systems has emerged [18]. Thus, for example, instability-induced pattern transformations in periodic porous elastic structures have been utilized for the design of auxetic materials [19], acoustic switches [20], and soft robotics [21].

1.1.1 Hyperelastic fiber composites

The study of elastic instabilities in periodic fiber composites was pioneered by Rosen [22], who derived an explicit formula to predict the buckling strain of linear layered composite. Triantafyllidis and Maker [23] investigated the instabilities in periodic layered composites with hyperelastic phases. They pointed out the instability can develop at the microscopic scale and macroscopic scale; here, the macroscopic scale refers to the length scale that is significantly larger than the characteristic size of the composite microstructure. Parnes and Chiskis [24] re-examined the instability analysis in linear elastic layered composites. They found that the buckling strain of dilute composites that experience the microscopic instability is constant, while for the non-dilute case (with macroscopic instability), the predicted buckling strain agrees with the result of Rosen [22]. Nestorovic and Triantafyllidis [25] investigated the interplay between macroscopic and microscopic instability of hyperelastic layered media subjected to combinations of shear and compression deformation. Geymonat et al. [26] established a rigorous theoretical foundation for microscopic instability analysis in periodic composites with the help of Bloch wave analysis [27]. They also connected the specific case of the long-wave limit with the macroscopic loss of ellipticity analysis. Qiu and Pence [28], Merodio and Ogden [29–31] employed the loss of ellipticity analysis to examine the macroscopic instabilities in fiber-reinforced nonlinearly elastic solids under plane deformation. Merodio and Ogden [32,33] also showed that the loss of ellipticity may occur in the fiber-reinforced transversely isotropic material model even under tensile deformations. Moreover, Volokh [34] examined the loss of ellipticity in hyperelastic solids with energy limiters.

Recently, Li et al. [35] experimentally realized the instability-induced wrinkles in multilayered composites under plan strain conditions via 3D-printed specimens. Slesarenko and Rudykh [36] showed that the wavy pattern in layered composite with viscoelastic constitutes can be tuned by varying the strain-rate. Slesarenko and Rudykh [37] examined the macroscopic and microscopic stabilities in periodic 3D fiber composites by means of the Bloch-Floquet finite-element-based analysis. More recently, Li et al. [11] examined the stability of compressible hyperelastic laminates. They found that the compressible laminates require larger strains to trigger the mechanical instability in comparison to the laminates with incompressible phases. Moreover, Li et al. [12] experimentally investigated the role of fiber distribution on the instabilities in 3D fiber composites. In periodically distributed fiber composites with square in-plane periodicity, they experimentally observed the transition of the instability-induced patterns from small wavelength wavy pattern to the long-wave mode. This transition happens with an increase in fiber volume fraction in 3D-printed samples. They also found that the composites with rectangular fiber periodicity exhibit cooperative buckling mode developing in the direction, where the fibers are closer to each other. Very recently, Li et al. [13] reported the instability-induced domain formations and their pattern transitions in periodic particulate composites. Li et al. [13] observed the formation of antisymmetric domains in experiments, and they studied the evolution of instability-induced patterns into the cooperatively wavy patterns. The domain formations were observed in the composites for which macroscopic instabilities are predicted by the Bloch-Floquet analysis.

1.1.2 Soft porous materials

Elastic instabilities can also occur in soft porous materials subjected to large deformation, resulting in the formation of various patterns (as shown in Figure 1). Abeyaratne and Triantafyllidis [38] predicted macroscopic instabilities in periodic soft porous materials by the loss of ellipticity analysis. Mullin et al. [39] experimentally realized instability-induced pattern transformations in porous composites with a square array of circular voids periodically embedded in an elastomer subjected to a uniaxial compressive deformation. They observed that, upon the onset of the microscopic instability, the circular voids suddenly evolve into ellipses arranged in a mutually orthogonal configuration. It is worth noting that Triantafyllidis et al. [40] numerically calculated similar buckling modes in periodic inclusion composites when the inclusions are highly compressible, and the matrix is significantly stiffer than the inclusions. Moreover, these pattern transformations were also realized at micrometer length scale in polymer structures fabricated by interference lithography [41–43].

Based on the realized pattern in the soft porous material with a square array of circular voids, various additional patterns were obtained through altering the distribution [19] and shape [44,45] of voids, and changing the loading direction [6].

Furthermore, Babaee et al. [46] investigated the pattern transformations in structure with holes arranged on the spherical shell, as well as the associated auxetic behaviors. Shim [47] studied the structural evolution in Buckliball induced by buckling under pressure loading. Florijn et al. [48,49] proposed a bi-void system comprising of larger and smaller circular voids; they showed that the composite stress-strain behavior can be designed to be monotonic, nonmonotonic, and hysteretic through altering the size of the holes and lateral confinement. Recently, Overvelde et al. [50] realized the checkerboard pattern in soft metamaterial comprising a square array of circular voids triggered by equibiaxial tensile deformation. More recently, Li et al. [14] proposed the design of *multiphase* composites with stiff inclusions and voids distributed periodically in a soft matrix. They experimentally illustrated that the anisotropic property of the composite can be used to achieve distinct new patterns. These distinct patterns are characterized by significantly different auxetic behaviors in the postbuckling regime. They also investigated the role of inclusion distribution on the behavior of the proposed transformative multiphase composite, and showed that the tailored positioning of the stiff inclusions can be exploited to expand the set of admissible switchable patterns [15]. Very recently, Li et al. [51] showed that the porous structure with proper positioning of stiff inclusions can enhance the robustness of the development of the buckled patterns.

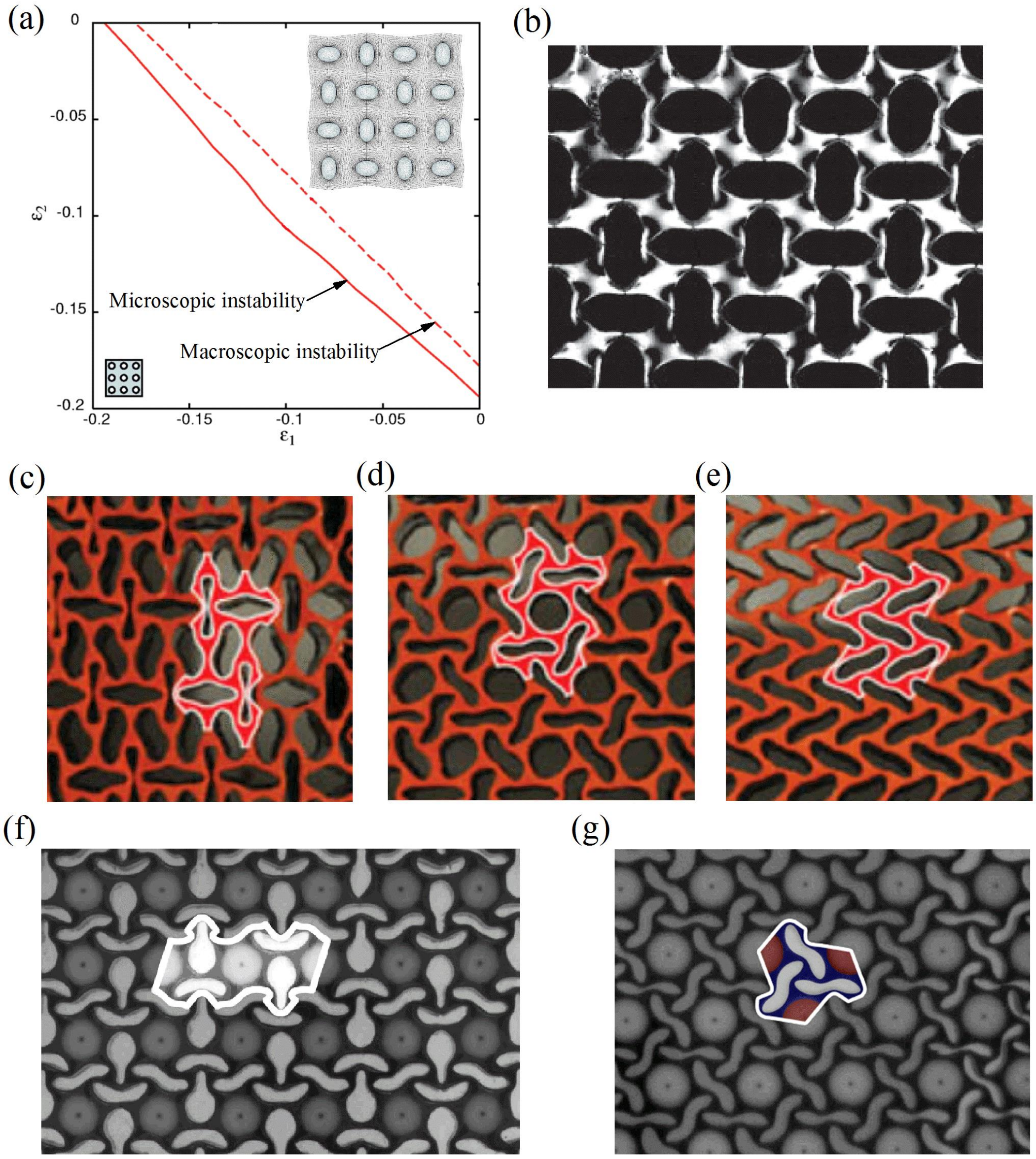

Figure 1. Instability-induced pattern formations in periodic porous materials. (a) Macroscopic and microscopic instabilities in inclusion composites (matrix-to-inclusion modulus ratio equal to 50) with a square distribution of inclusions, the inset illustrates the eigenmode of the microscopic instability for the composite undergoing equibiaxial compression deformation (Adapted from Reference [40]). (b) Pattern formation in the composite with a square array of circular voids embedded in a soft matrix (Adapted from Reference [39]). (c-e) Multiple patterns in a porous elastomeric structure comprising of a triangular array of circular voids (Adapted from Reference [6]). (f, g) Distinct patterns in multiphase composites (Adapted from Reference [14] (f) and Reference [15] (g)).

1.2 Elastic wave propagation in soft materials

In addition to investigating the elastic instabilities, this thesis explores the potential application of the elastic instability phenomena for the control of elastic waves.

1.2.1 Homogeneous materials

The study of small amplitude elastic wave propagation in finitely deformed homogeneous isotropic materials was pioneered by Biot [52], who investigated the influence of initial stress on elastic wave propagation. Hayes and Rivlin [53] examined the propagation of plane waves in deformed isotropic elastic materials and connected the eigenvalue of the secular equation determined wave propagation velocity with material instability. Then, Currie and Hayes [54] pointed out incompressible Mooney-Rivlin material can sustain two shear waves with polarization directions orthogonal to each other, and the corresponding propagation velocities were obtained by Boulanger and Hayes [55]. Later, Boulanger et al. [56] extended these results to a more general class of compressible Hadamard materials, and derived the explicit formulas to calculate the phase velocities of pressure and shear waves. Recently, Galich and Rudykh [57] studied the elastic wave propagation in Gent material with significant stiffening effect under large deformations. They showed that phase velocities of shear and pressure waves significant depend on the propagation direction and applied deformation in highly compressible materials. The dependence of the shear wave velocity on deformation was utilized to decouple the entangled shear and pressure waves in isotropic hyperelastic material [58,59].

1.2.2 Periodic composites

Propagation of small amplitude elastic waves in periodic composite materials is characterized by its dispersion relations (frequency vs. wavenumber). Remarkably, periodic composites with certain microstructures possess the so-called stop bands (as shown in Figure 2), i.e., the frequency ranges where the waves cannot propagate. For example, Kushwaha et al. [60] calculated the dispersion relation of small amplitude elastic waves in periodic linear elastic composites (without pre-stress nor deformation). They reported the existence of the *omnidirectional band gaps*, in which the out-of-plane shear (transverse) wave cannot propagate in all directions. It is worth noting that Kushwaha et al. [60] identified the omnidirectional band gaps through examining the *full area* of the irreducible Brillouin zone (IBZ). It is very common in the current literature, to report the omnidirectional band gaps based on the limited scanning of the *edges* of the irreducible Brillouin zone only [6,20,61,62]. The limited IBZ edge scanning, however, does not guarantee that the detected band gaps are omnidirectional [63]. Rytov [64] studied the elastic waves propagating in layered composites with linear phases (without pre-stress nor pre-strain), and derived the dispersion relations for shear and pressure waves propagating perpendicular and parallel to the layers. Galich et al. [65] extended Rytov's solutions [64] to the finitely deformed layered composite with hyperelastic phases. They showed that shear wave band gaps in the composites with neo-Hookean phases are independent of applied deformation. The locations and widths of pressure wave band gaps can be significantly tuned by deformations. Li et al. [16] investigated the oblique shear wave propagation in the finitely deformed layered composites. They found that band gaps close suddenly when the propagation direction deviates – even slightly – from the normal (i.e., perpendicular to the layer) direction. For shear waves traveling along the layer direction, Li et al. [16] showed that the dispersion curves of oblique shear waves possess two linear (a) short and (b) longwave ranges. The applied tensile deformation along layer direction shifts the dispersion curves towards higher frequencies in linear short wave ranges. Moreover, Slesarenko et al. [66] revealed the existence of negative group velocity in the soft composites in the marginally stable regime near elastic instabilities.

The tunability of elastic waves in periodic soft composites can be further amplified via instability-induced microstructure transformations. This concept was first illustrated by Bertoldi and Boyce [67,68]; they showed that the locations and widths of the band-gaps can be tuned by the instability-induced pattern transformations in periodically structured elastomeric materials. Wang et al. [69] investigated the role of deformation-induced changes in microstructures and local material properties on the response of the tunable band gaps in the structure with a square array of circular voids embedded in a soft elastomer. They found that the tunability of band gaps in this particular structure is mainly contributed by deformation-induced structural changes. The band gaps in soft composites with periodically distributed circular voids can be also enriched through different pattern transformations, achieved by altering the loading direction [6] or the distribution of voids [20]. Li et al. [14] investigated the

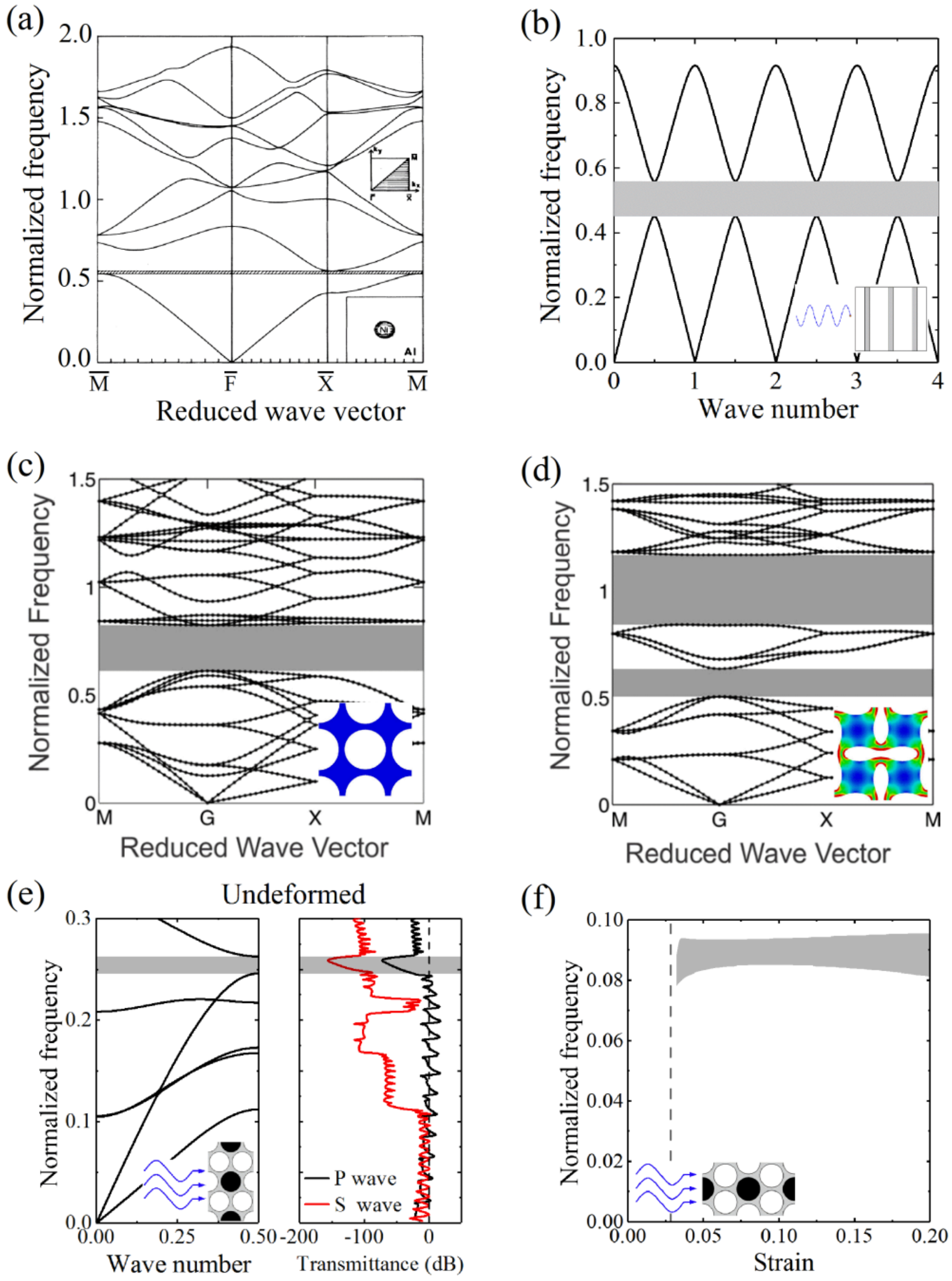

Figure 2. Dispersion diagrams of periodic composites: (a) Particulate composites (Adapted from Reference [60]), (b) Laminate composites (Adapted from Reference [16]), (c, d) Porous materials (Adapted from Reference [69]). (e) Dispersion diagrams and transmittance spectra of multiphase composites (Adapted from Reference [14]). (f) Evolution of band gaps as a function of the applied strain for multiphase composites (Adapted from Reference [14]).

elastic wave propagation in multiphase composite consisting of stiff inclusions and voids periodically distributed in a soft matrix. They showed that the instability induced microstructure switches give rise to the opening of the new band gap in remarkable low-frequency ranges. Moreover, Li et al. [11] showed that instability-induced wavy patterns in neo-Hookean laminates give rise to the tunability of the widths and locations of shear wave band gaps (that are not tunable by the applied deformation along the layer direction in neo-Hookean laminate in the stable regime [65]).

1.3 Methodology

1.3.1 Nonlinear elasticity

Consider a continuum body and identify each point in the undeformed configuration with its position vector **X**. When the body is deformed, the new location **x** is defined by the mapping function

$$\mathbf{x} = \boldsymbol{\chi}(\mathbf{X}, t), \tag{1}$$

so the deformation gradient is

$$\mathbf{F} = \partial \mathbf{x} / \partial \mathbf{X}, \tag{2}$$

and its determinant is

$$J \equiv \det(\mathbf{F}). \tag{3}$$

Physically, J is the volume ratio between the representative element in the deformed and undeformed configurations, thus $J > 0$.

Consider a hyperelastic material whose constitutive behavior is described in terms of strain energy density function $W(\mathbf{F})$ such that the first Piola-Kirchhoff stress tensor is given by

$$\mathbf{P} = \frac{\partial W(\mathbf{F})}{\partial \mathbf{F}}. \tag{4}$$

For incompressible materials, Eq. (4) is modified as

$$\mathbf{P} = \frac{\partial W(\mathbf{F})}{\partial \mathbf{F}} - p\mathbf{F}^{-\mathrm{T}}, \tag{5}$$

where p is the Lagrange multiplier defined by incompressibility constraint $\det(\mathbf{F}) = 1$.

In the absence of body forces, the equations of motion can be written in the undeformed configuration as

$$\mathrm{Div}\,\mathbf{P} = \rho_0 \frac{D^2\boldsymbol{\chi}}{Dt^2}, \tag{6}$$

where Div(•) represents the divergence operator in the undeformed configuration, $D(\bullet)/Dt$ is the material time derivative, and ρ_0 denotes the initial material density. When deformation is applied quasi-statically, Eq. (6) reads

$$\mathrm{Div}\,\mathbf{P} = \mathbf{0}. \tag{7}$$

1.3.2 Small amplitude motions superimposed on large deformation

Consider small amplitude motions superimposed on a deformed equilibrium state [70]. The equations of the incremental motion are

$$\mathrm{Div}\,\dot{\mathbf{P}} = \rho_0 \frac{D^2\,\dot{\mathbf{u}}}{Dt^2}, \tag{8}$$

where $\dot{\mathbf{P}}$ is an incremental change in the first Piola-Kirchhoff stress tensor and $\dot{\mathbf{u}}$ is an incremental displacement. The incremental change in the deformation gradient is given by

$$\dot{\mathbf{F}} = \mathrm{Grad}\,\dot{\mathbf{u}}, \tag{9}$$

where Grad (•) represents the gradient operator in the undeformed configuration.

The linearized constitutive law can be expressed as

$$\dot{P}_{ij} = \mathcal{A}_{0ijkl}\dot{F}_{kl}, \tag{10}$$

where $\mathcal{A}_{0ijkl} = \partial^2 W / \partial F_{ij}\, \partial F_{kl}$ is the tensor of elastic moduli. Substitution of Eq. (9) and (10) into Eq. (8) yields

$$\mathcal{A}_{0ijkl}\frac{\partial^2 \dot{u}_k}{\partial X_j \partial X_l} = \rho_0 \frac{D^2 \dot{u}_i}{Dt^2}. \tag{11}$$

In the updated Lagrangian formulation, Eq. (11) reads

$$\mathcal{A}_{ijkl}\frac{\partial^2 \dot{u}_k}{\partial x_j \partial x_l} = \rho \frac{\partial^2 \dot{u}_i}{\partial t^2}, \tag{12}$$

where $\mathcal{A}_{ipkq} = J^{-1}\mathcal{A}_{0ijkl}F_{pj}F_{ql}$ and $\rho = J^{-1}\rho_0$.

1.3.3 Bloch-Floquet analysis for elastic waves in finitely deformed periodic composites

To investigate small-amplitude elastic waves propagating in finitely deformed periodic composites, the Bloch-Floquet techniques superimposed on the deformed state is utilized to obtain the corresponding dispersion relations [27,68]. This approach is implemented in the finite element code COMSOL. In particular, the analysis is performed in two steps:

Step 1: Quasi-static analysis to obtain the deformed state

To obtain the static response of periodic structural composites under macroscopic large deformation, periodic displacement boundary conditions are imposed on the edges of the unit cell to obtain the deformed state; the periodic boundary conditions are

$$\mathbf{u}_B - \mathbf{u}_A = (\bar{\mathbf{F}} - \mathbf{1})(\mathbf{X}_B - \mathbf{X}_A), \tag{13}$$

where *A* and *B* are the paired nodes periodically located at the opposite edges of the unit cell; $\mathbf{u} = \mathbf{x}(\mathbf{X}) - \mathbf{X}$ is the displacement field; $\bar{\mathbf{F}}$ is the applied macroscopic deformation gradient. Based on this defined periodic boundary conditions, the deformed state is obtained through solving the equilibrium equation in the absence of body force stemming from Eq. (7).

Step 2: Bloch wave analysis superimposed on deformed state

Consider small amplitude waves superimposed on finitely deformed state, the corresponding incremental motions can be described as

$$\dot{\mathbf{u}}(\mathbf{X}, t\,) = \tilde{\mathbf{u}}(\mathbf{X})e^{-i\omega t}, \tag{14}$$

where $\tilde{\mathbf{u}}$ and ω denote the magnitude and angular frequency of the wave, respectively.

Based on the linearized constitutive Eq. (10), the incremental first Piola-Kirchhoff stress can be given by

$$\dot{\mathbf{P}}(\mathbf{X}, t\,) = \tilde{\mathbf{P}}(\mathbf{X})e^{-i\omega t}. \tag{15}$$

Substitution of Eq. (14) and Eq. (15) into Eq. (8) yields

$$\mathrm{Div}\,\tilde{\mathbf{P}} + \rho_0\omega^2\tilde{\mathbf{u}} = \mathbf{0}, \tag{16}$$

Moreover, according to the Bloch's theorem, small amplitude elastic waves propagation in periodic structures must satisfy the Bloch-Floquet conditions [27]

$$\tilde{\mathbf{u}}(\mathbf{X} + \mathbf{R}) = \tilde{\mathbf{u}}(\mathbf{X})e^{-i\mathbf{K}\cdot\mathbf{R}}, \tag{17}$$

where **R** defines the distance between the paired nodes on the opposite edges of the unit cell; $\mathbf{K}$ is the wave vector. Thus, based on the Bloch-Floquet displacement boundary conditions superimposed on the edges of the deformed unit cell (defined by Eq. (17)), the dispersion relation for finitely deformed periodic composite is obtained through solving the eigenvalue problem stemming from Eq. (16) for a range of wave vectors **K**.

1.3.4 Bloch-Floquet instability analysis and post-buckling analysis

Elastic instabilities in infinite periodic composites subjected to large deformations can occur at the microscopic levels, as well as macroscopic levels. The detection of microscopic instability can be performed by employing Bloch wave analysis superimposed on deformed primitive unit cell [26,68,71]. Through gradually increasing the applied averaged macroscopic deformation (defined in Eq. (13)), and solving the eigenvalue problem for the unit cell with defined Bloch-Floquet conditions (defined in Eq. (17)) superimposed on each deformation level for a range of wavenumbers $\mathbf{K}$, the microscopic instability is detected when a non-trivial zero eigenvalue is first identified at a non-zero wavenumber along the loading path, thus the corresponding applied deformation level and non-zero wavenumber are identified as the critical strain ε_{cr} and critical wavenumber $\mathbf{K}_{cr}$ [26,68]. In the limit of long-wave mode or macroscopic instability, it can be detected by performing the loss of ellipticity analysis based on the homogenized moduli of periodic composites, or alternatively, it can also be detected by Bloch wave analysis when the identified critical wavenumber $\mathbf{K}_{cr} \rightarrow \mathbf{0}$ [26].

Postbuckling analysis is carried out to capture the response of the composite after the onset of instability, thus enlarged unit cell needs to be constructed based on the critical wavenumber $\mathbf{K}_{cr}$ obtained by Bloch-Floquet instability analysis. To the trigger the bifurcation mode, the initial composite geometry is disturbed by a small amplitude imperfection in the form of the buckling mode. Then, periodic displacement boundary conditions are imposed on the enlarged unit cell to apply the averaged macroscopic deformation.

Chapter 2

Microscopic instabilities and elastic wave propagation in finitely deformed laminates with compressible hyperelastic phases[*]

The elastic instability and wave propagation in compressible layered composites undergoing large deformations are investigated. We find that the compressible laminates require larger strains to trigger mechanical instabilities, thus resulting in lower amplitudes of instability induced wavy patterns in compressible laminates as compared to incompressible layered materials. Moreover, we show that instability-induced wavy patterns give rise to the tunability of the widths and locations of shear and pressure wave band gaps.

---

[*] Based on the published paper: Li J, Slesarenko V, Rudykh S. Microscopic instabilities and elastic wave propagation in finitely deformed laminates with compressible hyperelastic phases. Eur J Mech - A/Solids 2019;73:126–36.

2.1 Introduction

Design of microstructured metamaterials for manipulating elastic wave propagation has drawn considerable attention [72–85]. These new materials can potentially serve for enabling various applications, such as wave guide [86], vibration damper [87], cloaking [88], and subwavelength imaging [89,90]. Recently, soft metamaterials with reconfigurable microstructures in response to external stimuli, such as mechanical load [65,91–94], electric and/or magnetic field [95–101], attracted significant interest for tuning elastic wave propagation. Moreover, the elastic instability induced buckling phenomena, giving rise to a sudden change in microstructure, have been demonstrated to be greatly instrumental for the design of switchable phononic crystals. Thus, Bertoldi and Boyce [67,68] introduced the concept of instability assisted elastic wave band gaps (BGs) control in soft elastomeric materials with periodically distributed circular voids [6,62,69]. Rudykh and Boyce [102] showed that the elastic instability induced wrinkling of interfacial layers could be utilized to control the BGs in deformable layered composites (LCs). In this work, we analyze the phenomena with a specific focus on the influence of the constituent compressibility on the instabilities and elastic wave BGs of finitely deformed neo-Hookean laminates in the postbuckling regime.

The important work on the stability of layered and fiber composites by Rosen [22], considered stiff layers embedded in a soft matrix as elastic beams on an elastic foundation, and derived an explicit expression to predict the critical buckling strain. Parnes and Chiskis [24] revisited the instability analysis in linear elastic LCs, and they found that the buckling strain of dilute composites that experienced microscopic instability was constant, while for the macroscopic case, the buckling strain agreed with the results of Rosen [22]. Triantafyllidis and Maker [23] analyzed the onset of instability in finitely deformed periodic layered composites. They demonstrated the existence of the microscopic and macroscopic (or long wave) instabilities by employing the Bloch-Floquet analysis [26], along with the loss of ellipticity analysis that is typically used to detect the onset of macroscopic instability [29,30,103]. Nestorovic and Triantafyllidis [25] investigated the interplay between macroscopic and microscopic instability of hyperelastic layered media subjected to combinations of shear and compression deformation. Micromechanics based homogenization was utilized to predict the macroscopic instability of transversely isotropic fiber composites with hyperelastic phases [104,105]. Gao and Li [106] showed that the wavy patterns of the interfacial layer could be tuned by the interphase between the interfacial layer and soft matrix. Recently, Slesarenko and Rudykh [37] implemented the Bloch-Floquet technique into the finite element based code and examined the macroscopic and microscopic instability of periodic hyperelastic 3D fiber composites. More recently, Galich et al [107] focused on the influence of the periodic fiber distribution on instabilities and shear wave propagation in the hyperelastic 3D fiber composites. Furthermore, the microscopic and macroscopic instability phenomena of multi-layered composites under plane strain conditions were observed in experiments via 3D-printed layered materials [35]. Slesarenko and Rudykh [36] experimentally showed that the wavy patterns in LCs with visco-hyperelastic constitutes could be tuned by the applied strain rate. Li et al. [12] experimentally realized the instability development in periodic 3D fiber composites. Through these studies, the role of stiff fiber reinforcement on the stability of composites has been well understood; in particular, the composites with stronger reinforcement (with higher shear modulus contrasts or with larger fiber volume fractions) are more prone to instabilities. However, the role of phase compressibility on the instability development and post-buckling behavior of hyperelastic laminates has not been examined.

In the first part of this chapter, we will focus on the influence of phase compressibility on the onset of instability and critical wavelengths that define the postbuckling patterns of the microstructure. We note that it is possible to use the estimates for the onset of instability and critical wavelengths based on the linear elasticity theory [35,102]; this, however, does not fully account for the nonlinear effects of finite deformations. To take into account these effects, we perform the instability analysis superimposed on finite deformations. The obtained information about the critical wavelengths is further used in the analysis presented in the second part of this chapter, where the elastic waves in the postbuckling regime are analyzed.

Rytov [64] derived explicit dispersion relations for elastic waves propagating perpendicular to the layers showing the existence of the elastic wave BGs (or stop bands) in LC frequency spectrum. Wu et al. [108], and Fomenko et al. [109] investigated the elastic wave BGs of layered media with functionally graded materials. Recently, Srivastava [84] predicted the appearance of negative refraction at the interface between layered composite media and homogeneous material. More recently, Slesarenko et al. [66] showed that that negative group velocity can be induced by deformation in hyperelastic composites in the stable regime near elastic instabilities.

Galich et al. [65] obtained explicit expressions for shear and pressure long waves in finitely deformed LCs with isotropic hyperelastic phases. Moreover, based on the analysis by Rytov [64], Galich et al. [65] extended the classical results to the class of finitely deformed hyperelastic laminates. In particular, Galich et al. [65] show that the shear wave BGs are independent of the applied deformation in neo-Hookean laminates. In addition, the results of Galich et al. [65] demonstrate that the pressure wave BGs can be tuned by deformation, mostly via the change in the thickness of the layers. In this work, we examine the elastic wave propagation in finitely deformed neo-Hookean laminates in the *postbuckling* regime, and we specifically focus on the influence of material compressibility.

2.2 Simulations

We consider periodic layered composites consisted of two alternating hyperelastic phases with initial volume fractions $v_a = d_a/d$ and $v_b = 1 - v_a$ (see Figure 3(a)). Here and thereafter, the quantities corresponding to phase *a* and phase *b* are denoted by subscripts $(\bullet)_a$ and $(\bullet)_b$, respectively. The constitutive behavior of each phase is defined through the extended neo-Hookean strain energy density function

$$W(\mathbf{F}_\xi) = \frac{\mu_\xi}{2}\left(\mathbf{F}_\xi\colon\mathbf{F}_\xi - 3\right) - \mu_\xi \ln\left(J_\xi\right) + \left(\frac{K_\xi}{2} - \frac{\mu_\xi}{3}\right)(J_\xi - 1)^2, \qquad (18)$$

where μ_ξ is the initial shear modulus, K_ξ is the bulk modulus, subscript ξ stands for *a* or *b*. The compressibility of the material is defined by the ratio K_ξ/μ_ξ.

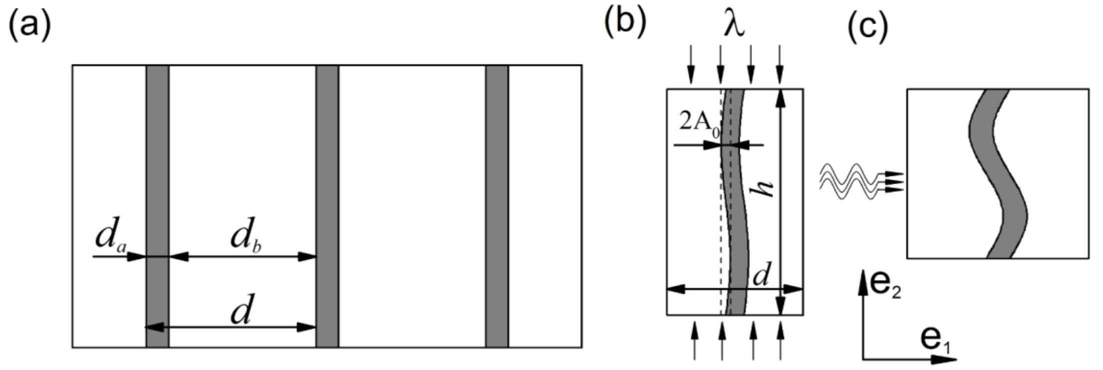

Figure 3. (a) Periodic LCs, (b) Deformed unit cell, (c) Small amplitude wave propagation in the deformed unit cell.

In order to detect the onset of instability of LCs, and obtain the corresponding critical stretch ratio λ^{cr} and critical wavelength l^{cr} (or critical wavenumber k^{cr}), the Bloch-Floquet analysis is used (for details, see Slesarenko and Rudykh [37]; Triantafyllidis and Maker [23]). The microscopic instability is associated with the existence of bifurcation at a non-zero critical wavenumber k^{cr}, which defines the buckling mode of the structure through the critical wavelength $l^{cr} = 2\pi/k^{cr}$. The specific case of so-called long wave mode, $k^{cr} \rightarrow 0$, can be detected by the loss of ellipticity analysis for the effective elastic modulus tensor. The obtained information about the critical wavelengths is used in the subsequent postbuckling analysis (and elastic wave propagation in the postbuckling regime). A unit cell with height $h = l^{cr}$ is constructed in the finite element model, and small amplitude imperfections are introduced in the form of $X_1 = \mathrm{A}_0 \cos(\frac{2\pi X_2}{h})$ imposed on the initial geometry of the stiffer layer (see Figure 3(b)). In particular, through checking different weights (A_0/d_a) of the imperfections, we find that $\mathrm{A}_0/d_a = 10^{-3}$ is proper to trigger bifurcation and enough precise to capture the development of the instability induced wavy patterns. The periodic boundary conditions of displacement are imposed on the unit cell, and the mechanical loading is applied in terms of average deformation gradient, which is used in the displacement imposed periodic boundary conditions on the unit cell (see Figure 3(b)). The obtained numerical solution for the finitely deformed state is used in the subsequent small amplitude wave propagation analysis. This has been done by employing the Bloch wave numerical analysis (implemented in the finite element code, for details, see Bertoldi and Boyce [68]; Galich et al. [110]; Slesarenko and Rudykh [37]; Li et al. [16]). Thus, the dispersion curves for elastic waves propagating in finitely deformed compressible LCs are obtained.

2.3 Results and discussion

2.3.1 Instabilities in finitely deformed compressible layered composite

We start from consideration of the influence of compressibility on the onset of instability and the corresponding critical wavelengths. Figure 4 shows the dependence of critical stretch ratio λ^{cr} (a, c) and critical wavenumber $\tilde{k}^{cr}$ (b, d) on the compressibility of LCs with neo-Hookean phases. Both phases are characterized by identical compressibility ($K_a/\mu_a = K_b/\mu_b = K/\mu$). The critical wavenumber is normalized as $\tilde{k}^{cr} = k^{cr}d/(2\pi)$. For completeness, we show also the linear elastic material estimates denoted by the short-dashed black (Rosen, [22]) and by dotted blue curves (Parnes and Chiskis, [24])[1]. The circular points denote the numerical results for LCs with neo-Hookean phases. Hollow and solid symbols correspond to microscopic and macroscopic instabilities, respectively. Note that we also add the curves connecting the symbols, and these curves do not represent the actual data, but indicate the trends in the dependencies only.

---

[1] The compressibility of linear elastic material is related to that of neo-Hookean material by Poisson's ratio $\nu = \frac{3K/\mu-2}{6K/\mu+2}$.

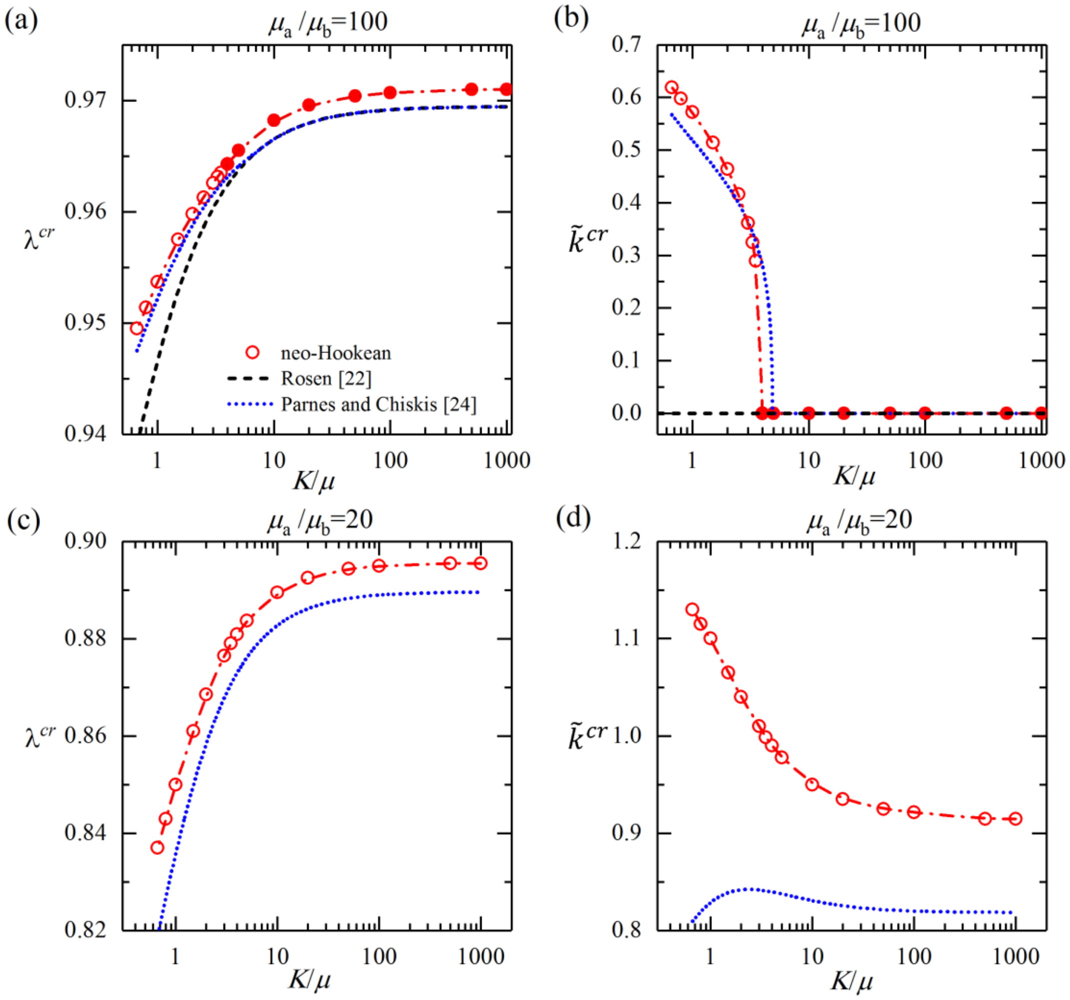

Figure 4. Dependence of critical stretch ratio λ^{cr} (a, c) and critical wavenumber $\tilde{k}^{cr}$ (b, d) on the compressibility of LCs with $v_a = 0.09,\ K_a/\mu_a = K_b/\mu_b$. Hollow symbols correspond to microscopic instabilities, while solid symbols correspond to macroscopic instabilities.

Compressible LCs are observed to be more stable; in particular, the critical stretch ratio increases with a decrease in compressibility (an increase in K/μ), see Figure 4(a, c). This stabilizing effect may be due to the additional freedom in accommodating deformation in compressible LCs as compared to the constrained incompressible LCs.

The linear estimates and nonlinear analysis predict similar trends of the dependence of critical stretch on compressibility. However, the nonlinear analysis predicts earlier onsets of instabilities. Moreover, for composites with lower stiffness ratio, significant differences in linear and nonlinear predictions of critical wavenumber are observed (see Figure 4(d)). The LCs with lower shear modulus contrasts require larger deformation for the onset of instability; therefore, the nonlinear behavior (not accounted in the linear estimates) becomes more prominent.

Remarkably, compressible LCs are found to develop instabilities on microscopic length-scales, while LCs with higher incompressibility (larger K/μ) buckle in the long wave mode. For example, in LC with $\mu_a/\mu_b = 100$, we observe a switch in buckling modes from microscopic instability to macroscopic instability indicated by the void (microscopic) and filled (macroscopic) red circles in Figure 4(a, b). Similar transitions from microscopic to macroscopic instability modes in incompressible fiber composites happen when the shear moduli contrast is increased beyond a certain threshold value [37]. For compressible LCs, the observed macro-to-micro mode switch (at certain threshold compressibility value) may be attributed to the compressibility-induced reduction in the effective stiffness ratio between the phases; thus, leading to the development of microscopic instabilities. Finally, we note that the critical stretch ratio of neo-Hookean LCs attains the analytical estimation for incompressible neo-Hookean LCs [23] as the incompressibility parameter is increased.

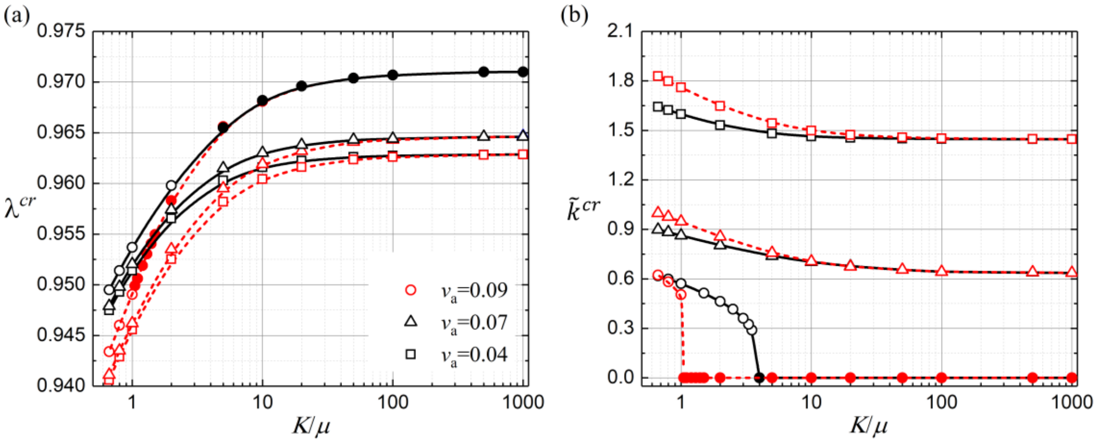

Figure 5. Dependence of critical stretch ratio λ^{cr} (a) and critical wavenumber $\tilde{k}^{cr}$ (b) on the compressibility of LCs with $\mu_a/\mu_b = 100$. The black points correspond to LCs with identical compressibility; the red points correspond to LCs with nearly incompressible ($K_b/\mu_b = 10^3$) soft matrix.

Next, we examine the influence of compressibility on instabilities in LCs with different volume fractions. Figure 5 shows the critical stretch ratio λ^{cr} (a) and normalized critical wavenumber $\tilde{k}^{cr}$ (b) as functions of compressibility for LCs with $\mu_a/\mu_b = 100$. The square, triangle, and circle symbols correspond to the LCs with $v_a = 0.04, 0.07,$ and 0.09, respectively. The black points correspond to the results of LCs with identical phase compressibility, while the red points correspond to LCs with nearly incompressible matrix ($K_b/\mu_b = 10^3$), and stiffer layers with varying compressibility. Note that we consider the range of $K/\mu \geq 2/3$, such that the initial Poisson's ratio is positive [111]. Figure 5(a) shows that the critical stretch ratio increases with a decrease in compressibility (an increase in K/μ). Note that LCs with $K/\mu \gtrsim 50$, critical stretch changes only slightly with an increase in K/μ. However, for LCs with $K/\mu \lesssim 10$, a decrease in compressibility (an increase in K/μ) results in a pronounced increase in critical stretch. For example, when compressibility of LC (with identical phase compressibility) is changed from $K/\mu = 50$ to 10^3, the critical stretch of LC with $v_a = 0.04$ increases from $\lambda^{cr} = 0.9627$ to only 0.9628; whereas, a decrease in compressibility from $K/\mu = 2/3$ to 10 leads to an increase in critical stretch from $\lambda^{cr} = 0.9475$ to 0.9616. Figure 5(b) shows the dependence of critical wavenumber $\tilde{k}^{cr}$ on the ratio of K/μ. We observe that the critical wavenumber decreases with a decrease in compressibility (i.e. increase in K/μ), the effect is more pronounced at the range of $K/\mu \lesssim 10$. We note that the LC with $v_a = 0.09$ exhibits a transition from finite wavelength mode to long wave instability mode at $K/\mu \approx 3.5$ for LCs with identical phase compressibility, $K/\mu \approx 1.1$ for LCs with nearly incompressible matrix and varying stiff layer compressibility, corresponding to a switch from microscopic instability to macroscopic instability.

For LCs with nearly incompressible matrix ($K_b/\mu_b = 10^3$), the influence of the stiffer layer compressibility on critical stretch ratio and wavenumber is more pronounced as compared to LC with identical phase compressibility (compare the red symbols with the black symbols in Figure 5(a, b)). For example, for LC with $v_a = 0.07$, the change in compressibility of the stiffer layer from $K_a/\mu_a = 10^3$ to 2/3, leads to the changes in critical stretch ratio from $\lambda^{cr} = 0.965$ to 0.941, and critical wavenumber from $\tilde{k}^{cr} = 0.64$ to 1.00. For LCs with identical phase compressibility, the same change in compressibility decreases the critical stretch ratio from $\lambda^{cr} = 0.965$ to 0.948, and increases the critical wavenumber from $\tilde{k}^{cr} = 0.64$ to 0.90. One of the factors for the observed differences can be attributed to the change in the volume fraction of the stiffer layer under compression. For LCs with identical compressibility ($K_a/\mu_a = K_b/\mu_b$), the volume fraction of the stiffer layer is constant under contraction deformation (before the onset of instability). However, for LCs with nearly incompressible soft matrix and compressible stiff layers, the stiffer layer volume decreases under contraction deformation and the volume of the matrix remains constant. Thus, the volume fraction of the stiffer layer (in the deformed state) decreases. As a result, LCs with more compressible stiffer layers (with lower K_a/μ_a) buckle at large strain levels, and develop wavy patterns of smaller wavelengths as compared to LCs with identical phase compressibility. However, the dependence of the wavelength on the stiffer layer compressibility changes for LCs with larger volume fractions, for which LCs may exhibit long wave instabilities (depending on the compressibility).

For LCs with identical phase compressibility, an increase in stiff layer volume fraction results in significant decrease in critical strain ($\varepsilon^{cr} = 1 - \lambda^{cr}$) and critical wavenumber. For example, for LC with nearly incompressible phases ($K_a/\mu_a = K_b/\mu_b = 10^3$), an increase in stiff layer volume fraction from $v_a = 0.04$ to 0.09 leads to an earlier onset of instabilities at $\varepsilon^{cr} = 0.029$ ($\varepsilon^{cr} = 0.037$ for $v_a = 0.04$), and leads to a switch in the instability mode from finite size $\tilde{k}^{cr} = 1.45$ (for $v_a = 0.04$) to long wave mode ($\tilde{k}^{cr} \to 0$ for $v_a = 0.09$).

Next we investigate the influence of compressibility on instabilities in LCs with different shear modulus contrasts. Figure 6 shows the dependence of critical stretch ratio (a, c, e) and critical wavenumber (b, d, f) on compressibility. The circular, square, and triangle symbols correspond to the results of LCs with shear modulus contrasts $\mu_a/\mu_b = 20, 100,$ and 500, respectively. The black and red points correspond to LCs with identical phase compressibility, and to LCs with nearly incompressible matrix and varying stiffer layer compressibility, respectively. In agreement with the previous results, here we observe that the critical stretch ratio increases with a decrease in compressibility (i.e. increase in K/μ), and the critical wavenumber decreases with a decrease in compressibility (i.e. increase in K/μ). We observe that the critical strain for LC with lower shear modulus contrast is more sensitive to a change in compressibility. The compressibility has a more significant effect on the critical wavenumber of LC with higher shear modulus contrast. For instance, for LC with $\mu_a/\mu_b = 20$, the change of compressibility from $K_a/\mu_a = K_b/\mu_b = 10^3$ to 2/3, leads to the changes in critical strain from $\varepsilon^{cr} = 0.105$ to 0.163, and critical wavenumber from $\tilde{k}^{cr} = 2.18$ to 2.57; thus the critical strain and wavenumber increase 55.24% and 17.89%, respectively. For LC with $\mu_a/\mu_b = 500$, the corresponding change in compressibility (from $K_a/\mu_a = K_b/\mu_b = 10^3$ to 2/3) leads to an increase in critical strain and wavenumber by 36.80% and 31.62%, respectively.

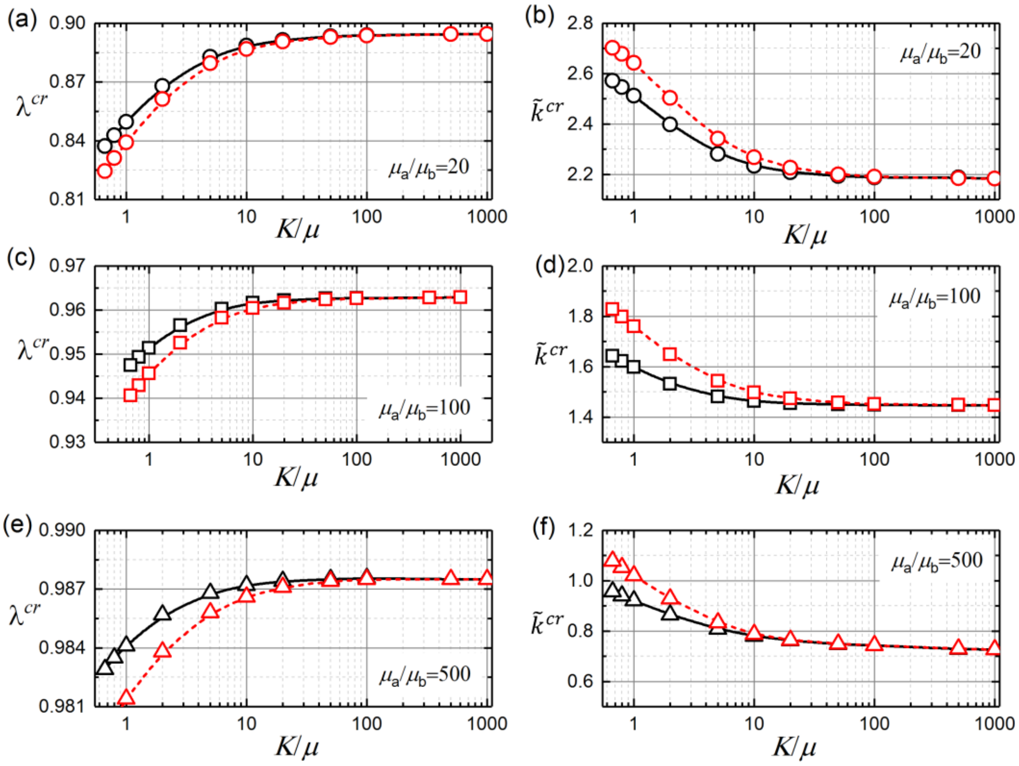

Figure 6. Dependence of critical stretch ratio λ^{cr} ((a), (c), and (e)) and critical wavenumber $\tilde{k}^{cr}$ ((b), (d), and (f)) on the compressibility of LCs with $v_a = 0.04$.

In addition, we also observe that an increase in the stiffer layer compressibility leads to a more significant increase in critical strain and wavenumber as compared to LC with identical phase compressibility in a wide range of shear modulus contrasts. This effect increases with an increase in shear modulus contrast (compare red and black symbols in Figure 6). For instance, for the case of $\mu_a/\mu_b = 500$, the critical strain and wavenumber for LC with identical phase compressibility $K/\mu = 2/3$ are $\varepsilon^{cr} = 0.017$ and $\tilde{k}^{cr} = 0.96$; and the critical strain and wavenumber for LC with $K_a/\mu_a = 2/3, K_b/\mu_b = 10^3$ are $\varepsilon^{cr} = 0.020$ and $\tilde{k}^{cr} = 1.08$, increased by 17.65% and 12.5%, respectively (compared to LC with $K/\mu = 2/3$). Whereas for the case of $\mu_a/\mu_b = 20$, the critical strain and wavenumber for LC with $K_b/\mu_b = 10^3$, $K_a/\mu_a = 2/3$ increase by approximately 8% and 5%, respectively, when compared to the corresponding LC with identical phase compressibility $K/\mu = 2/3$.

LCs with stiffer layers (higher shear modulus contrasts) are more prone to instabilities, and develop buckling modes at smaller wavenumbers (larger wavelength). For example, for LC with nearly incompressible phases, namely, $K_a/\mu_a = K_b/\mu_b = 10^3$, the composite with $\mu_a/\mu_b = 20$ and 100 buckles at $\varepsilon^{cr} = 0.106$ to 0.037, and develops wavy pattern at $\tilde{k}^{cr} = 2.18$ to 1.45, respectively.

To summarize, LCs with stronger role of stiffer layers are more prone to instabilities and develop buckling modes with larger wavelengths. Compressible LCs are found to be more stable thanks to the additional freedom in accommodating deformation as compared to the constrained incompressible LCs. There are compressibility-controlled switches in the LC buckling modes from macroscopic to microscopic instabilities. These switches may be a result of the reduction in effective stiffness ratio between the phases arising from the deformation of compressible LC. Moreover, LCs with nearly incompressible matrix are more stable than the LCs with identical phase compressibility. This stabilizing effect can be attributed to a decrease in the compressible stiffer layer volume fraction (while the volume of nearly incompressible matrix remains almost constant).

2.3.2 Elastic waves in finitely deformed compressible layered composite

Next, we consider elastic waves propagating in finitely deformed LCs in the direction perpendicular to the layers. For this case, Galich et al. [65] extended the results of Rytov [64] to account for the effect of finite deformation on elastic wave propagation. The explicit results for neo-Hookean LCs by Galich et al. [65] clearly show that band gaps (BG) – frequency ranges where waves cannot propagate – of shear waves do not depend on deformation. This is because the deformation induced changes in geometries and local material properties compensate each other. However, once the deformation exceeds the critical stretch ratio, the stiffer layers develop wavy patterns and deformation becomes inhomogeneous in the phases. Therefore, the analytical solution – that assumes that the layers remain flat and deformation is homogeneous in each layer – reaches the limits of applicability. To overcome this limit and analyze the influence of compressibility on elastic wave propagation in finitely deformed compressible LCs, we make use of the finite element Bloch wave analysis superimposed on large deformations [67,68].

We start with illustrating the dispersion curves of the undeformed and deformed ($\lambda = 0.9$) LCs. The dispersion curves shown in Figure 7 are for LC with $v_a = 0.04$, $\mu_a/\mu_b = 100, \rho_a/\rho_b = 1, K_a/\mu_a = K_b/\mu_b = 1$. The continuous curves correspond to shear waves, while the dashed curves are for pressure waves. The shaded grey and blue areas correspond to the shear wave band gaps (SBGs) and pressure wave band gaps (PBGs), respectively. Frequency is normalized as $f_n = \frac{\omega d}{2\pi}\sqrt{\overline{\rho_0}/\tilde{\mu}}$, where ω is the angular frequency, $\overline{\rho_0} = \rho_{0a}v_a + \rho_{0b}v_b$, $\tilde{\mu} = \left(\frac{v_a}{\mu_a} + \frac{v_b}{\mu_b}\right)^{-1}$. We note that the numerical results are in perfect agreement with the theoretical results [64,65] for the range of deformations, where the LCs remain stable. In the buckled deformed state at $\lambda = 0.9$ ($\lambda^{cr} = 0.9514$), the first SBG widens from $\Delta f_n = 0.020$ (in the undeformed state) to 0.024, and its upper boundary shifts from $f_n = 0.510$ to 0.524, the first PBG widens from $\Delta f_n = 0.031$ (in the undeformed state) to 0.032 and its upper boundary shifts from $f_n = 0.779$ to 0.767.

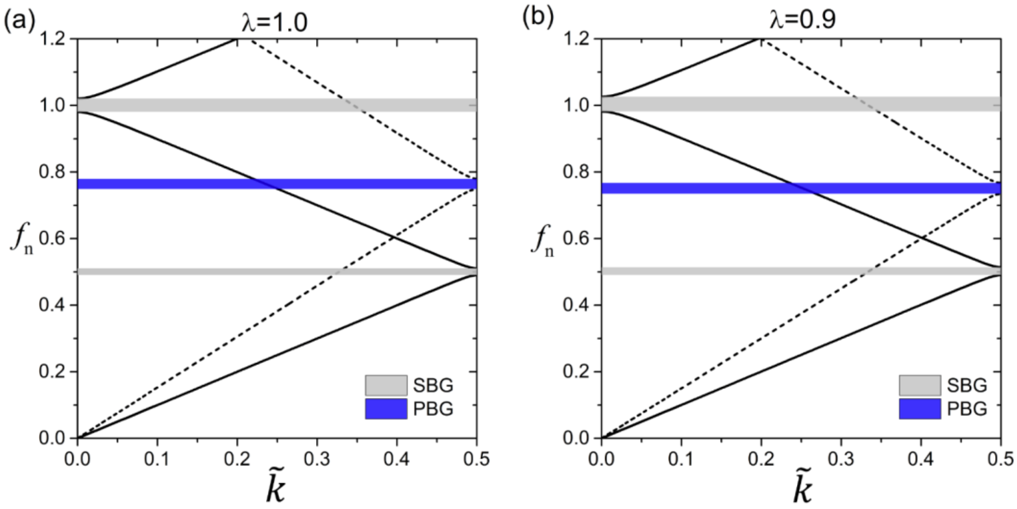

Figure 7. Dispersion relations for shear (black continuous curves) and pressure (black dashed curves) waves in LC with $v_a = 0.04$, $\mu_a/\mu_b = 100, \rho_a/\rho_b = 1, K_a/\mu_a = K_b/\mu_b = 1$ in undeformed (a) and deformed (b) states. The shaded areas correspond to the shear (grey) and pressure (blue) wave BGs.

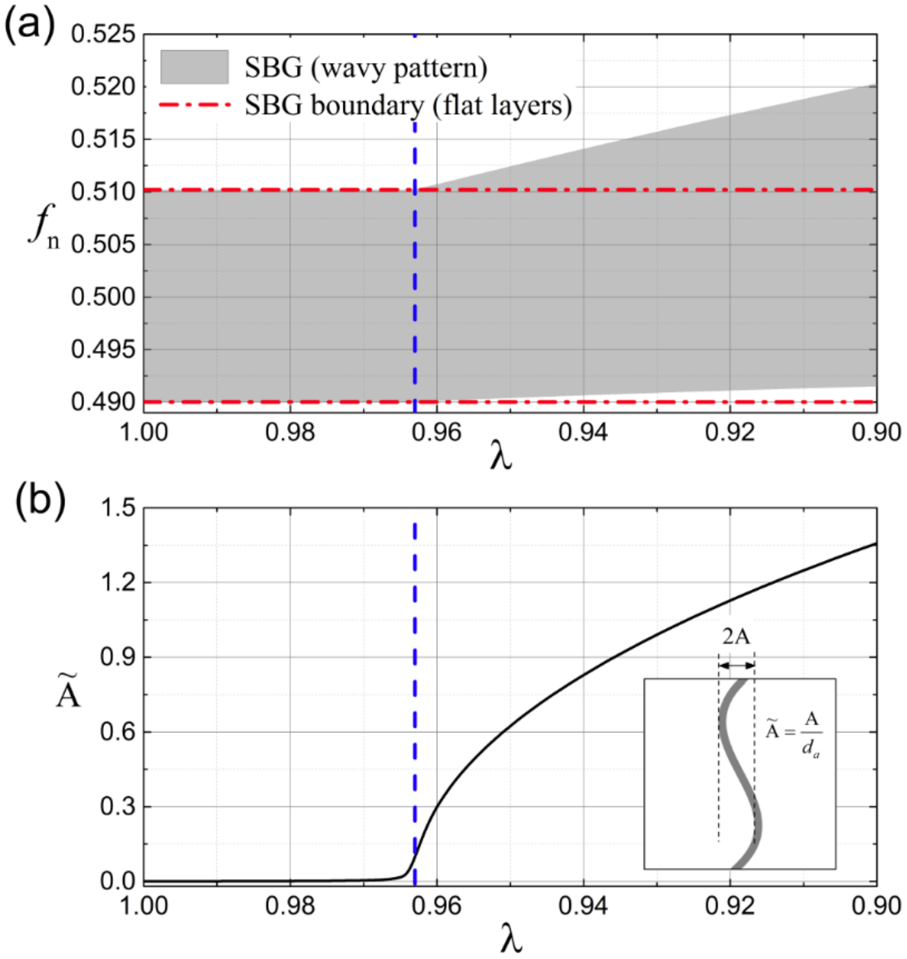

Figure 8. Dependence of SBG (a) and wrinkle amplitude (b) on applied deformation for LC with $v_a = 0.04$, $\mu_a/\mu_b = 100$, $\rho_a/\rho_b = 1$, $K_a/\mu_a = K_b/\mu_b = 10^3$.

Next, we investigate the influence of deformation on the BG structure of nearly incompressible LCs. Figure 8 shows evolutions of the first SBG (a) and wrinkle amplitude (b) as functions of deformation. The wrinkle amplitude is normalized as $\widetilde{A} = \frac{A}{d_a}$. The LC with $v_a = 0.04$, $\mu_a/\mu_b = 100, \rho_a/\rho_b = 1$ consists of nearly incompressible phases ($K_a/\mu_a = K_b/\mu_b = 10^3$), and it experiences microscopic instability at $\lambda^{cr} = 0.963$ with the critical wavenumber $\tilde{k}^{cr} = 1.45$. To highlight the effect of instability induced wavy patterns on SBG, we show the results for the buckled LC and the flat LC (n which the wavy patterns are suppressed) under the same deformation. The analytical results [65] for the first SBG of LC with flat layers are located at lower frequency boundary $f_n = 0.490$ and width $\Delta f_n = 0.020$, which is independent of deformation. Before the onset of instability ($\lambda^{cr} = 0.963$), the wavy pattern amplitude is negligible (see Figure 8(b)), and LCs produce identical SBGs (see Figure 8(a)). After the onset of instability, the LC develops wavy patterns, and the amplitude of wrinkles rapidly increases with an increase in deformation (see Figure 8(b)). The appearance of the wavy patterns shifts up the location of SBG and expands its width. The effect is more significant for the upper frequency boundary of the BG. For example, the deformation of $\lambda = 0.9$ widens the SBG from $\Delta f_n = 0.020$ to 0.029 and shifts its upper frequency boundary from $f_n = 0.510$ to 0.520. We note that for the considered nearly incompressible LC ($K/\mu = 10^3$), PBGs are located at relatively high frequency ranges (compared to the first SBG). For example, according to the calculation that based on the results of Galich et al. [65], the lower boundary of the first SBG for considered LC in the undeformed state is $f_n = 0.490$ (with $\Delta f_n = 0.020$), while the lower boundary of the corresponding first PBG is $f_n = 15.51$ (with $\Delta f_n = 0.63$). The numerical investigation of PBGs in LCs with nearly incompressible phases requires a large number of calculated eigenfrequencies and is not considered here.

To illustrate the influence of deformation in compressible LCs, we show SBG (a), PBG (b), and wrinkle amplitude (c) as functions of deformation in Figure 9. The results are given for the LC with $v_a = 0.04,\ \mu_a/\mu_b = 100, \rho_a/\rho_b = 1, K_a/\mu_a = K_b/\mu_b = 1$. The considered LC experiences microscopic instability at $\lambda^{cr} = 0.951$ with the critical wavenumber $\tilde{k}^{cr} = 1.60$. For the SBG (shown in Figure 9(a)), we observe that the appearance of the wavy patterns leads to widening of the SBG. Moreover, the SBG is shifted towards higher frequency range after the applied deformation attains the critical stretch level; a further increase in strain level (decrease in stretch ratio) leads to an increase in the width of the SBG. In particular, the applied deformation of $\lambda = 0.9$ widens the SBG from $\Delta f_n = 0.020$ to 0.023 and shifts its upper frequency boundary from $f_n = 0.510$ to 0.514. Thus, for highly compressible LCs, the influence of instability induced wavy patterns on the widths of SBGs is weaker than the one in nearly incompressible LCs (shown in Figure 8(a)). This happens because an increase in compressibility (decrease in K/μ) leads to a decrease in wavy pattern amplitude. For example, the amplitudes in LCs with nearly incompressible ($K_a/\mu_a = K_b/\mu_b = 10^3$) and highly compressible phases ($K_a/\mu_a = K_b/\mu_b = 1$) at the deformation of $\lambda = 0.9$ are $\widetilde{\mathrm{A}} = 1.36$ and 1.10, respectively.

For PBG (shown in Figure 9(b)), the LCs with wavy patterns and flat layers produce almost identical PBGs for the range of deformation prior to the onset of instability ($\lambda^{cr} = 0.951$). After the onset of instability, however, the instability induced wavy patterns widen the PBG and shift it towards higher frequency range. This effect is more significant on the upper frequency boundary of PBG. For example, compared to the LC with flat layers, the PBG of LC with wavy patterns widens from $\Delta f_n = 0.030$ to 0.032 and its upper frequency boundary shifts from $f_n = 0.764$ to 0.767 at the deformation of $\lambda = 0.9$. This is similar to the previous results for SBGs (see Figure 8(a), Figure 9(a)).

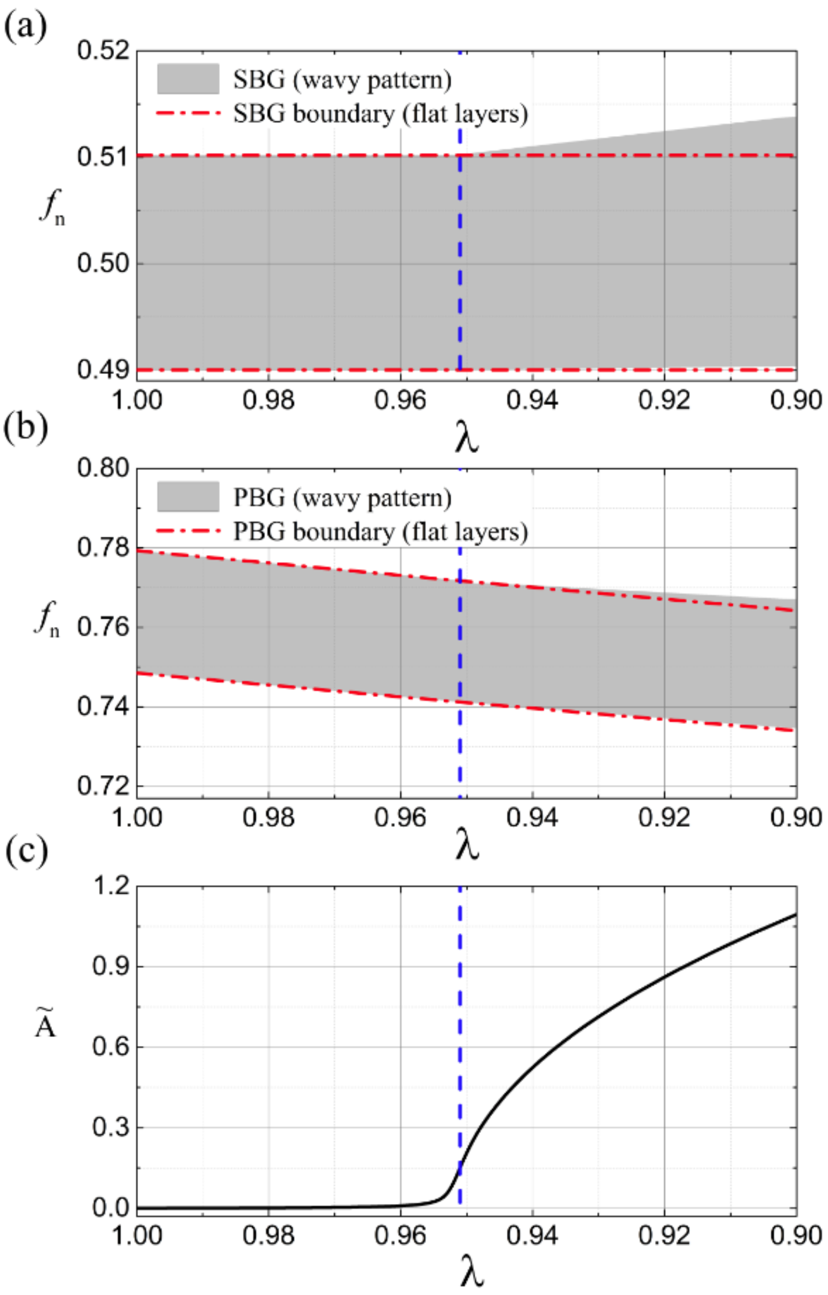

Figure 9. Dependence of SBG (a), PBG (b), and wrinkle amplitude (c) on applied deformation for LC with $v_a = 0.04$, $\mu_a/\mu_b = 100, \rho_a/\rho_b = 1, K_a/\mu_a = K_b/\mu_b = 1$.

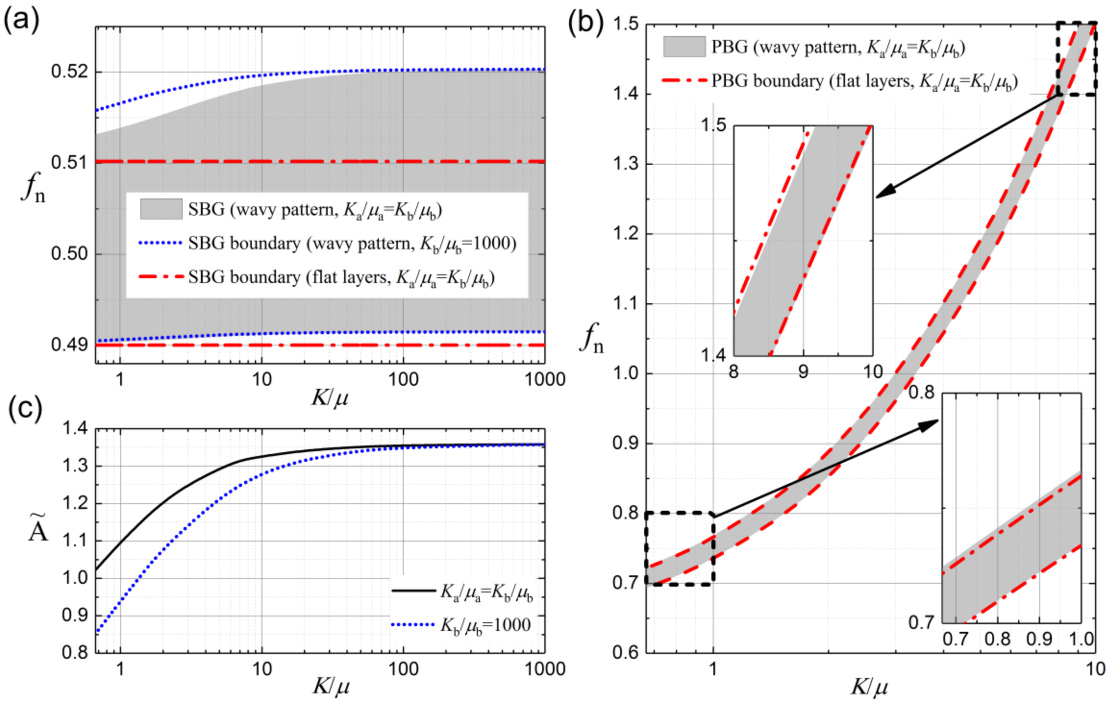

Figure 10. Dependence of SBG (a), PBG (b), and wrinkle amplitude (c) on the compressibility of LCs with $v_a = 0.04$, $\mu_a/\mu_b = 100, \rho_a/\rho_b = 1$ under deformation of $\lambda = 0.9$.

Figure 10 shows the dependence of SBG (a), PBG (b), and wrinkle amplitude (c) on the compressibility parameter K/μ. The results are given for LCs with $v_a = 0.04, \mu_a/\mu_b = 100, \rho_a/\rho_b = 1$ subjected to a contraction deformation of $\lambda = 0.9$. For LCs with flat layers, we observe that compressibility does not affect the SBGs (see Figure 10(a)) – in full agreement with the analytical results[2] of Galich et al. [65]. For LCs with wavy patterns, however, we observe that the SBGs are widened and the SBG locations are shifted towards higher frequency ranges. This effect increases with a decrease in compressibility (i.e. increase in K/μ). For example, when the compressibility changes from $K/\mu = 0.67$ to 10^3, the width of SBG of LC with identical compressibility increases from $\Delta f_n = 0.023$ to 0.029. This is due to the fact that an increase in K/μ leads to an increase in wrinkle amplitude (see Figure 10(c)). Moreover, we note that LCs with identical phase compressibility show larger wrinkle amplitudes as compared to LCs with nearly incompressible matrix (see Figure 10(c)). However, LCs with nearly incompressible matrix show more significant widening of SBGs (Figure 10(a)). This indicates that the tunability of the SBG is governed by a complicated interplay of the local material property and geometry changes; these effects are discussed below along with the illustrations in Figure 10.

---

[2] The change in geometry induced by deformation is fully compensated by the corresponding change in material properties in neo-Hookean laminates with compressible and incompressible phases.

For PBGs in highly compressible LCs, we observe that the instability induced wavy patterns expand the widths and shift their locations to higher frequency ranges (as compared to the LCs with flat layers). For example, for LC with $K/\mu = 0.67$, the appearance of wavy patterns expands the width of PBG from $\Delta f_n = 0.028$ to 0.031 and shifts its upper frequency boundary from $f_n = 0.721$ to 0.724. Whereas with the decrease of compressibility (i.e. increase in K/μ), the effect of wavy patterns on PBG gradually changes from expanding the BG width and shifting its location to higher frequency range, to narrowing the BG width and shifting its location to lower frequency range (see Figure 10(b)). For example, for LC with $K/\mu = 10$, the wavy patterns narrow the width of PBG from $\Delta f_n = 0.062$ to 0.058, and shift its upper frequency boundary from $f_n = 1.565$ to 1.559. For the considered cases, the transition point at which the effect of wavy patterns on PBGs changes from expanding to narrowing the BG widths is at $K/\mu \approx 4$. We note that for the considered LCs with nearly incompressible soft matrix ($K_b/\mu_b = 10^3$), PBGs are located at relatively high frequency ranges (compared to the first SBG). Thus, numerical investigation of PBGs in LCs with nearly incompressible soft matrix requires a large number of calculated eigenfrequencies and is not considered here.

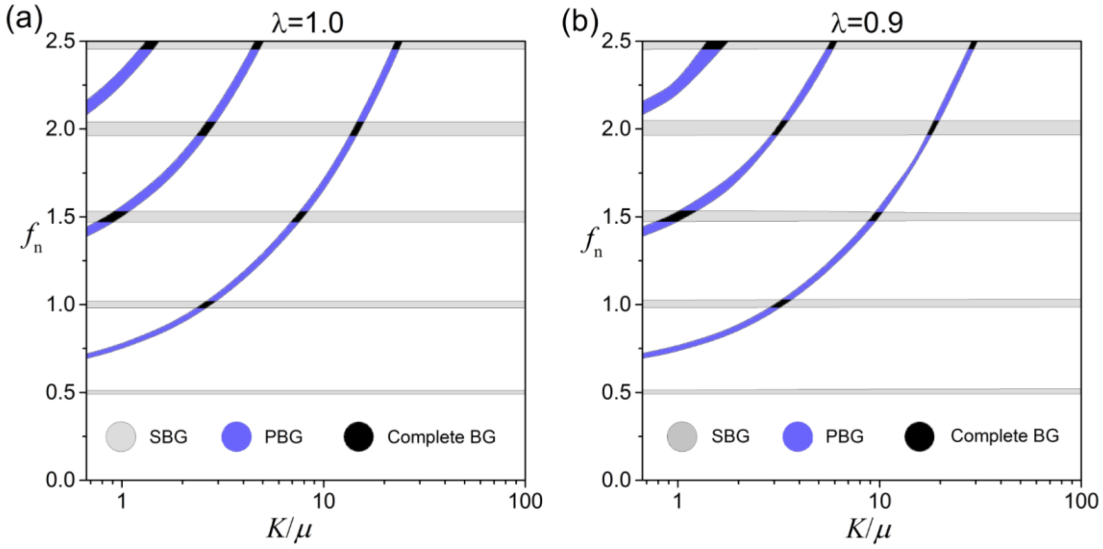

Figure 11. Dependence of BG on the compressibility of LCs with $v_a = 0.04$, $\mu_a/\mu_b = 100$, $\rho_a/\rho_b = 1$ in the undeformed (a) and deformed (b) states.

Next, we examine the so-called complete BGs where neither shear nor pressure waves can propagate. Figure 11 shows the dependence of SBG and PBG on the compressibility for LCs with $v_a = 0.04$, $\mu_a/\mu_b = 100$, $\rho_a/\rho_b = 1$ in the undeformed and deformed buckled ($\lambda = 0.9$ shown in Figure 11(b)) states. The shaded gray, blue, and black areas correspond to the shear wave, pressure wave, and complete BGs, respectively. In the undeformed state, the compressibility has no influence on SBGs. In the buckled deformed state, however, the locations of SBGs shift slightly, but the locations of PBGs are significantly shifted towards lower frequency ranges; this is similar to the observations in Figure 9 and Figure 10. Consequently, deformation can induce complete BG in a specific frequency range while the undeformed LCs do not produce complete BG in that frequency range. For example, for LC with $K/\mu = 3.5$, we observe the complete BG in the frequency range from $f_n = 1.002$ to 1.028,

]

but there is no complete BG in this frequency range for the same LC in the undeformed state.

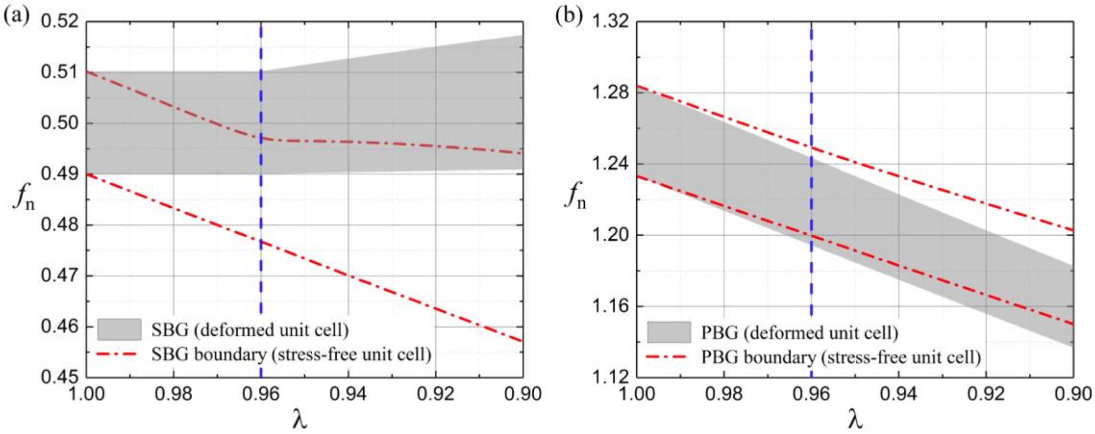

Figure 12. Dependence of SBGs (a) and PBGs (b) on deformation in LCs with $v_f = 0.04, \mu_a/\mu_b = 100, \rho_a/\rho_b = 1, K_a/\mu_a = K_b/\mu_b = 5$.

Finally, we examine the influence of deformation induced geometrical changes on band gaps. To this end, we analyze the evolution of BGs in stress-free configurations with the corresponding geometrical changes; and we compare these to the results for the deformed configurations (accounting for both geometrical and local material property changes). Figure 12 shows the SBGs (a) and PBGs (b) of the deformed LC and stress-free LC (with the corresponding geometrical change only) as functions of stretch ratio. The results are given for LC with $v_f = 0.04$, $\mu_a/\mu_b = 100$, $\rho_a/\rho_b = 1$, $K_a/\mu_a = K_b/\mu_b = 5$. The LC experiences the microscopic instability at $\lambda^{cr} = 0.960$ with the critical wavenumber $\tilde{k}^{cr} = 1.48$. Prior to the onset of instability ($\lambda^{cr} = 0.960$), the geometrical changes shift the SBG towards lower frequencies (see Figure 12(a)). This effect, however, is fully compensated by the corresponding deformation induced changes in local material properties (Galich et al, 2017a). Thus, the SBG of the deformed LC is independent of the applied deformation in the stable regime. However, upon the onset of instability, the SBG widens as the applied deformation is further increased. At this post-buckling regime, the corresponding SBG of the stress-free LC also widens with deformation. However, the width of the actual SBG (in the deformed LC) is smaller than that of the stress-free LC. Moreover, the actual SBG is shifted towards higher frequencies, whereas the geometrical changes push the SBG down towards lower frequencies. Thus, the instability induced changes in local material properties start prevailing over the geometrical changes in their influence on the SBG.

Next, we consider PBGs in the deformed and stress-free LCs. The PBGs are shifted towards lower frequencies. The location of the PBG of the deformed LC is lower than that of the stress-free LC (see Figure 12(b)). Therefore, we can conclude that both geometrical and local material changes shift down the location of PBG. Compared to the PBG in the undeformed state (the corresponding PBG width is $\Delta f_n = 0.051$), the PBGs of the stress-free and deformed LCs are $\Delta f_n = 0.053$ and 0.045 (at $\lambda = 0.9$), respectively. Thus, the deformation induced changes in local material property narrow the width of PBG. We note that the geometrical changes play a more significant role in affecting the location of PBG. For example, applied deformation of $\lambda = 0.9$ shifts the lower frequency boundary of the PBG of stress-free unit cell from $f_n = 1.233$ (undeformed state) to 1.150, whereas the same deformation shifts the lower frequency boundary of the PBG of the deformed unit cell from $f_n = 1.233$ (undeformed state) only to 1.137.

In summary, the instability induced wavy patterns results in tunability of the widths and locations of SBGs (that are not tunable by deformation in LCs with neo-

Hookean phases in the stable regime); this tunability, however, is not significant in comparison to the tunability of the PBGs (mainly through deformation induced changes in layer thickness), leading to the tunability of complete BGs (where neither shear nor pressure wave can propagate) by deformation.

2.4 Summary

We have examined the elastic instability and wave propagation in finitely deformed LCs with compressible neo-Hookean phases. The LCs with stronger role of stiffer layers (higher stiffness ratio and/or stiffer layer volume fraction) buckle earlier and develop buckling modes at smaller wavenumbers (larger wavelengths). Compressible LCs, however, are more stable and develop wavy patterns at smaller wavelengths. This stabilizing effect of compressibility may be attributed to the additional freedom to accommodate deformation as compared to the constrained incompressible LCs. We also observed the compressibility-controlled switches in the LC buckling modes from macroscopic to microscopic instabilities. These switches may be because applied deformation on compressible LC leads to a reduction in effective stiffness ratio between the phases. Moreover, LCs with identical phase compressibility are more prone to the onset of instabilities as compared to the composites with nearly incompressible matrix, this happens because the contraction deformation results in a decrease in the stiffer layer volume fraction for LCs with nearly incompressible matrix.

Next, we have examined the elastic wave propagation in finitely deformed LCs in the direction perpendicular to the layers. We have found that the instability induced wavy patterns lead to the widening of the SBG (mostly driven by the deformation induced geometrical changes), and shifts it towards higher frequency range (mostly driven by the deformation induced changes in local material property). Deformation significantly shifts the location of PBG to lower frequencies – mainly through the corresponding deformation induced changes in layer thickness – in addition to some tunability in the width of the PBG.

Chapter 3

Instabilities and pattern formations in 3D fiber composites[*]

We investigate elastic instabilities and pattern formations in 3D-printed deformable fiber composites. We experimentally realize the instability induced patterns in the deformable 3D systems of periodically distributed fibers embedded in a soft matrix. We observe that the fiber composites exhibit significant softening upon achieving the critical strain at which the stiff fibers cooperatively buckle into wavy patterns. For periodic fiber composites, we show that the critical wavenumber and critical strain decrease with an increase in fiber volume fraction, and an increase in the periodicity aspect ratio leads to a decrease in critical wavenumber and critical strain. For single fiber in a soft matrix system, we observe that the critical wavelength has a linear dependence on fiber diameter. An explicit formula is derived to estimate the dependence of critical wavelength on shear modulus contrast, and further verified by experimental data and numerical simulations.

---

[*] Based on the published paper: Li J, Slesarenko V, Galich PI, Rudykh S. Instabilities and pattern formations in 3D-printed deformable fiber composites. Compos Part B Eng 2018;148:114–22.

3.1 Introduction

Elastic stiff fibers embedded in a soft matrix are ubiquitous in natural and synthetic systems, e.g., microtubules in living cell [112,113], fibrous biological tissues [114,115], and fiber-reinforced polymer composites [116–119]. It is well known that an isolated fiber experiences classical Euler buckling, when subjected to axial compressive loads. However, for stiff fibers embedded in a soft matrix, the presence of soft matrix significantly decreases the critical wavelength and increases the critical strain [113,120,121]. This mechanical phenomenon has drawn considerable attention, due to its importance in fiber composite designs [37,122–124], functional material designs [106,125], and biological systems [114,126].

The buckling behavior of a single stiff circular wire embedded in an elastic matrix was firstly theoretically investigated by Herrmann et al. [127], which considered the elastic matrix as a three-dimensional continuous body and proposed two foundation model to investigate the buckling behavior of the stiff wire: (a) exact foundation model that considered the displacement and force continuity requirements between the elastic matrix and the stiff wire, (b) approximate foundation model that only considered the displacement and force in radial direction and neglected the shear deformation between the elastic matrix and the stiff wire. For the approximate mode, Herrmann et al. [127] derived an explicit expression to estimate the stiffness of the matrix. Later, Brangwynne et al. [113] employed Herrmann's approximate foundation model to elucidate their experimental observations on the buckling of microtubules in living cells, and derived an expression to approximate the value of matrix stiffness. Recently, Su et al. [128] studied the buckling behavior of a slender Nitinol rod embedded in a soft elastomeric matrix. Planar wavy patterns and non-planar coiled buckling modes were experimentally observed; these experimental observations were interpreted based on consideration of the two lowest buckling modes. Zhao et al. [121] examined the buckling of finite length elastic fiber in a soft matrix; the authors derived a formula to connect the overall strain and the strain state in stiff fiber. This formula showed that the buckling of stiff fiber could be significantly tuned by the slenderness ratio of the fiber. More recently, Chen et al. [129] examined the buckling of stiff wire in a soft matrix, and numerically showed that the stiff wire buckled in 2D sinusoidal configuration first, then gradually transited the configuration from 2D sinusoidal into 3D helical mode. In many studies, Winkler foundation model [130] is used to provide analytical linear elasticity based estimates for buckling of a single fiber in matrix. However, the accuracy of this model in a wide range of shear modulus contrast is not examined. Here, we first experimentally observe the buckling process of a stiff fiber embedded in a soft matrix under an axial compressive load by 3D printer fabricated specimens, and show the dependence of the critical wavelength on the stiff fiber diameter. Then, based on the Wrinker foundation model, we mathematically derive a new estimation for the effective stiffness, and give an explicit formula to calculate the critical wavelength of the stiff fiber in this system. The accuracy of this formula is verified by experimental data and numerical simulations.

The pioneering work on the stability analysis of layered and fiber composites was laid by Rosen [22], who derived an explicit expression to predict the buckling strain of layered composite with linear elastic material. Triantafyllidis and Maker [23] investigated microscopic and macroscopic instabilities in periodic layered composites with hyperelastic phases. Geymonant et al [26] established a rigorous theoretical foundation for microscopic instability analysis in periodic composites, connecting the specific case of long wave limit and the macroscopic loss of ellipticity analysis. The loss of ellipticity analysis has been used to study macroscopic instability in fiber-reinforced hyperelastic solids based on phenomenological models [29–31,103]. An alternative approach of micromechanics based homogenization was utilized to estimate the macroscopic instabilities in transversely isotropic hyperelastic fiber composite [104,105]. Recently, Greco et al. [131] investigated the influence of matrix or fiber/matrix interface microcracks on the failure behaviors of periodic fiber-reinforced composites under biaxial loading conditions. By making use of the Bloch-Floquet analysis superimposed on large deformations, Slesarenko and Rudykh [37] analyzed the interplay between macroscopic and microscopic instabilities in periodic hyperelastic 3D fiber composites subjected to an axial compressive load. Moreover, the buckling modes with wavy patterns in periodic layered composites under compressive loads were observed in experiments[35,36]. However, to the best of our knowledge, instabilities of deformable periodic 3D fiber composite have not been experimentally investigated. In this chapter, we study the buckling behavior of periodic 3D fiber composites with square and rectangular arrangements of periodic fibers; to this end we utilize a multimaterial 3D printer, and fabricate and mechanically test the periodic composite specimens. The experimentally obtained critical wavelengths and critical strains are compared with numerical results by Bloch-Floquet analysis.

3.2 Experiments and simulations

To experimentally observe the buckling process of fiber composite subjected to uniaxial compression along the fibers, we fabricated the specimens composed of stiff fibers embedded in an elastomeric soft matrix by using the multi-material 3D printer Object Connex 260-3. The soft matrix was printed in TangoPlus (TP) with the initial shear modulus $G \approx 0.23$ MPa, the stiffer fiber was printed in a digital material (DM) with the initial shear modulus $G \approx 240$ MPa; the digital material is a mixture of the two base material (TangoPlus and VeroWhite). Here, we considered two cases: single stiff fiber embedded in a soft matrix (Case A); periodic fiber composites with square and rectangle arrangements (Case B). All the specimens were printed in the shape of rectangular blocks to provide a clearer visualization of the buckled fiber shapes and pattern formations through the nearly transparent soft matrix material. Guided by the theoretical and numerical predictions of the buckling wavelength of the stiff fiber and considering the resolution of the multi-material 3D printer, the samples composed of a centrally located single DM fiber embedded in TP matrix (case A) were printed in dimensions 20 × 20 × 40 mm (length × width × height) and in stiff fiber diameters ranging from d=0.5 to 1.0 mm; the samples composed of 36 periodically distributed fibers embedded TP matrix (case B) were printed in dimensions 30 × 30 × 40 mm (length × width × height) and in stiff fiber volume fractions ranging from c_f=0.01 to 0.025, except for the sample with c_f=0.025, whose height was printed in 50 mm. For the composites with periodically distributed fibers, to reduce the influence of boundary effects on the buckling behavior of stiff fibers, the samples were printed with a boundary TP material layer of the thickness t=5 mm.

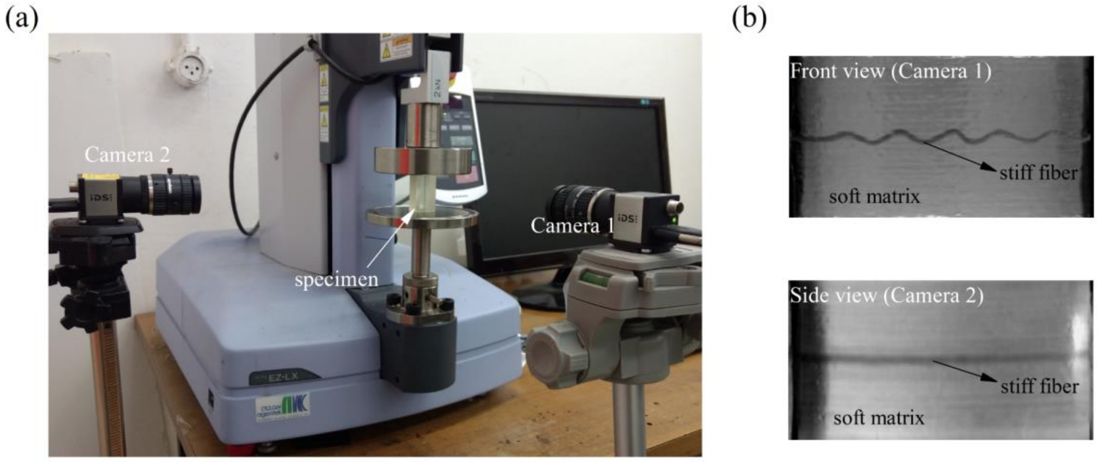
(a)
Camera 2
Camera 1
specimen
(b)
Front view (Camera 1)
stiff fiber
soft matrix
Side view (Camera 2)
stiff fiber
soft matrix

Figure 13. Experimental setup (a) and typical buckled configurations (b).

The uniaxial compression tests were carried out using Shimadzu EZ-LX testing machine (maximum load 2 kN). Figure 13 shows the experimental setup of the uniaxial compression of 3D-printed samples (a), and an illustration of the buckled configurations of the sample (b). To reduce the influence of material viscoelasticity on the observed behavior of the composite, the tests were performed at a low strain rate of 4×10^{-4} s^{-1}. Upon achieving the critical compression level, the stiffer fibers start developing the buckling shape; the process was captured by two digital cameras (located in front and on the side of the tested samples, as shown in Figure 13(a)). An example of the single fiber buckling induced configuration obtained from these orthogonal views is shown in Figure 13(b).

3.3 Results and discussion

3.3.1 Buckling of a single stiff fiber embedded in a soft matrix

We start with the investigation of the buckling of a single stiff fiber embedded in a soft matrix subjected to axial compressive load. The sketch of this system is shown in Figure 14. E and v refer to the Young's elastic modulus and Poisson's ratio, respectively. Subscripts $(\bullet)_f$ and $(\bullet)_m$ refer to the properties of the stiff fiber and soft matrix, respectively; d refers to the diameter of the stiff fiber. Figure 15 illustrates the development process of instability induced wavy patterns (a) and stress-strain curves (b) for DM fibers with diameters d =0.50, 0.71, and 1.00 mm. Since the DM fiber buckles almost in the planar configuration, only the view to record the main buckling shape is shown. We observe that the stiff fiber develops wavy patterns, and the critical wavelength and the amplitude of the wavy pattern increase with an increase in stiff fiber diameter (see Figure 15(a)). Figure 15(b) shows the corresponding stress–strain curves. Due to the stiff fiber buckling, we observe that the stress–strain curves exhibit softening near to the buckling point. This effect is more significant for the composite with larger stiff fiber diameter (see the dotted black curve in Figure 15(b)). Similar stress softening phenomenon has been observed in the bulging buckling mode of cylindrical shells under inflation [132,133]. In addition, we note that the composite strength increases with an increase in stiff fiber diameter in pre-buckling and postbuckling regimes.

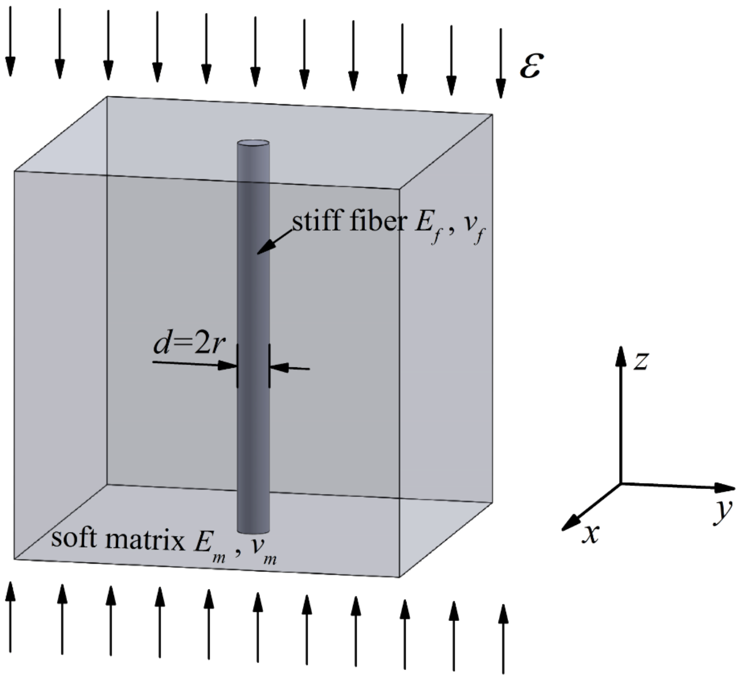

Figure 14. Sketch of an elastic stiff fiber embedded in a soft matrix subjected to axial compressive load.

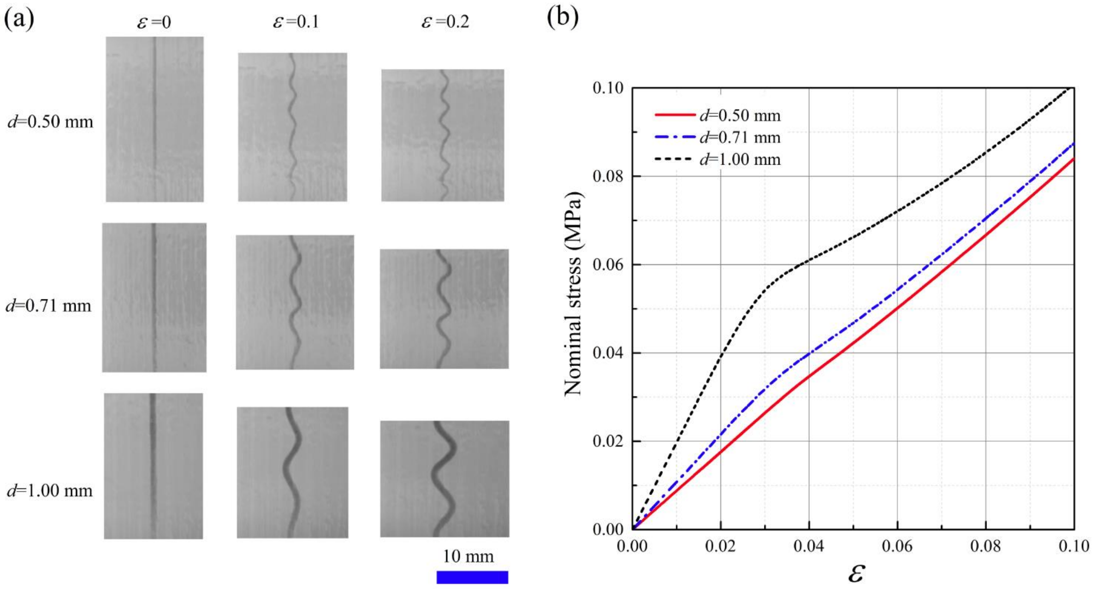

Figure 15. Development of instability induced wavy patterns (a) and stress-strain curves (b) for a single stiff fiber embedded in a soft matrix.

Next, to clarify the quantitative relation between the critical wavelength and stiff fiber diameter, we plot the critical wavelengths for all tested specimens as a function of stiff fiber diameter in Figure 16. Interestingly, the critical wavelength has a good linear dependence on the stiff fiber diameter, which will be explained by theoretical analysis in the following discussions.

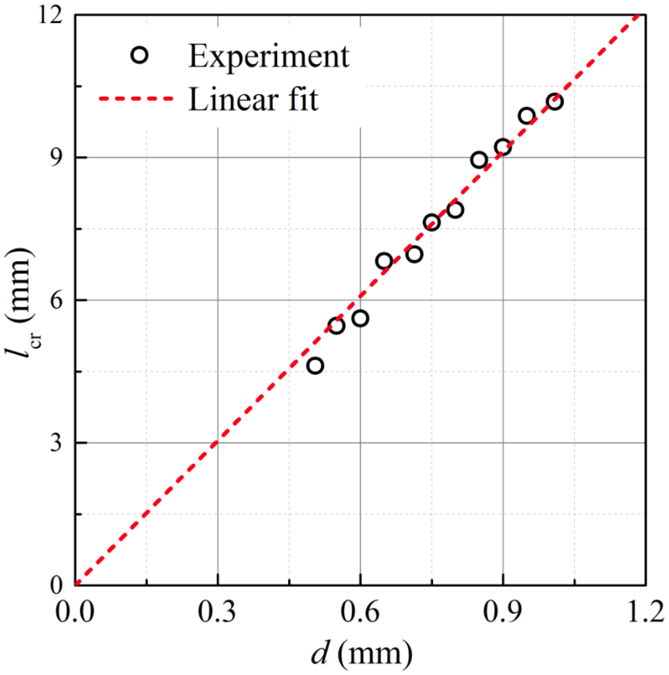

Figure 16. Dependence of critical wavelength l_{cr} on stiff fiber diameter.

Here, a theoretical analysis is performed to investigate the buckling mechanisms observed in the experiments. We note that the Winkler foundation model has been frequently utilized to investigate buckling of a single stiff fiber embedded in soft matrix [113,120,121,128]. However, previous works were mostly focused on the systems with high shear modulus contrast (the ratio of stiff fiber to soft matrix shear modulus is larger than 10^5). Here, we study buckling of the 3D printed system with shear modulus contrast of approximately 10^3. We employ the Winkler foundation model, and derive an explicit expression for an accurate approximation for the model, and we further examine the accuracy of model to predict the buckling of single stiff fiber embedded in soft matrix in a wide shear modulus contrast.

Considering the system as a thin and stiff beam supported by a soft matrix, the governing equation for a stiff fiber is given by [134]

$$E_f I_f \frac{\partial^4 u}{\partial z^4} + E_f S_f \varepsilon \frac{\partial^2 u}{\partial z^2} + Ku = 0, \tag{19}$$

where I_f and S_f are the area moment of inertia and cross-sectional area of the stiff fiber, respectively; ε is the applied axial strain. $u(z) = A\cos(kz)$ is the buckling mode with A and $k = 2\pi/l$ being the amplitude and wavenumber, respectively; l is the wavelength and K is the effective stiffness of soft matrix, which can be expressed as [127]

$$K = \frac{16\pi G_m(1-\nu_m)}{2(3-4\nu_m)K_0(kr)+K_1(kr)kr}, \tag{20}$$

where K_0 and K_1 are the modified Bessel functions of the second kind.

Substituting $u(z)$ and Eq. (20) into Eq. (19) yields

$$\varepsilon = \frac{(\tilde{k})^2}{4} + \frac{1}{E_f(\tilde{k})^2}\frac{16G_m(1-\nu_m)}{2(3-4\nu_m)K_0(\tilde{k})+K_1(\tilde{k})\tilde{k}}, \tag{21}$$

where $\tilde{k} = kr$ is the normalized wavenumber. The critical strain ε_{cr} corresponding to the onset of buckling can be obtained by minimizing Eq. (21) with respect to $\tilde{k}$; thus, the critical normalized wavenumber $\tilde{k}_{cr}$ depends on the material property of the system only. It also indicates that the critical wavelength has a linear dependence on stiff fiber diameter. This observation agrees well with our experimental results (see Figure 16).

Assuming the soft matrix to be incompressible (ν_m=0.5), Eq. (20) can be approximated (see Appendix A for details) as

$$K = \frac{4\pi G_m}{-\ln\left(\frac{e^{\gamma-\frac{1}{2}}}{2}\tilde{k}\right)}, \tag{22}$$

where γ=0.577 is the Euler's constant. We note that the form of Eq. (22) is consistent with the simplified stiffness for incompressible materials obtained by Zhao et al.[121], Brangwynne et al.[113], and Su et al.[128]. However, the coefficient under the logarithm in the denominator is different. We note that the difference is due to the fact that we account for the second term (i.e. $K_1(\tilde{k})\tilde{k}$) in the denominator; this allows us to obtain a more accurate agreement with the exact value of the effective stiffness term for a wider range of shear modulus contrasts. The different approaches for the approximation of Eq. (20) are discussed in Appendix A.

Then, substitution of Eq. (22) into Eq. (21) yields

$$\varepsilon = \frac{(\tilde{k})^2}{4} + \frac{1}{E_f(\tilde{k})^2}\frac{4G_m}{-\ln\left(\frac{e^{\gamma-\frac{1}{2}}}{2}\tilde{k}\right)}. \tag{23}$$

By minimizing Eq. (23) with respect to $\tilde{k}$, the critical wavenumber can be expressed as

$$\tilde{k}_{cr} = \left(\frac{4G_m}{(1+\nu_f)G_f}\right)^{1/4}\left[\frac{1+2\ln\left(\frac{e^{\gamma-\frac{1}{2}}}{2}\tilde{k}_{cr}\right)}{-\ln^2\left(\frac{e^{\gamma-\frac{1}{2}}}{2}\tilde{k}_{cr}\right)}\right]^{1/4}, \tag{24}$$

since the right-hand side of Eq. (24) changes very slowly with $\tilde{k}_{cr}$, Eq. (24) can be approximated as

$$\log(\tilde{k}_{cr}) = -0.265\log\left(\frac{G_f}{G_m}\right) + 0.265\log\left(\frac{4}{1+\nu_f}\right). \tag{25}$$

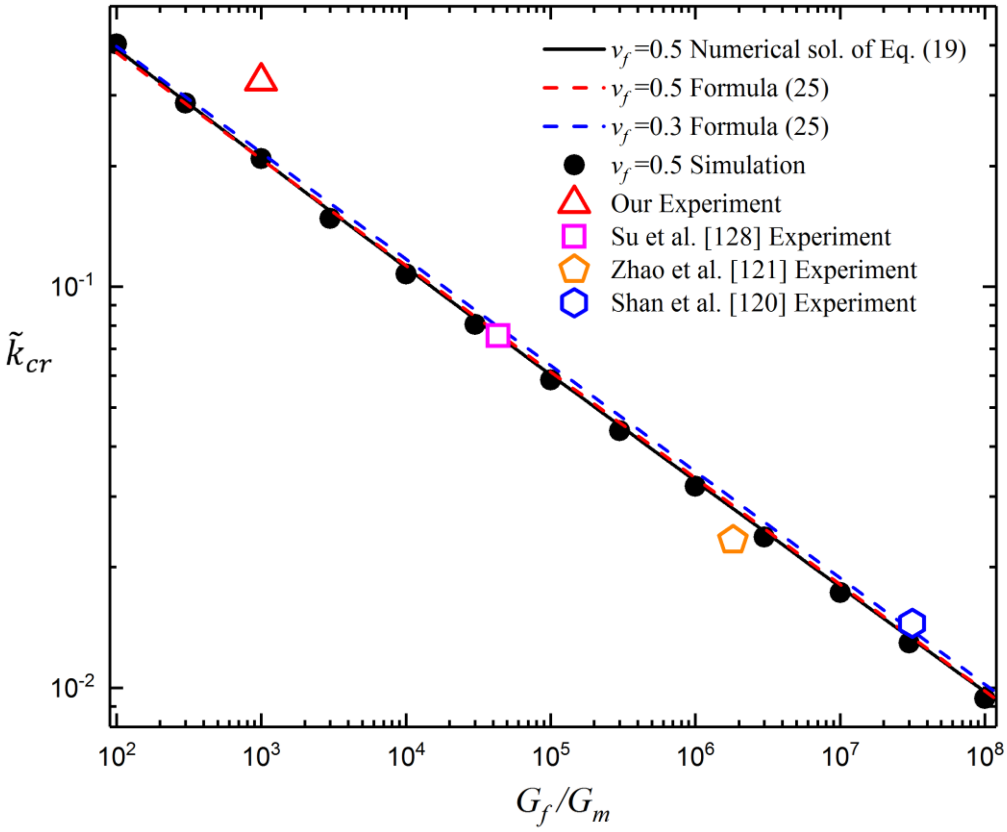

Figure 17. Normalized critical wavenumber $\tilde{k}_{cr}$ as a function of shear modulus contrast G_f/G_m.

Figure 17 shows the dependence of the normalized critical wavenumber on shear modulus contrast. We observe that the approximate expression given by Eq. (25) agrees well with the numerical solution of Eq. (19) (compare the dashed red line with the continuous black line in Figure 17), and the theoretical prediction for critical wavenumber shows good accordance with the experimental observations in a wide range of shear modulus contrast. We note that an increase in Poisson's ratio of the stiff fiber material leads to a slight increase in the normalized critical wavenumber (compare the dashed blue line with the dashed red line in Figure 17).

In addition, we perform the standard linear buckling analysis through the finite element numerical procedure implemented in COMSOL 5.2a; thus, we obtain numerically the dependence of normalized critical wavenumber on shear modulus contrast[3]. Figure 17 presents a comparison of the critical wavenumbers obtained by numerical simulations and theoretical analysis (compare the black circular points with black continuous curve), which additionally demonstrates that the obtained Eq. (25) provides an accurate prediction for the critical wavelength of a stiff fiber embedded in a soft matrix within a wide range of shear modulus contrast $\left(10^2 < G_f/G_m < 10^8\right)$.

3.3.2 Buckling of composites with periodically distributed fibers

Next, we investigate the instability induced pattern formations in composites with fibers periodically distributed in soft matrix. In particular, we study (a) symmetric case of square arrangement of periodically distributed fibers, and (b) case of rectangular arrangements of periodically distributed fibers. We present the experimental results for onset of instabilities in the periodic 3D-printed fiber composites and compare them with the numerical results. In order to numerically identify onset of instabilities and corresponding critical wavelengths, we employ Bloch-Floquet analysis, which is implemented by means of finite element code COMSOL. In the numerical analysis, we consider TP (soft matrix material) and DM (stiff fiber material) as nearly incompressible neo-Hookean materials ($\Lambda/G = 1000$, where Λ is the first Lame constant) with shear modulus contrast $G_f/G_m = 1000$. First, we apply macroscopic deformation by using the periodic displacement boundary conditions imposed on the faces of the unit cell. Once the deformed state is obtained, Bloch-Floquet conditions are imposed on the faces of the unit cell via $\mathbf{u}(\mathbf{X}+\mathbf{R})=\mathbf{u}(\mathbf{X})e^{-i\mathbf{K}\cdot\mathbf{R}}$, where **X** and **u** denote the position vector and displacement vector, respectively; **K** and **R** denote the Bloch wave vector and spatial periodicity in the reference configuration. The corresponding eigenvalue problem with the Bloch-Floquet boundary conditions is solved numerically until a non-trivial zero eigenvalue is detected at a certain deformation level. The corresponding compressive strain and wavenumber are identified as the critical strain ε_{cr} and critical wavenumber k_{cr}, respectively. For more detailed and illustrative description of the numerical instabilities analysis readers are referred to Slesarenko and Rudykh [37]. Note that we distinguish the microscopic and macroscopic (or long wave) instabilities. The microscopic instabilities are associated with onset of instabilities at a finite critical wavelength ($l_{cr}=2\pi/k_{cr}$, or non-zero critical wavenumber k_{cr},). The macroscopic (or long wave) instabilities are associated with the specific case of $k_{cr}\to 0$, when critical wavelength significantly exceeds the microstructure characteristic size. In this case the onset of macroscopic instabilities can be determined by evaluating the effective tensor of elastic moduli and applying the loss of ellipticity condition [26].

---

[3] In the numerical model, the soft matrix and stiff fiber are considered as linear elastic material; the geometry of the numerical model is considered as square brick. Considering the computational cost and accuracy, the height of the model is set as $H = 10l_{cr}$ (l_{cr} is estimated by Formula (25))); we note, however, that the choice of the height H in the numerical model may affect the critical wavelength. The side length of the square cross section of the model is set as $W = 150r$ to diminish the effect of the finite size of the sample on critical wavelength.

Case A. Square arrangement of periodically distributed fibers

Figure 18 illustrates the development of instability induced wavy patterns (a) and the dependence of critical wavenumber on stiff fiber volume fraction (b) for periodic fiber composite with square arrangement. The representative volume element is shown in the inset of Figure 18. We observe that the composites with stiff fiber volume fractions c_f=0.01 and 0.015 develop wavy patterns at smaller length scales (typically attributed to microscopic instabilities), while the composite with c_f=0.025 buckles in long wave mode (macroscopic instability). The periodic composite with c_f=0.02 can be arguably assigned to be at the transition zone between the composites that develop microscopic and macroscopic instabilities. Thus, we experimentally observe the transition of the instability induced patterns from small wavelength wavy pattern to long wave mode, as the fiber volume fraction increases. For completeness, we show the dependence of the critical wavenumber on stiff fiber volume fraction obtained through the Bloch-Floquet numerical analysis superimposed on the deformed state in Figure 18. Here and thereafter, the hollow and solid symbols correspond to the microscopic and macroscopic instabilities, respectively. The circles and triangles denote the numerical and experimental results for periodic fiber composite, respectively; the dashed blue line corresponds to the theoretical result of single fiber composite obtained by Eq. (25). We observe a remarkable agreement of the experimental observations and numerical simulation results. Both experimental observations and numerical simulations show that the critical wavenumber decreases with an increase in stiff fiber volume fraction. When the stiff fiber volume fraction exceeds a certain threshold value (c_f ≈0.02 for $G_f/G_m = 1000$), the fiber composites start developing instabilities in the long wave mode upon achieving the critical level of compressive deformation. The interactions between stiff fibers weaken with a decrease in stiff fiber volume fraction, therefore, we observe that the critical wavenumber of periodic fiber composite in the dilute limit attains the value corresponding to single fiber system (compare the circular points with dashed blue line in Figure 16(b)).

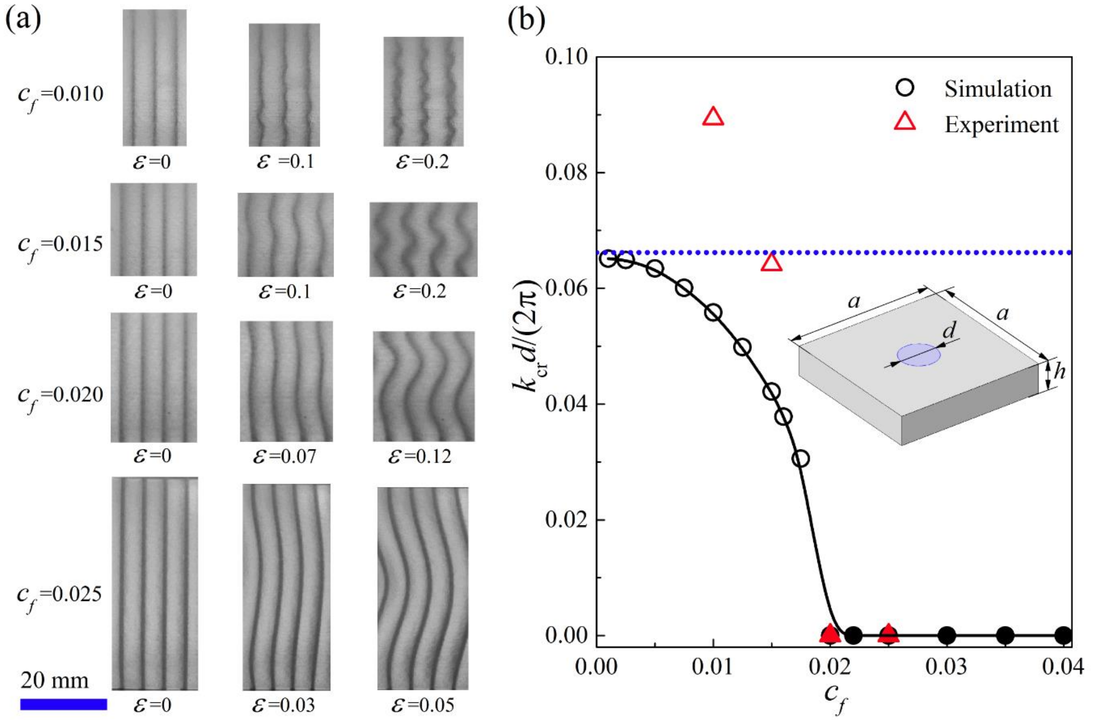

Figure 18. Development of wavy patterns in fiber composites with square arrangement (a); dependence of critical wavenumber on fiber volume fraction (b). The dotted horizontal line in (b) corresponds to the single fiber analytical result (Eq. (25)).

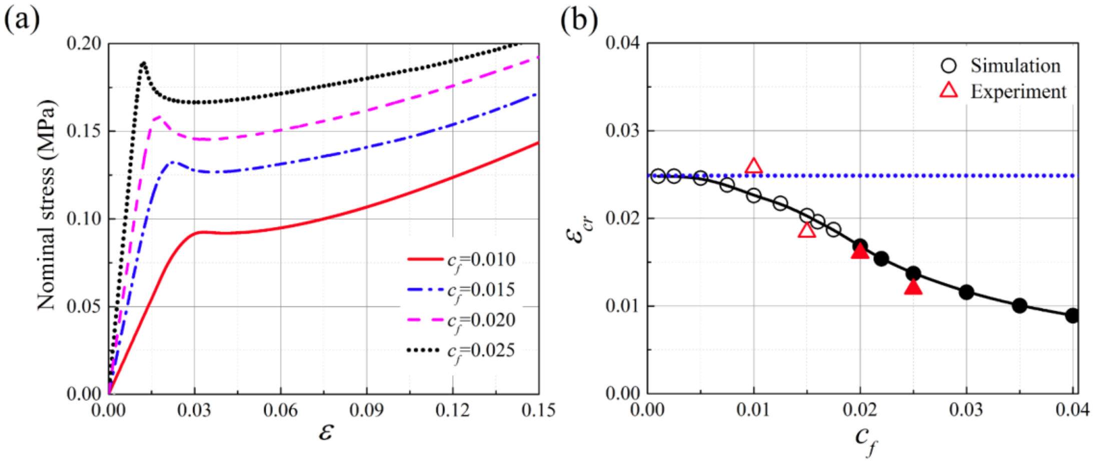

Figure 19. Experimental stress-strain curves for fiber composites with square arrangement (a), and dependence of the critical strain on fiber volume fraction (b). The dotted horizontal line in (b) corresponds to the single fiber analytical result (Eq. (23)).

Figure 19 shows the experimental stress-strain curves (a), and the dependence of the critical strain (b) for periodic fiber composites with square arrangement. As expected, the stress-strain curves (see Figure 19(a)), show that the fiber composites exhibit softening upon achieving the critical strain at which the stiff fibers buckle into wavy patterns. The critical strain is observed to decrease with an increase in stiff fiber volume fraction as shown in Figure 19(b). Similar to the observation for critical wavenumber, the critical strain for periodic fiber composites at low stiff fiber volume fraction approaches the critical strain of single fiber system (denoted by the horizontal dotted line in Figure 17(b)).

Case B. Square arrangement of periodically distributed fibers

Next, we investigate the influence of fiber arrangements on the buckling behavior of the periodic fiber composites. In particular, we consider fiber composite with rectangular periodic unit cell. The representative volume element, characterized by aspect ratio $\eta = b/a$, is shown in the inset of Figure 20. Note that while the aspect ratio is varied, the fiber volume fraction is kept fixed at the value c_f=0.01. In our experiments, the fiber diameter was identical for all composite specimens with different aspect ratios; we also kept fixed the dimensions of the considered specimens and the number of stiff fiber. The development of the wavy pattern in fiber composites with rectangle arrangement is shown in Figure 20 (a). Similarly to the previously discussed case of periodic square arrangements, the periodic composites with rectangular arrangements of periodic fibers develop wavy patterns, and the amplitude of the wavy pattern significantly increases with an increase in compressive load.

However, a change in the periodicity aspect ratio leads to certain cooperative buckling behavior of the fibers such that the wavy patterns develop in the direction, where fibers are close to each other (see the cases for η=4, 9 in Figure 20(a)). Figure 20(b) presents the dependence of critical wavenumbers on aspect ratio. We find that experimental and numerical results show good accordance, especially in the range of high aspect ratio. We also observe that the critical wavenumber decreases with an increase in aspect ratio, and this effect is more significant in the range of small aspect ratio.

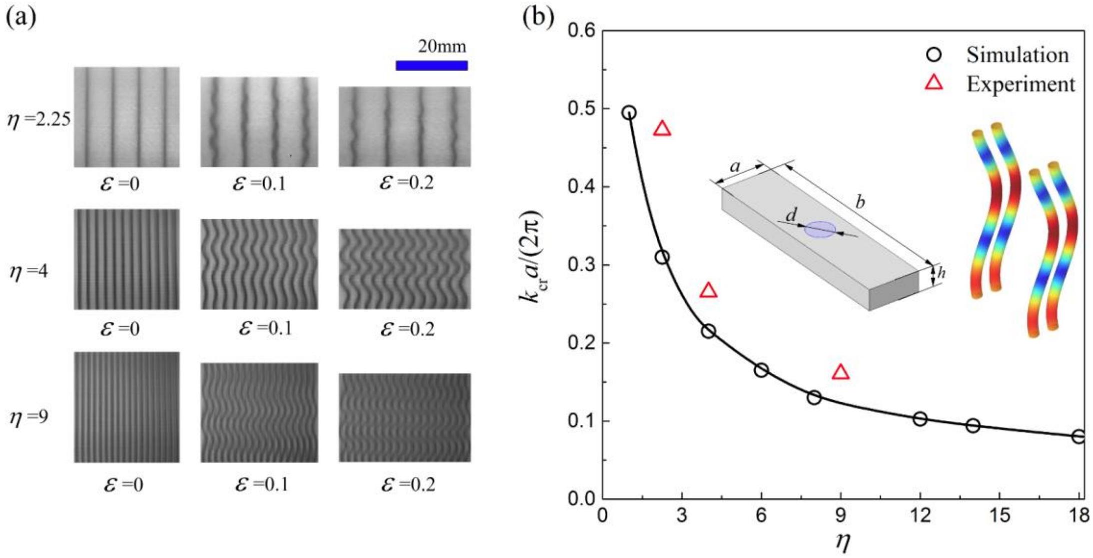

Figure 20. Development of wavy patterns in fiber composites with rectangle arrangement (a); dependence of critical wavenumber on the periodicity aspect ratio (b).

Figure 21 presents the experimental stress-strain curves (a), and the dependence of critical strain (b) for periodic fiber composites with rectangle arrangement. Similar to the observation for fiber composite with square arrangement, we observe that the buckling of the stiff fiber decreases the load capacity of fiber composite (see Figure 21(a)). In the stable regime, the stiffness of the composites with different periodicity aspect ratios is nearly identical. However, the onset of buckling and the postbuckling behavior changes significantly with a change in the periodicity aspect ratio. Figure 21(b) shows the dependence of the critical strain on aspect ratio. We observe that the critical strain decreases with an increase in aspect ratio; thus, the composites with higher aspect ratio require lower levels of compressive deformation to trigger buckling.

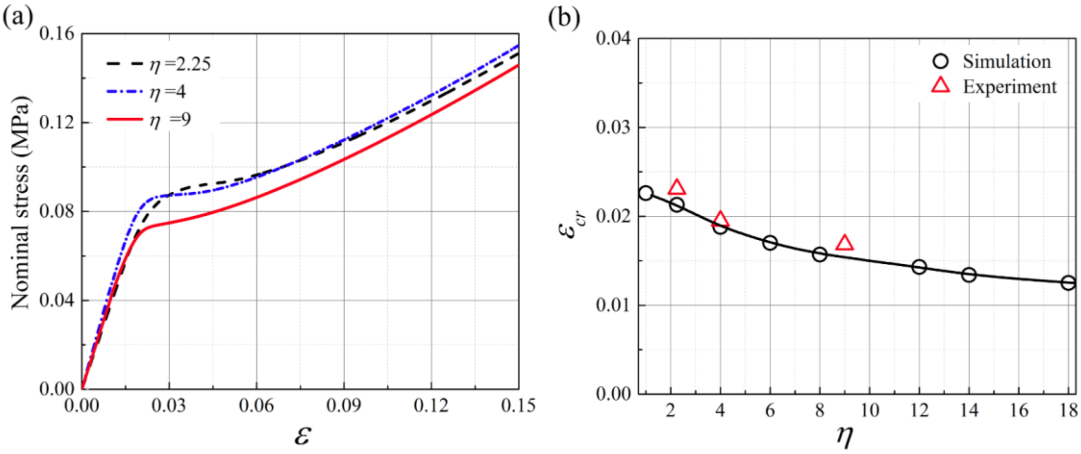

Figure 21. Experimental stress – strain curves for fiber composites with rectangle arrangement (a), and dependence of the critical strain on the periodicity aspect ratio (b).

3.4 Summary

We have examined the elastic buckling of single stiff fiber and periodically distributed stiff fiber embedded in a soft matrix subjected to axial compressive loads. First, we experimentally observed the buckling process of a single fiber embedded in soft matrix. We have found that the critical wavelength and the amplitude of the wavy pattern increase with an increase in fiber diameter, and the critical wavelength has a linear dependence on the stiff fiber diameter. Then, based on the Winker foundation model, we derived an explicit expression to predict the buckling wavelength, and further verified the derived expression in a wide range of shear modulus contrast by comparing to experimental data and numerical simulations.

Next, we investigated the elastic buckling of composites with periodically distributed fibers. We experimentally observed the transition of the instability induced patterns from small wavelength wavy pattern to long wave mode, along with the increase of fiber volume fraction. For fiber composites with periodic square arrangement, both experimental and numerical results have shown that the critical wavenumber and critical strain decrease with an increase in fiber volume fraction. For fiber composites with rectangular arrangements, we have observed that the stiff fibers develop a cooperative buckle mode in the direction, where the fibers are close to each other; and an increase in aspect ratio leads to a significant decrease in critical wavenumber and critical strain. Thus, various out-of-plane postbuckling wavy patterns can be tailored through the design of in-plane fiber arrangements. These findings may be used in the design of reconfigurable functional materials, potentially extending the ideas to electro- [135,136] and magnetoactive [137–140] composite materials, and tunable acoustic metamaterials [65,68,98], and other bistable and 4D-printed functional materials [141–143].

Chapter 4

Domain formations and pattern transitions via instabilities in soft particulate composites*

Experimental observations of domain formations and pattern transitions in soft particulate composites under large deformations are investigated. The system of stiff inclusions periodically distributed in soft elastomeric matrix experiences dramatic microstructure changes upon the development of elastic instabilities. In the experiments, the formation of microstructures with antisymmetric domains and their geometrically tailored evolution into a variety of patterns of cooperative particle rearrangements are observed. Through experimental and numerical analyses, it is shown that these patterns can be tailored by tuning the initial microstructural periodicity and concentration of the inclusions. Thus, these fully determined new patterns can be achieved by fine tuning of the initial microstructure.

---

* Based on the published paper: Li J, Pallicity TD, Slesarenko V, Goshkoderia A, Rudykh S. Domain Formations and Pattern Transitions via Instabilities in Soft Heterogeneous Materials. Adv Mater 2019;31:1807309.

4.1 Introduction

Soft materials can develop large deformations in response to various external stimuli, such as mechanical loading [1], electrical [2,144] and magnetic fields [3,145,146], heat [4,143], and light [5,147], thus providing rich opportunities for the design of responsive and reconfigurable functional materials with novel and unusual properties [72,148,149]. Moreover, the performance of soft materials can be further empowered via the instability phenomenon giving rise to dramatic structural changes [18]. This approach enables diverse applications including flexible electronics [7,150–153], optical [154] and acoustic [62,155,156] switches, auxetic materials [14], surface pattern control [157], and soft robotics [9,158]. The instability-induced microstructure transformations discovered in the soft system with periodic voids [39,71] have led to the development of programmable mechanical metamaterials [48,49], switchable auxetic materials [19,45,46,159], color displayers [160], wave absorbers [6,20,68,69], and actuators [21]. To predict the onset of elastic instabilities and associated microstructure transformations in soft materials, the nonlinear elasticity framework of small perturbations superimposed on large deformations is employed [70]. Based on the homogenized material response, macroscopic instability or so-called long wave instability can be predicted [30,31]. The macroscopic instability corresponds to a special limit in the Bloch-Floquet analysis [23,26] that allows detecting the onset of instability and corresponding mode at different wavelengths. This approach has been successfully used to theoretically predict instability-induced microstructure transformations in various soft systems that have been realized in experiments

[19,39,45,46,159]. Furthermore, recent development in advanced material fabrication techniques, such as 3D printing [161], interference lithography [43], allows the realization of pre-designed soft microstructures at various length-scales, and extending applications of these intrinsic pattern transformations in reconfigurable materials.

Here we report our experimental observations of the formation of anti-symmetric domain, and its geometrically tailored evolution into a variety of patterns with cooperative particle rearrangements in soft composites under large deformations. We study the system of stiff inclusions periodically distributed in a soft elastomeric matrix experiencing dramatic microstructure transformations upon the development of elastic instabilities. We experimentally realize the instability-induced modes of transformative microstructures from domain formations to cooperative new patterns of particles rearranged in wavy chains, depending on the initial microstructural periodicity and concentration of the inclusions. The numerical Bloch-Floquet instability analysis is employed to investigate the effect of geometrical parameters and material compositions on the composite buckling behaviors giving rise to the formations of various patterns.

4.2 Experiments and simulations

Soft composite samples with stiff circular inclusions periodically distributed in a soft elastomeric matrix were fabricated with an Object Connex 260-3 3D printer. A schematic illustration of the composite microstructure is shown in Figure 22(a). The geometric parameters are defined through periodicity aspect ratio $\eta = w/h$, and inclusion spacing ratio $\xi = d/h$; where w and h denote the unit cell width and height, respectively; d is the diameter of the inclusions. The soft matrix was printed in TangoBlack Plus resin (shear modulus $\mu_m = 0.2$ MPa), the stiff circular inclusions were printed in VeroWhite resin (shear modulus $\mu_i = 600$ MPa). We first examine the behavior of the soft composites with large spacing ratio and small periodicity aspect ratio, where the domain formations or long wave modes are predicted. In particular, the specimens with $\xi = 0.8, \eta = 1.5$; $\xi = 0.8, \eta = 1.0$; and $\xi = 0.9, \eta = 1.5$ were tested experimentally. Next, the effect of periodicity aspect ratio and the inclusion spacing ratio on the composite behaviors was experimentally investigated separately. Two series of specimens were fabricated: (A) the composites with fixed spacing ratio $\xi = 0.8$, and varying periodicity aspect ratio η =1.5, 4, 8, 24 and (B) the composites with fixed aspect ratio $\eta = 3$, and inclusion spacing ratio $\xi = 0.7$, 0.8, 0.9, 0.95. The in-plane dimensions of the specimens were 60 × 90 mm (width × height), and the out-plane thickness of the specimens was $t = 5$ mm. The unit cell height (defined in Figure 22(a)) for all specimens was fixed as $h = 2.5$ mm. To diminish the influence of boundary effects on buckling behaviors of the composites, all specimens were printed with a TangoBlack Plus resin boundary layer of 25-mm width.

The uniaxial compression tests were performed using a Shimadzu EZ-LX testing machine. The deformation in the thickness direction was prevented by placing the specimens in a transparent parallel fixture to maintain the plane strain conditions. The specimens were compressed in Y direction at a constant velocity of 1 mm/minute. During the test, the compression force and displacement were recorded by the data acquisition system; the deformation processes were captured by the high-resolution charge-coupled device (CCD) camera. Multiple samples with identical material properties and geometries were printed and tested to ensure that the observed phenomenon is independent of the individual tests.

Simulations are performed by means of the finite element code (COMSOL 5.2a). The soft matrix and stiff inclusions are modeled as nearly incompressible neo-Hookean materials. The plane-strain conditions are imposed in the simulations. To detect the onset of instabilities in the periodic particulate soft composite and the associated critical strain ε_{cr} and critical wavenumber k_{cr}, we conduct the Bloch-Floquet analysis superimposed on the deformed state [37,68]. The primitive unit cell (as shown in Figure 22(a)) is constructed, and the corresponding displacement boundary conditions are imposed on the unit cell edges. The analysis is performed in two steps: (1) first, we apply the averaged macroscopic deformation through imposing the corresponding periodic displacement boundary conditions on the unit cell edges to obtain the deformed state; (2) we superimpose the Bloch-Floquet boundary conditions on the unit cell edges, and solve the corresponding eigenvalue problem for a range of wavenumbers. These steps are repeated until a non-trivial zero eigenvalue is detected at a certain applied deformation level. Then, the corresponding critical strain and wavenumber are identified. Note that the macroscopic instabilities are detected when $k_{cr} \rightarrow 0$ [26]. A more detailed description of the simulations can be found in Appendix B.

4.3 Results and discussion

First, we examine the behavior of the soft composite configurations giving rise to domain formations; these microstructural configurations correspond to the soft composites with large particle spacing ratio and small periodicity aspect ratio. Figure 22(c-e) shows the instability-induced patterns in soft composites with $\xi = 0.8, \eta = 1.5$ (c); $\xi = 0.8, \eta = 1.0$ (d); $\xi = 0.9, \eta = 1.5$ (e) at applied strain levels $\varepsilon = 0.15$ (c), 0.11 (d), 0.08 (e). Corresponding critical strains in the composites are $\varepsilon_{cr} = 0.088$ (c), 0.089 (d), 0.038 (e), respectively. Figure 22(c, d) shows that the composites with aspect ratio $\eta = 1.0$, 1.5 (with fixed particle spacing ratio $\xi = 0.8$) form anti-symmetric domains upon the development of instabilities. Interestingly, similar domains or twin patterns were also observed in different systems such as martensitic phase transformations [162,163], liquid crystals [164,165], nematic elastomers [166,167], stiff thin films bonded on a soft substrate [168–170]. The observed domains (marked by the dashed green lines) consist of approximately five unit cells; the particles within the domain align in straight lines with the orientations (or directors) marked by red arrows. The domain orientation changes with the applied deformation as illustrated in Figure 22(b) showing the experimentally observed domain orientation evolutions. Prior to the onset of instability, the inclusions are aligned in the vertical straight lines corresponding to the zero domain orientation angle. When the applied deformation exceeds the critical strain, the domains start forming, and the orientation angle rapidly increases with an increase in compressive strain. Finally, we note that the increase in particle spacing ratio leads to the transformation of the instability-induced pattern into cooperative particle rearrangements as wavy chains (see Figure 22(e)) for the soft composite with $\eta = 1.5$, $\xi = 0.9$). The period of wavy chains consists of approximately 20 inclusions.

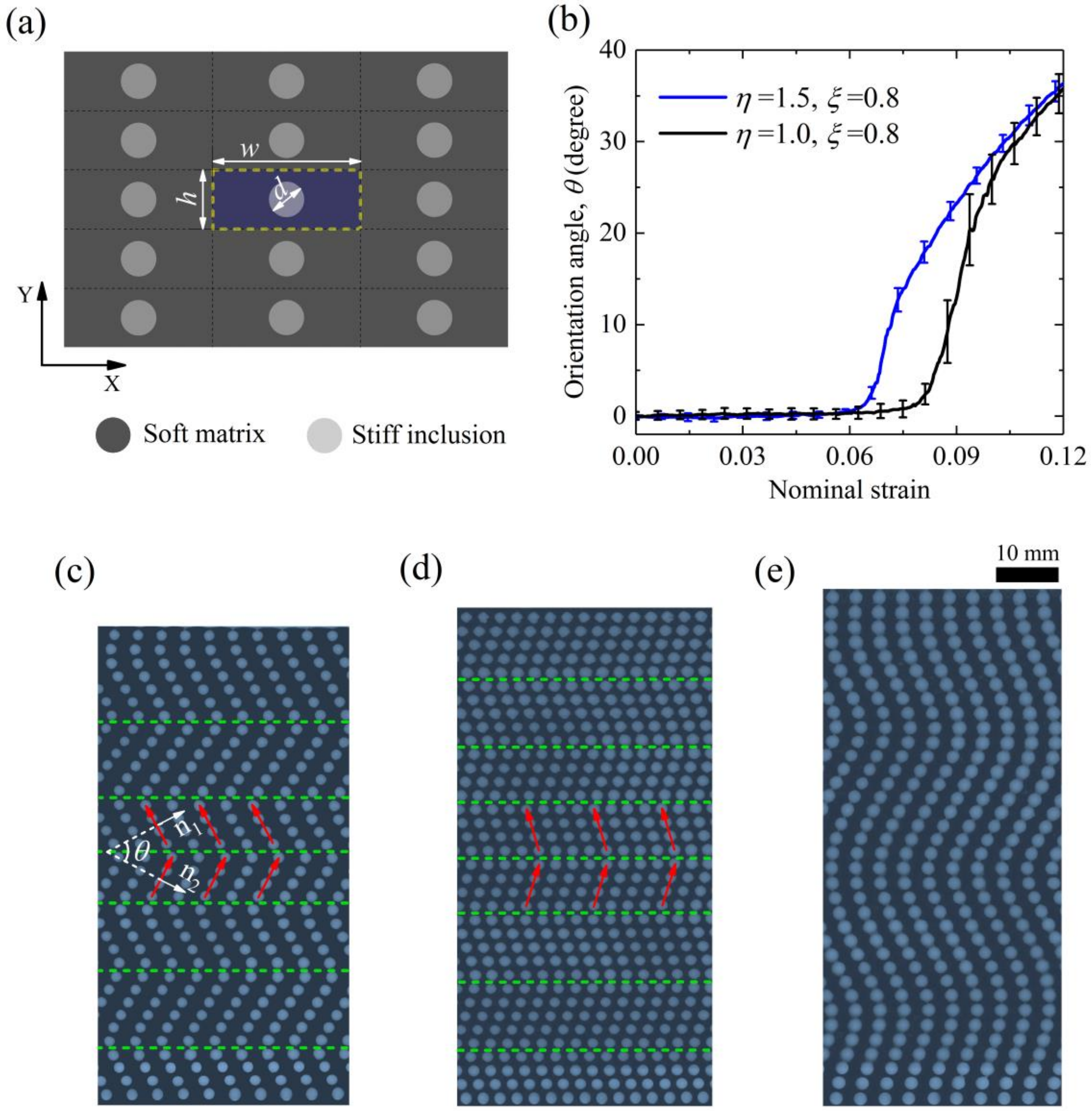

Figure 22. (a) Schematic composite microstructure with stiff circular inclusions periodically distributed in a soft matrix, the primitive unit cell is highlighted in light navy color. (b) The dependence of domain orientation angle on the applied strain. Experimental images of instability-induced domain formations (c, d), and periodic wavy particle chains (e); the results are given for the composites with $\xi = 0.8, \eta = 1.5$ (c), $\xi = 0.8, \eta = 1.0$ (d), $\xi = 0.9, \eta = 1.5$ (e) at strains $\varepsilon = 0.15$ (c), 0.11 (d), 0.08 (e).

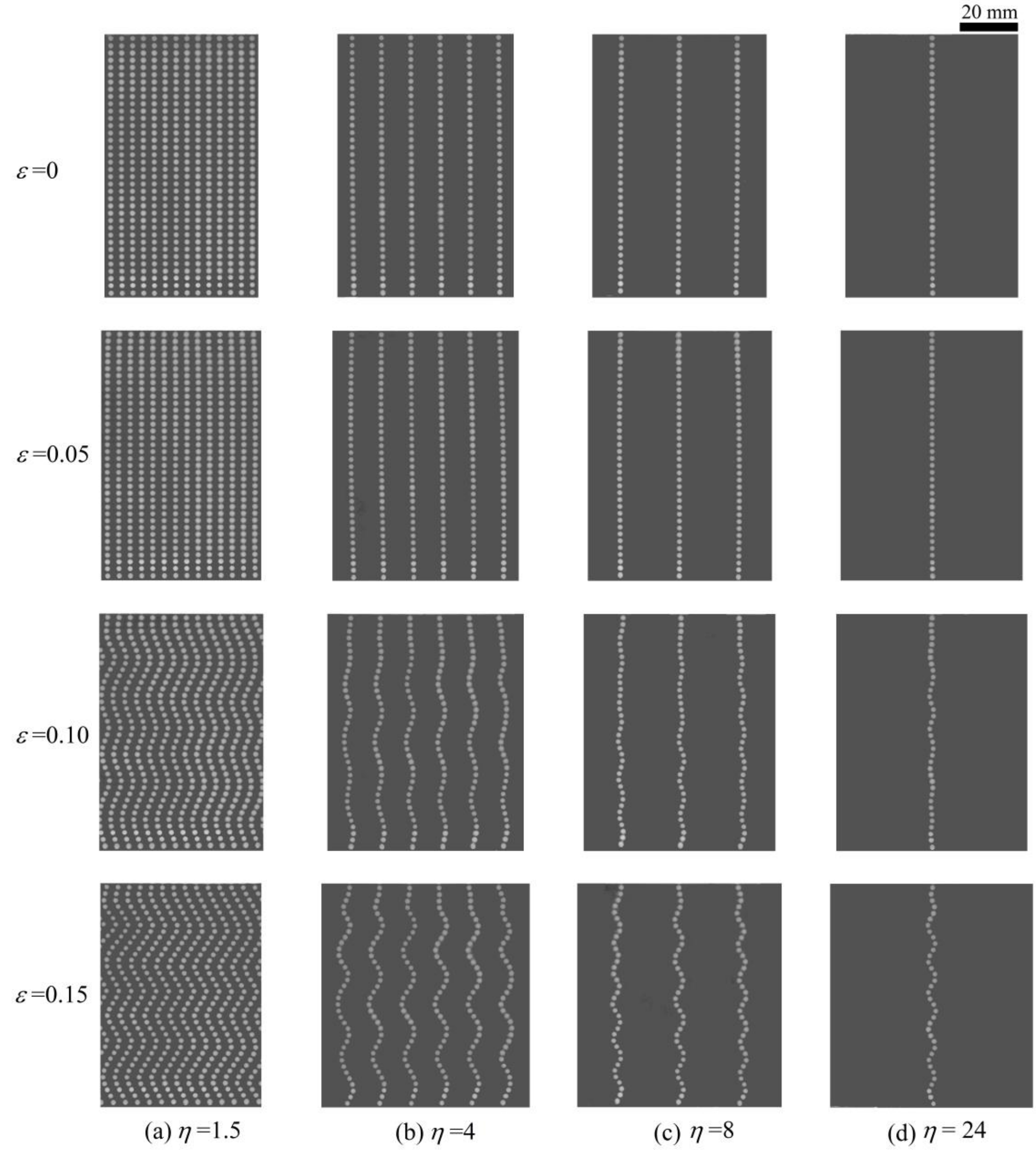
20 mm
ε=0
ε=0.05
ε=0.10
ε=0.15
(a) η=1.5
(b) η=4
(c) η=8
(d) η = 24

Figure 23. Deformation sequences of the composites with varying periodicity aspect ratios loaded at different deformation levels. The inclusion spacing ratio is fixed as $\xi = 0.8$.

To identify the key parameters dictating the instability-induced pattern evolutions, we analyze the soft composite behaviors with varying initial microstructure geometrical parameters. First, we examine the role of the periodicity aspect ratio on the soft composite behavior, while keeping the inclusion spacing ratio fixed. Figure 23 shows the deformation sequences of the composites with various periodicity aspect ratios at different deformation levels. The results are given for the composites with periodicity aspect ratio $\eta = 1.5$, 4, 8, 24 (from the left to the right columns); the inclusion spacing ratio is fixed $\xi = 0.8$. We observe that the composite microstructure experiences a rapid change upon exceeding the critical strain. For the composite with relatively small periodicity ratio $\eta = 1.5$ (see Figure 23(a)), we observe that the development of instability results in the stiff inclusions rearranged into anti-symmetric domains, similar to the one shown in Figure 22(d). We find that the director orientation (denoted by red arrows in Figure 22(c, d)) of each domain rotates with further increase in applied deformation. The composites with $\eta = 4$, 8, 24, develop different patterns of periodic wavy chains of particles upon instabilities (see Figure 23(b-d)). Thus, the instability induced patterns exhibit a transition from the domain formations to the appearance of wavy patterns. Moreover, we find that the length of the formed wavy chain patterns decreases with the increase in periodicity aspect ratio; for example, the period of wavy chain for the composite with $\eta = 4$ consists of approximately eight inclusions, while the composite with $\eta = 8$ forms a period with approximately five inclusions. Furthermore, we note that the evolution of the instability-induced pattern transformations for the composites with η =8, 24 is almost identical (compare Figure 23(c, d)). This is due to the fact that the interactions between the columns of stiff inclusions become weak in composites with large periodicity aspect ratio, and the post-buckling behavior of such composites approaches the one corresponding to a single column of particle system (see Figure 23(d)).

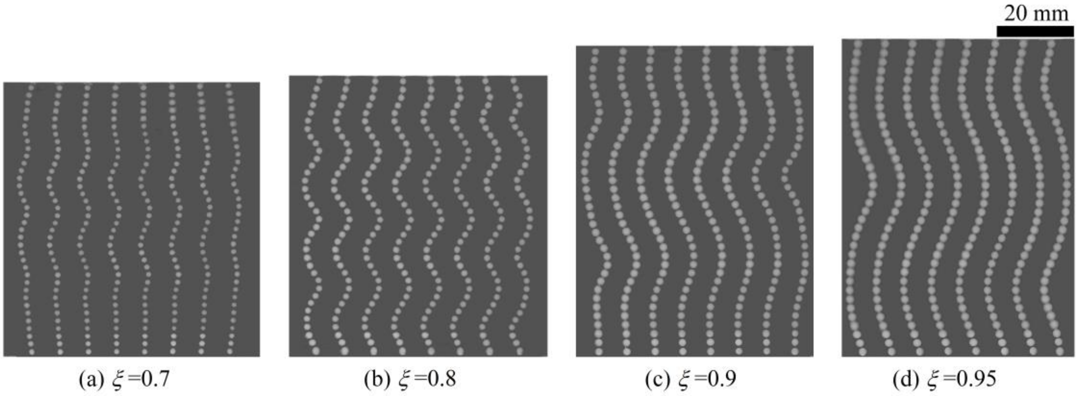

Figure 24. Buckled configurations in soft composites with various inclusion spacing ratios $\xi = 0.7, 0.8, 0.9, 0.95$; and fixed periodicity aspect ratio $\eta = 3$. The results are given at strain levels $\varepsilon = 0.17$ (a), 0.15 (b), 0.06 (c), and 0.04 (d).

Next, we illustrate the role of the inclusion spacing ratio in the soft composite behavior. Figure 24 presents the instability-induced patterns in the composites with various inclusion spacing ratios $\xi = 0.7$ (a), 0.8 (b), 0.9 (c), 0.95 (d), and fixed periodicity aspect ratio $\eta = 3$. The results are shown for the composites with applied strain levels: $\varepsilon = 0.17$ (a), 0.15 (b), 0.06 (c), and 0.04 (d). We observe that all composites develop wavy-like patterns, and the length of the wavy-like pattern increases with the increase in inclusion spacing ratio. The wave length of the instability-induced pattern in the composite with $\xi = 0.95$ is significantly larger than the characteristic size of its unit cell, similar to the one shown in Figure 22(e)); these patterns can be attributed to the transition to the macroscopic or long wave mode. Remarkably, these pattern transformations are fully reversible, since the composites restore their initial states after removing the applied load.

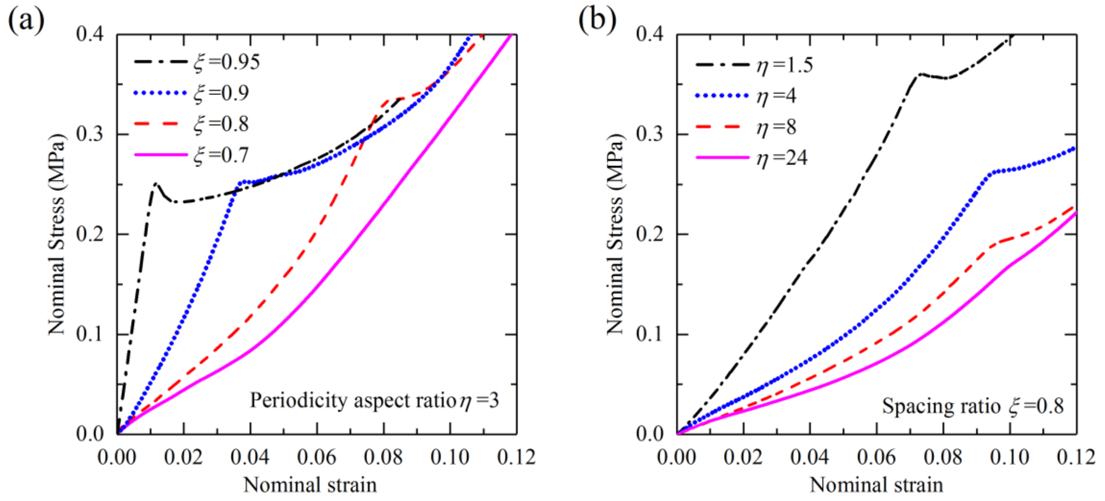

Figure 25. Experimental stress-strain curves for the composites with various spacing ratios (a) and various periodicity aspect ratios (b).

The experimental stress-strain curves for the composites with various spacing ratios (a) and various periodicity ratios (b) are shown in Figure 25. Prior to the onset of instability, the composites with larger spacing ratio and/or smaller aspect ratio possess stronger reinforcement and exhibit stiffer responses. When the critical deformation level is achieved, the softening behavior is observed due to the instability-induced microstructure transformations; the softening effect weakens for the composites with smaller spacing ratio and/or larger periodicity aspect ratio. In particular, for the composite with $\xi = 0.7, \eta = 3$, only slight softening is observed at ε =0.152; and for the composite with single column of inclusions (i.e., $\eta = 24$), the softening behavior is barely detectable, though the instability can be readily identified from visual observation of the pattern change. Thus, the composite response can be described by two effective convex strain energy functions merged at the onset of instability, and it is characterized by the reduced effective stiffness in the postbuckling regime.

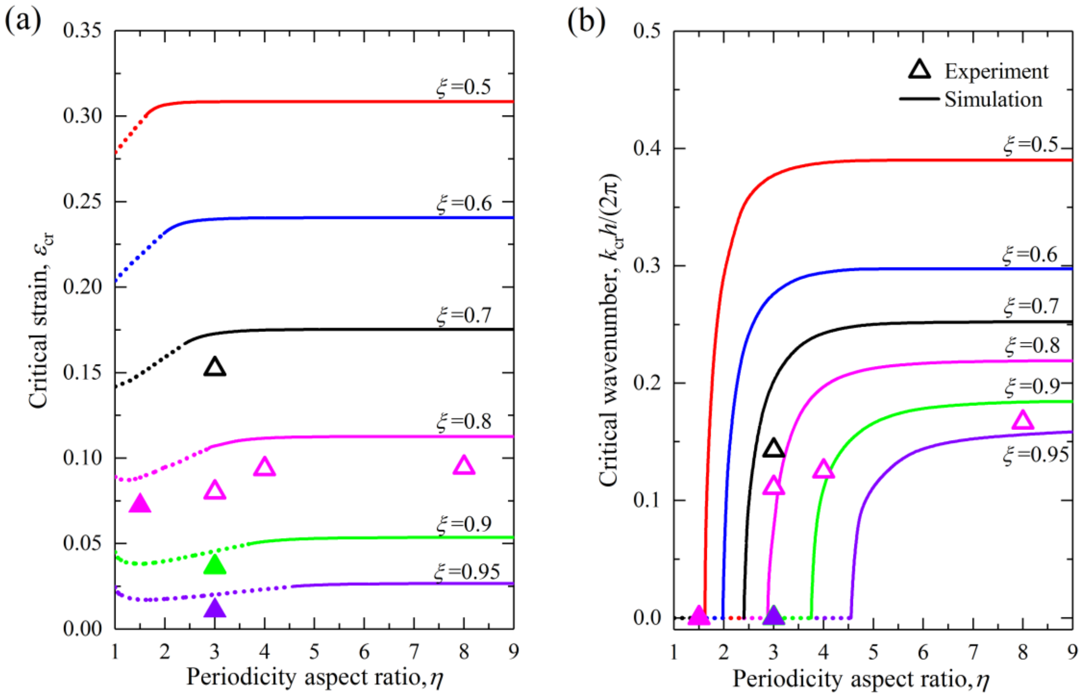

Figure 26. The dependence of critical strain (a) and critical wavenumber (b) on periodicity aspect ratio for the composites with various spacing ratios. The dotted curves and filled triangular symbols correspond to macroscopic instabilities, while continuous curves and hollow triangular symbols correspond to microscopic instabilities.

Next, we summarize our numerical predictions together with experimental observations of the dependence of the critical strain (a) and critical wavenumber (b) as functions of periodicity aspect ratio for the composites with various inclusion spacing ratios in Figure 26. The dotted and continuous curves correspond to the numerically predicted macroscopic and microscopic instabilities, respectively. We use the hollow and filled triangles to denote the experimentally observed critical strains and wavelengths (wavenumbers) corresponding to the numerically detected microscopic and macroscopic instabilities, respectively. The experimental critical strain is measured as the deformation level at which the onset of material softening is detected.

We observe a qualitative agreement between the numerically predicted trends and experimental results. Interestingly, the domain formation is observed, when the numerical analysis detects the instability at a special limit of the so-called macroscopic instabilities ($k_{cr} \rightarrow 0$). The macroscopic instability analysis can only detect the onset of instabilities, however, it cannot provide the information on the characteristic wavelength of the instability-induced domains. We note, however, the interesting correspondence of the prediction of the macroscopic instabilities and the new domain formations observed in the experiments. We observe that both simulations and experiments indicate that the composites with higher inclusion spacing ratio are more prone to instabilities and buckle earlier (see Figure 26(a)). The critical strain dependence on the periodicity aspect ratio changes as the spacing ratio is increased. For the composite with small spacing ratio (for example, $\xi = 0.5$), critical strains are found to increase with the increase in the periodicity aspect ratio. When the spacing ratio attains a certain value, the dependence changes and a minimum critical strain is observed at a certain value of periodicity aspect ratio, depending on the inclusion spacing ratio. For example, for the composites with $\xi = 0.9$, the minimum critical strain ($\varepsilon_{cr}^{\min} = 0.038$) occurs at $\eta \approx 1.4$. Moreover, we note that the experimental critical strains are observed to be lower than the numerical results. This may be due to various factors, such as the boundary effects for the finite-sized specimens tested in experiments, which are not considered in the numerical simulations for the infinite periodic composites [14,39,71].

Figure 26(b) shows the dependence of critical wavenumber on the periodicity aspect ratio for the soft composites with various fixed inclusion spacing ratios. Our simulations predict that the composites with high spacing ratio and/or low periodicity aspect ratio develop macroscopic instability (namely, $k_{cr} \rightarrow 0$); these cases correspond to the experimentally observed domain formations. Both experiments and simulations show that an increase in periodicity aspect ratio, or a decrease in inclusion spacing ratio can result in a transition from domain formations to the appearance of periodic wavy chains of particles. Moreover, both critical strain and critical wavenumber are found to be barely influenced by the change in the periodicity aspect ratio when it is large enough ($\eta > 6$ for the composites with inclusion spacing ratio $\xi = 0.8$); this agrees well with our experimental observations for the composites with $\eta = 8$ and 24, showing similar responses (compare Figure 23(c, d)). These numerical predictions, together with the experimental observations, indicate that the composites with more dense assemblies of the stiff particles tend to develop the twinning domains (upon onset of instabilities); apparently, these patterns are energetically favorable over the wavy patterns in these configurations. Once the distance between the columns of particles is increased, the composites start to exhibit laminate-like buckling behavior – with the effective stiffer layer formed from the column of stiff inclusions – developing the wavy patterns with various wavelengths.

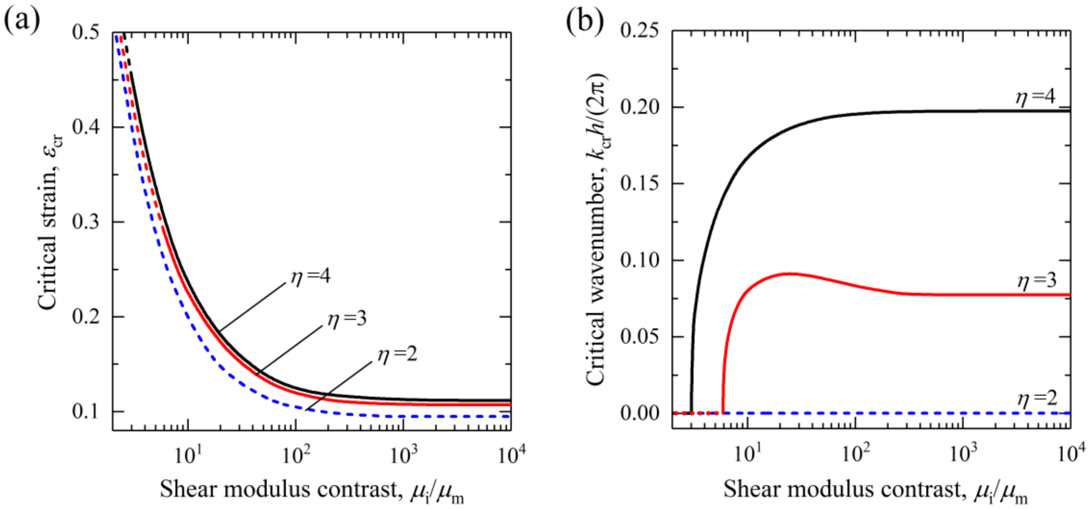

Figure 27. The dependence of critical strain (a), and critical wavenumber (b) on inclusion-to-matrix shear modulus contrast μ_i/μ_m. The composite spacing ratio is fixed as $\xi = 0.8$. Dotted and continuous curves correspond to macroscopic and microscopic instabilities, respectively.

Finally, we numerically examine the influence of the material composition on the composite buckling behavior. Figure 27 presents the dependence of (a) critical strain, and (b) critical wavenumber on the inclusion-to-matrix shear modulus contrast μ_i/μ_m for the composites with periodicity aspect ratio $\eta = 2, 3, 4$ and fixed spacing ratio $\xi = 0.8$. We observe that the composites with higher shear modulus contrast buckle earlier (at lower strains); interestingly, an increase in the shear modulus contrast may result in the buckling mode switch from macroscopic instability to microscopic instability (see Figure 27(b)) depending on the initial microstructure parameters. For example, the switch of the buckling mode from macroscopic to microscopic instability occurs at $\mu_i/\mu_m \approx 5.9$ for the composite with periodicity aspect ratio $\eta = 3$, and initial spacing ratio $\xi = 0.8$. In the range of low shear modulus contrasts, the inclusions are able to develop significant deformations, and change their shape resulting in strong stabilization of the composite, and in significant changes in the buckling modes developing at large strains.

4.4 Summary

In conclusion, we have observed experimentally the formation of anti-symmetric domains, and the evolution of the instability-induced patterns into periodic wavy chains. These pre-determined patterns and transitions are dictated by the initial microstructure geometrical parameters; thus providing the means to tailor the transformative behavior of soft composites, and to pre-design a variety of switchable functions. The observed domain formation phenomenon in the soft composites can be used for designing materials with switchable functionalities drawn from different length scales. The material design can be further facilitated through numerical computations, as we have shown, the employed numerical method predicts the phenomenon, and can guide towards the desired functionalities achieved through tailored microstructures. We note, however, that the computationally macroscopic instability analysis alone is not enough, and it requires to be accompanied with the full microscopic analysis for the reliable predictions of the domain formations in soft composites. This approach can be combined with the energy convexity consideration along the loading path to identify the energetically preferable post-buckling configurations of the soft composites [171]. We note that the emergence of the domains happens in the composite configurations with dense population of the stiff inclusions. However, when the particle frustration is relaxed – as the distance between the columns of inclusions increases – the composites develop wavy patterns resembling the buckling behavior in soft laminates with the effective stiff layer formed from stiff particle columns. Apparently, the domain patterns are energetically preferable over the wavy patterns in the composite configurations with dense concentration of the stiff inclusions; interestingly, the surface patterns observed in stiff-thin-film/soft-substrate systems show similar behaviors and transitions from twining patterns to wrinkles. Moreover, the formation of the domains in the soft composites is reminiscent of the structures emerging in different systems such as twin patterns in martensitic phase transformations, liquid crystals, and nematic elastomers.

Our findings open new ways for developing the reconfigurable mechanical metamaterials that can find applications in a large variety of fields from acoustic metamaterials, actuators, and soft robotics to morphing devices remotely controlled by external fields for biomedical applications. Thus, for example, the observed switchable behavior can be potentially induced by electric [172] or magnetic [173] fields, or thermally [174], extending application of the phenomenon in a broad class of architected active materials. Furthermore, these controllable microstructure transformations can be potentially merged at different length scales with other material systems, such as laminates [175], periodic porous [39] and bistable structures [176] providing the opportunity for the design of new hierarchical materials that draw their functionalities from different wavelengths.

Chapter 5

Instability-induced pattern transformations in multiphase soft composites[*]

We investigate the instability-induced pattern transformations in 3D-printed soft composites consisting of stiff inclusions and voids periodically distributed in a soft matrix. These soft auxetic composites are prone to elastic instabilities giving rise to negative Poisson's ratio (NPR) behavior. Upon reaching the instability point, the composite microstructure rearranges into a new morphology attaining NPR regime. Remarkably, identical composites can morph into distinct patterns depending on the loading direction. These fully determined instability-induced distinct patterns are characterized by significantly different NPR behaviors, thus, giving rise to enhanced tunability of the composite properties. Finally, we illustrate a potential application of these reversible pattern transformations as tunable acoustic-elastic metamaterials capable of selectively filtering low frequency ranges controlled by deformation.

---

[*] Based on the published paper: Li J, Slesarenko V, Rudykh S. Auxetic multiphase soft composite material design through instabilities with application for acoustic metamaterials. Soft Matter 2018;14:6171–80.

5.1 Introduction

Auxetic materials, also known as materials with negative Poisson's ratio (NPR), are characterized by their unusual response to uniaxial strain. As opposite to conventional materials, they demonstrate lateral shrinkage while being compressed. This endows auxetic materials with many desirable properties, such as enhanced mechanical resistance [177,178], variable permeability [179,180], high energy absorption ability [181], synclastic behavior [182]. Due to these remarkable properties, auxetic materials can be potentially used in various applications, including protective devices [183], smart sensors [184] and filters [179,185], angioplasty stents [186], fasteners [187] and textiles [188]. Among them, perforated systems [189–191] are of particular interest thanks to relative simplicity and low cost of manufacturing; for example, various periodic patterns, ranging from diamonds [192] to stars [193] or slits [149,194,195], have been explored to design auxetic material. Meanwhile, there have been increasing interest in using elastic instability induced pattern transformations to design reconfigurable metamaterials that exhibit negative Poisson's ratio behavior [46].

Bertoldi et al. [159] illustrated the NPR behavior in two-dimensional periodic porous structures with square arrays of circular voids in an elastomeric matrix. They found that the auxetic behavior arose from the dramatic changes in geometry due to the development of elastic instability. Overvelde et al. [45] considered the effect of pore shape on the mechanical response; Shim et al. [19] systematically investigated the role of circular hole arrangement on the post-buckling behavior of the periodic porous structures. Remarkably, these reversible pattern transformations have been demonstrated to be instrumental to design tunable color displays [160,196], phononic [20,68,69] and photonic [154] switches. The design of the periodic elastomeric porous structures is based on various distribution of voids in a single phase matrix material. Furthermore, mechanical properties [197] and surface patterns [157] in stiff-soft two phase composites can be controlled by tailored stiff phase distributions.

Here, we put forward a new design of soft auxetic *composites* incorporating *stiff* inclusions and voids periodically distributed in soft matrix. The rich design space of the material system provides the means to control the onset of instabilities and pattern formations through positioning of the stiff phase, while maintaining the ability to pre-design collapse of voids. This combination of voids, soft and stiff phases gives rise to new admissible multiple pattern switches, and tunable and enhanced NPR behavior. Guided by our numerical simulations, we experimentally realize the instability-induced pattern transformations and NPR behavior in 3D-printed multiphase soft auxetic composites. In addition, we illustrate a potential application of the reported pattern transformation phenomenon for design of acoustic soft metamaterials possessing tunable stop bands at low frequencies of elastic waves.

5.2 Experiments and simulations

The periodic composite specimens were fabricated by means of 3D printer Object Connex 260-3. The 3D printed samples were composed of stiff circular inclusions and voids periodically distributed in soft matrix as schematically shown in Figure 28. The radius of circular voids and stiff inclusions was $r_0 = 2$ mm, and the initial matrix volume fraction was $c^{(m)} = 0.3$. The stiff inclusions were printed in Verowhite resin, while the soft matrix was printed in digital material FLX9860, which is a mixture soft TangoBlackPlus (~ 85 wt%) and stiff Verowhite (~ 15 wt%) [198]. The out-of-plane thickness of both specimens was t = 10 mm. Uniaxial compression tests were performed using Shimadzu EZ-LX testing machine (maximum load 2 kN). During the test, the specimens were placed in a transparent fixture to prevent out-of-plane deformation. The specimens were quasi-statically compressed at constant strain-rate of $2\times10^{-4}\ s^{-1}$. Since the microstructure exhibits different mechanical responses in X- and Y-directions, two sets of experiments - compression in X-, and in Y- directions - were performed. The specimens that were loaded in X or Y material direction were composed of 8 × 11 or 10 × 9 unit cells, respectively. The deformation process was recorded by a high resolution digital camera.

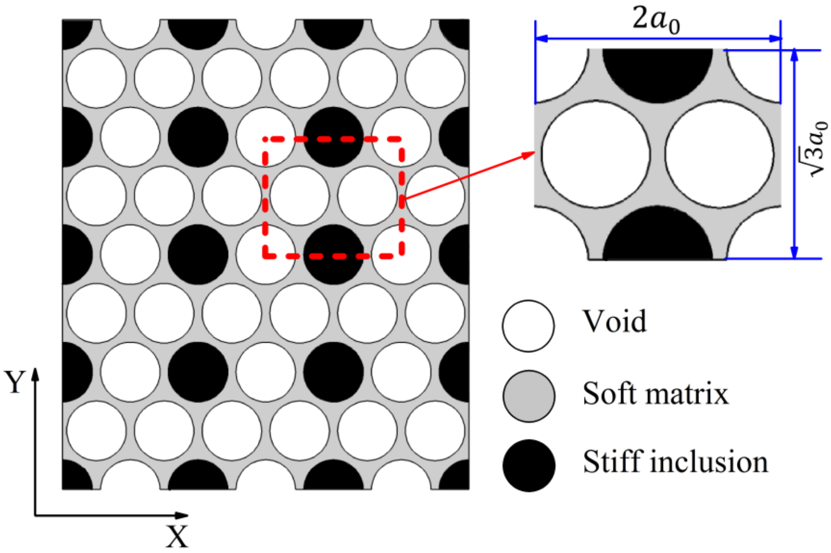

Figure 28. Schematic of the geometric arrangement of three phase (stiff inclusions, voids, soft matrix) periodic composites. a_0 denotes the center-to-center distance between circular voids in the undeformed configuration.

Numerical simulations are performed by means of the finite element code COMSOL 5.2a, in which the unit cell (see Figure 28) is constructed and corresponding periodic displacement boundary conditions are imposed on the opposite sides of the unit cell. Note that here we consider a 2D-system, in particular, plane-strain conditions are used; similar conditions are maintained in the experimental setting. The matrix and inclusion materials are modeled as neo-Hookean materials with initial shear moduli $\mu^{(m)} = 0.60$ MPa and $\mu^{(i)} = 0.63$ GPa, respectively. The onset of instability is identified by Bloch-Floquet analysis superimposed on the deformed state [68]; the analysis allows us to identify the critical strain and corresponding patterns that form upon achieving the critical level of deformation. This information is used in the post-buckling numerical analysis, for which new unit cells are constructed to match the new instability-induced periodicity. In particular, enlarged unit cell consisting of 1×2 primitive unit cells with small amplitude geometrical imperfections in the form of the buckling mode (obtained from Bloch-Floquet instability analysis) are numerically analyzed in the post-buckling regime.

5.3 Results and discussion

Figure 29 presents the evolution of the instability-induced pattern transformation when the composite is loaded in Y (a,b) or X (c,d) material directions at different strain levels from 0 to 20% (from left to right); rows (a, d) and (b, c) show the experimental and numerical results, respectively. We observe that when the critical compressive strain is reached, the material microstructure experiences rapid and dramatic changes, leading to the formation of the new patterns (see Figure 29(b, c) at $\varepsilon = 0.05$), which further evolve with an increase in applied strain. These observed changes in pattern transformation may be a result of a combination of the geometry changes and inhomogeneous deformation of the nonlinear materials. In particular, we note that the pattern transformation results in significant rotation of the stiff inclusion accompanied by the corresponding local deformation of the matrix. Similar deformation mechanism has been utilized in design of functional metamaterials [159,190,192,196,199]. Note that, in agreement with the numerical instability analysis predictions, the periodicity of the new pattern doubles in Y-direction (regardless of the compression direction). Although the development of the instability-induced patterns for the composite loaded in X- or Y-direction is initially similar (see Figure 29(a, d) at $\varepsilon = 0.05$), their patterns are essentially distinct at larger strain levels (for details, see the visualization of the deformed configurations in Appendix C). The difference in the achieved distinct microstructures is dictated by the positions of the stiff inclusions relative to the loading direction. Thus, various stiff inclusion distributions give rise to an increased variety of admissible instability-triggered patterns. We note that the initial shape of the material microstructure can be fully recovered after unloading, demonstrating that these pattern transformations are fully reversible. Remarkably, the structure exhibits negative Poisson's ratio (NPR) behavior upon developing the new instability-induced pattern; in particular, significant lateral contraction (in response to vertical contraction) are predicted numerically, and are observed experimentally (see Figure 29(b, c) at $\varepsilon = 0.2$) for both loading cases.

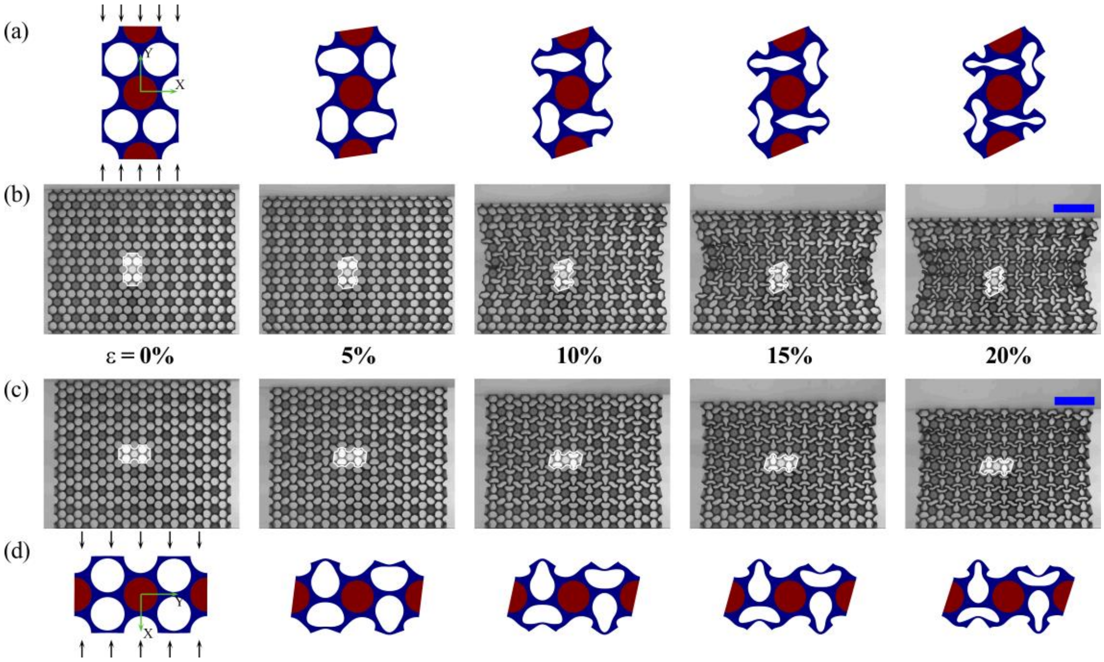

Figure 29. Numerical and experimental images of the structure loaded in Y-direction (a,b), in X-direction (c,d) at different macroscopic deformation levels. Scale bar: 20 mm.

Figure 30 shows evolutions of stress (a) and Poisson's ratio (c, d) as functions of the applied compressive strain for the composite structures loaded in X- and Y-material directions. Both experiments and simulations indicate that the stress-strain curves are strongly affected by elastic instabilities (see Figure 30(a)). In the stable regime, the stress-strain curves are almost linear, and the periodic composite exhibits different responses when loaded in X- and Y-direction. In particular, the effective moduli are 0.46 MPa (for X-material direction) and 0.64 MPa (for Y-direction). While the corresponding inclusion-matrix composite with hexagonal periodic unit cell exhibits similar in-plane responses for the corresponding X- and Y-loading directions [200]; the considered void-matrix-inclusion system possesses in-plane anisotropy as the microstructure differs in X- and Y- material directions. For completeness, we show the dependence of effective Young's moduli of the composite loaded in X- and Y-

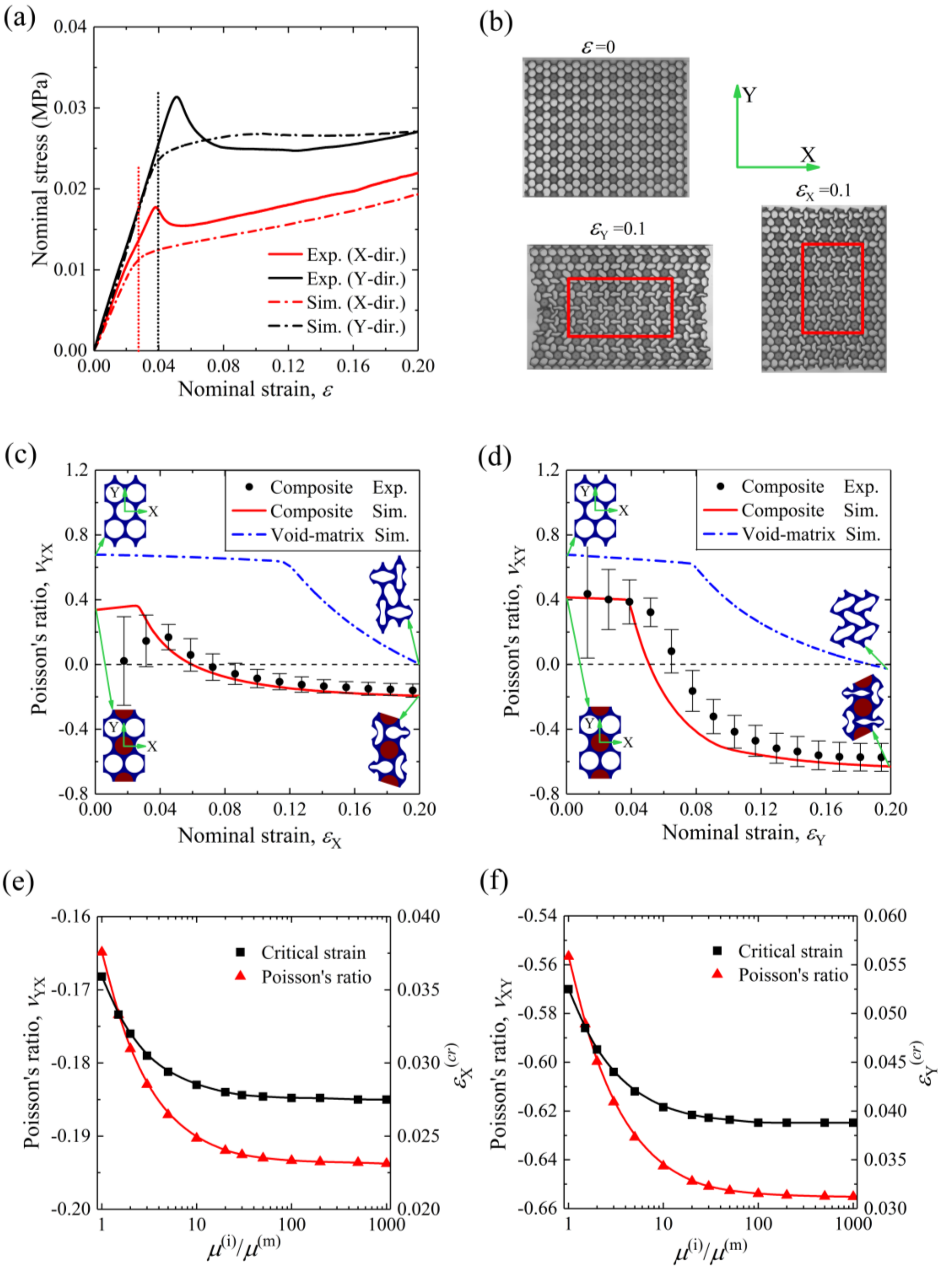

Figure 30. (a) Numerical and experimental stress-strain curves for the structure loaded in Y or X material directions. (b) Schematic composite area for Poisson's ratio evaluation. (c) Poisson's ratio ν_{YX} as function of ε_X. (d) Poisson's ratio ν_{XY} as function of ε_Y. (e-f) Dependence of critical strain and Poisson's ratio (at deformation level ε=0.2) on shear modulus contrast $\mu^{(i)}/\mu^{(m)}$.

material directions on matrix volume fraction in Appendix D. The critical strain levels are $\varepsilon_{\mathrm{X}}^{(cr)} \approx 0.028$ for the composite loaded in X material direction; and $\varepsilon_{\mathrm{Y}}^{(cr)} \approx 0.039$ for the composite loaded in Y material direction. The critical strain values are obtained numerically by the Bloch-Floquet analysis superimposed on the deformed state [68]. When the applied strain exceeds the critical level, significant softening of the structure is observed for both material loading directions. The numerical simulations predict earlier developments of instability patterns, as compared to the observed onset of instabilities in experiments. In addition, a drop in the stress level is observed (after the critical strain level) in experiments. This difference is due to the boundary effects of the tested samples; these effects are not included in the numerical simulations, in which infinite composites are examined through consideration of the periodic unit cell. Similar behaviors were also observed in buckling of porous structure [39,71]. In addition, the effect of friction between the fixtures and specimens may also contribute to the appearance of the local peak in the stress-strain curve.

Remarkably, the onset of instability and the associated composite microstructure switches significantly affect the effective Poisson's ratio (see Figure 30(c, d)). We observe that prior to instability, Poisson's ratio is positive in the composite loaded either in X- or Y- material directions[4]. When the critical deformation is reached, the voids suddenly collapse inward leading to a rapid decrease in composite Poisson's ratio, which soon becomes negative. Further increase in compressive deformation results in a slow decrease in the Poisson's ratio. The composite structure loaded in X or Y material directions exhibits a significant difference in the values of Poisson's ratio; for example, $\upsilon_{\mathrm{YX}} \approx -0.2$ or $\upsilon_{\mathrm{XY}} \approx -0.6$ at $\varepsilon = 0.2$, respectively. To highlight the significance of the stiff phase presence on the induced negative Poisson's ratio behavior, we present our numerical results for the corresponding void-matrix system (without stiff inclusions), whose buckled patterns have been experimentally observed by Shan et al. [6,19]. The dependence of the Poisson's ratio on deformation for the void-matrix system is denoted by dashed blue curves in Figure 30(c, d). We observe that the void-matrix system is characterized by positive Poisson's ratio and NPR behavior is not observed until the deformation reaches the level of $\varepsilon \approx 0.2$ (for both cases that loaded in X- or Y-directions). This is in contrast to the NPR behavior in the composites that start showing negative values of Poisson's ratio after only $\varepsilon \approx 0.05$. Thus, at larger strain levels the periodic composites show very significant NPR behavior as compared to the corresponding void-matrix system, for example, at $\varepsilon = 0.2$, the composite shows $\upsilon_{\mathrm{YX}} \approx -0.2$ or $\upsilon_{\mathrm{XY}} \approx -0.6$, while the void-matrix system has positive value for $\upsilon_{\mathrm{YX}} \approx 0.01$, and only $\upsilon_{\mathrm{XY}} \approx -0.03$. Furthermore, the stiff phase makes the composite prone to elastic instabilities at smaller strains; in particular the composite experiences instabilities at only $\varepsilon_{\mathrm{X}}^{(cr)} \approx 0.028$ or $\varepsilon_{\mathrm{Y}}^{(cr)} \approx 0.039$; while the void-matrix material requires $\varepsilon_{\mathrm{X}}^{(cr)} \approx 0.120$ or $\varepsilon_{\mathrm{Y}}^{(cr)} \approx 0.078$ to buckle. Thus, our results indicate that by introducing periodically distributed stiff phase into soft porous structures, new patterns can be induced upon instabilities; and these distinct patterns exhibit very different NPR behavior.

---

[4] In our experiments, Poisson's ratio was measured by monitoring the central part of the composite samples (where the behavior is not significantly affected by the boundary effects from the sample edges) by means of a high resolution digital camera allowing to identify the position of stiff inclusion centroids. The corresponding monitored central regions of the samples are highlighted by red rectangles in Figure 30(b). The details of the evaluation of the Poisson's ratio are described in the Appendix E.

Next, we show an example of the dependence of critical strain and Poisson's ratio on shear modulus contrast $\mu^{(i)}/\mu^{(m)}$ in Figure 30(e, f). The example of the Poisson's ratio dependence is given for the deformation level $\varepsilon = 0.2$. Through the simulations, we observe that the composites form the new periodicity with 1×2 primitive unit cells for the considered range of shear modulus contrasts, $\mu^{(i)}/\mu^{(m)}$ from 1 to 1000. The critical strain and Poisson's ratio decrease with an increase in shear modulus contrast for both X- or Y- loading directions. Thus, composites with higher shear modulus contrasts are more prone to instabilities and show more pronounced NPR behaviors.

Next, we explore a potential application of the reported reconfigurable material for tunable soft phononic crystal that can manipulate elastic wave propagation and filter specific frequency ranges, which, in turn, can be controlled by applied deformation. The Bloch wave analysis is performed at different deformation levels to obtain the corresponding dispersion curves [68]. The obtained dispersion relations (a, b) and the evolution of the stop bands for waves propagating in X- or Y-directions as functions of applied deformation (c-f) are shown in Figure 31. The reported frequency is normalized as $\tilde{f} = \omega a_0 / \left(2\pi\sqrt{\mu^{(m)}/\rho_0^{(\mathrm{m})}}\right)$, where ω is angular frequency and $\rho_0^{(\mathrm{m})}$ is the initial matrix density. We note that the initial density of the inclusions and matrix density is identical, namely, $\rho_0^{(\mathrm{i})} = \rho_0^{(\mathrm{m})}$.

In addition, a frequency domain analysis is performed to obtain the transmittance spectra, 16 enlarged unit cells with periodic boundary conditions are considered in the numerical model. Shear wave (S wave) and pressure wave (P wave) are excited to evaluate the corresponding attenuation, which is calculated as $\Phi = 20\log_{10}\left|\frac{u_{\mathrm{out}}}{u_{\mathrm{in}}}\right|$, where u_{in} and u_{out} refer to the average displacement for the input and output enlarged unit cell, respectively.

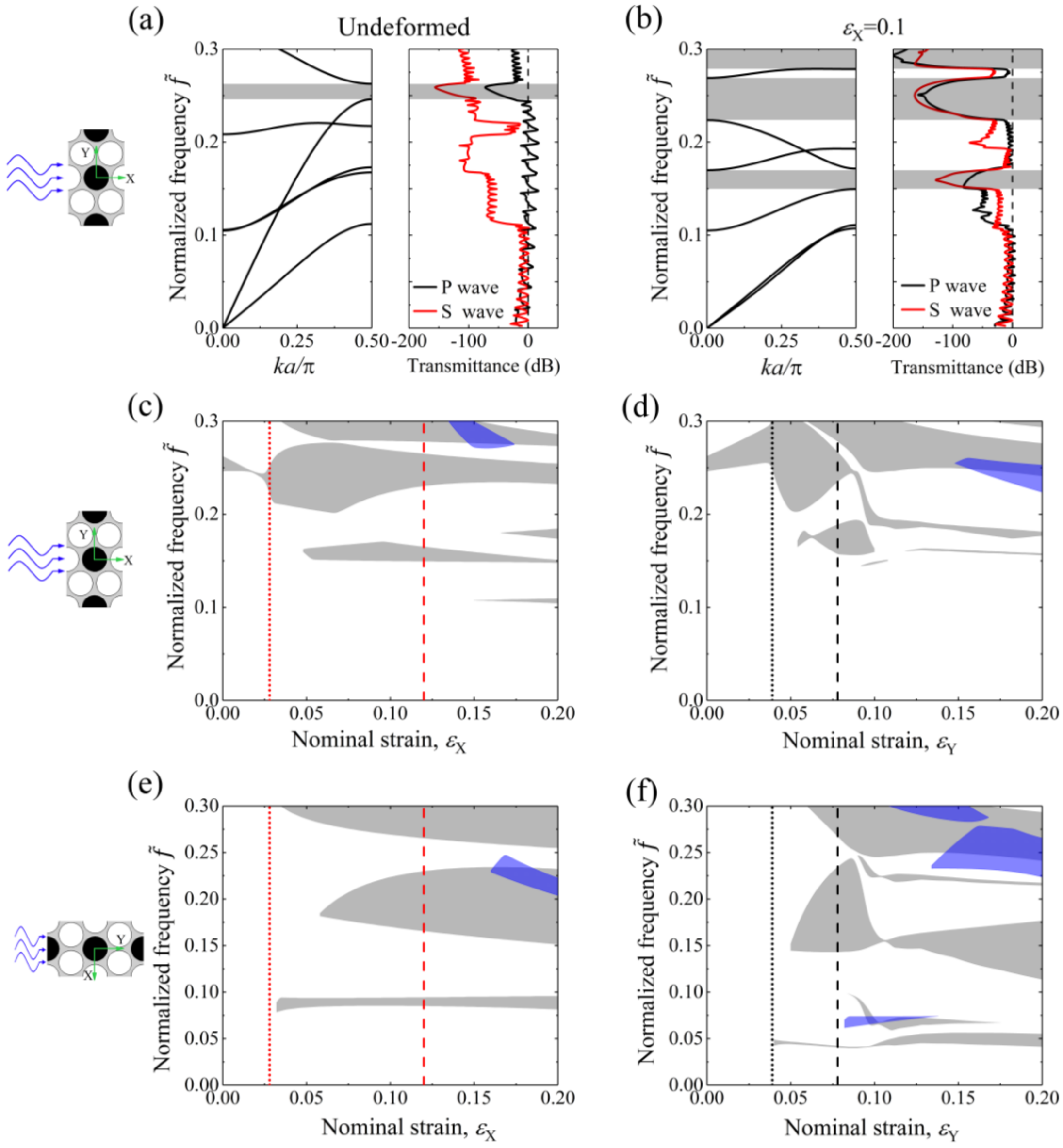

Figure 31. (a-b) Dispersion relations and transmittance spectrum for elastic waves propagating in X direction in undeformed (a) and deformed (b) states. (c-f) Evolution of stop bands for waves propagating in X (c, d) or Y (e, f) direction as a function of applied strain in X (c, e) or Y (d, f) direction. The shaded grey areas and blue areas correspond to the band gap structure of the void-inclusion-matrix composite and void-matrix system, respectively. The dotted curves and the dashed curves correspond to the critical strain of the composite and void-matrix system, respectively.

Figure 31(a, b) show the dispersion relations and corresponding transmittance spectrum in the undeformed and deformed ($\varepsilon_{\mathrm{x}} = 0.1$) states. Here, we show the results for elastic waves propagating in X direction at low frequency range $\tilde{f} \leq 0.3$. In the undeformed state, the periodic structure possesses the first band gap (i.e. the frequency ranges where neither pressure nor shear waves can propagate) at lower boundary $\tilde{f} = 0.246$ with the width $\Delta\tilde{f} = 0.016$. With applied strain $\varepsilon_{\mathrm{x}} = 0.1$, the band gap shifts the lower boundary towards $\tilde{f} = 0.224$, and widens up to $\Delta\tilde{f} = 0.045$. Moreover, in the deformed state, a new band gap – that does not exist in undeformed state – opens at a lower frequency range $\tilde{f} = 0.150 - 0.170$. Furthermore, the transmittance spectra shown in Figure 31(a, b) demonstrate significant attenuation at the corresponding bang gap frequency ranges for both shear and pressure waves.

Next, we show the evolution of the band gaps (denoted by shaded grey areas) for elastic wave propagating in X- or Y- directions as a function of applied strain in X or Y material directions in Figure 31(c-f). We observe that the widths and locations of the band gaps are significantly influenced by applied deformation, and new band gaps open upon reaching the instability point and pattern transformations. In the stable regime, for elastic wave propagating in X-direction, the prohibited frequency range is narrowed and shifted towards lower frequencies with an increase in strain applied in X-direction; while the applied strain in Y-direction expands the band gap width and shifts it towards higher frequencies. In the post-buckling regime, the width of the band gap increases significantly. Moreover, new band gaps are opened at low frequencies. For elastic waves propagating in Y-direction, there is no band gap in the undeformed state (in the considered frequency range $\tilde{f} \leq 0.3$). However, the instability induced new patterns give rise to formation of new band gaps. For example, at the applied strain $\varepsilon = 0.2$, the structure loaded in X-direction possesses two band gaps at $\tilde{f} = 0.081 - 0.096$ and $0.151 - 0.232$ frequency ranges, whereas the structure loaded in Y-direction possesses five band gaps at $\tilde{f} = 0.048 - 0.062;\ 0.074 - 0.076$; $0.139 - 0.178;\ 0.223 - 0.224$; and $0.249 - 0.292$. These results indicate that the reported instability-induced pattern transformations in multiphase composites hold significant potential for applications as switchable acoustic metamaterials.

For comparison, we present the evolution of the band gaps (denoted by shaded blue areas) in void-matrix system (corresponding to the considered composite with the stiff inclusions replaced by voids) in Figure 31(c-f). The corresponding matrix volume fraction is identical to that of void-matrix-inclusion system, namely, $c^{(m)}$ =0.3. In the void-matrix system, the instability induced pattern also opens the band gaps; however, the widths of band gaps are significantly narrowed, and their locations are at higher frequency ranges as compared to the composite (compare the shaded blue and grey areas in Figure 31(c-f)). In addition, we provide an example with the following material parameters: matrix volume fraction $c^{(m)}$ =0.3, a_0 =10 mm, $\mu^{(m)} = 0.6$ MPa, $\rho_0^{(\mathrm{m})}$ =10^3 kg/m^3; and, for the composite with stiff inclusions, we consider $\mu^{(i)} = 630$ MPa and $\rho_0^{(\mathrm{i})} = \rho_0^{(\mathrm{m})}$. When elastic waves propagate in the undeformed composite in Y direction, there is no band gap in the frequency range 0-600 Hz for both composites. However, at applied deformation level of $\varepsilon_{\mathrm{x}} = 0.2$, the void-matrix material opens a band gap at frequency range 499.2−545.0 Hz, whereas the composite with stiff inclusions exhibits more remarkable band gaps at lower frequency ranges, namely, at 198.7−234.1 Hz and 370.1−568.8 Hz. This is remarkable because it is usually challenging to open band gaps at low frequency ranges.

We note that many soft materials are rate dependent, and this aspect is not included in the simulations. Therefore, the numerical predictions of the band gap are more applicable for composites made out of phases with low damping; otherwise, these effects may shift the edges of band gaps and affect the corresponding attenuations [201,202]. We note that the computational predictions of the band gaps in the soft single phase porous system have been experimentally demonstrated through the observed capability of significant wave attenuation in the frequency ranges controlled by deformation [6]. In addition, the examined composite exhibits significant NPR behavior and opens low frequency band gaps after the deformation exceeds the critical level; although effective Poisson's ratio would manifest in a lower initial slope (corresponding to long waves) of the longitudinal or pressure wave branch in dispersion curves, the observed effective NPR may not be directly related to the formation of the band gaps.

Moreover, we note that the performance of the system can be potentially optimized through a selective choice of distribution, volume fractions, and shapes of stiff inclusion and voids, to give rise to a specific property, such as enhanced NPR behavior; the effect of material properties, such as shear modulus and density contrasts, viscoelasticity, on the material performance and wave propagation properties can be also considered in the future work.

5.4 Summary

To summarize, through a combination of numerical calculations and experiments on 3D printed composite samples, we demonstrate the existence of multiple stable patterns in the identical composite material with periodically arranged phases. These new instability induced patterns – tunable by the location of the stiff phases – give rise to the negative Poisson's ratio behavior. Thus, one can potentially pre-design and significantly tune the onset of instability and the associated microstructure transformations. Thus, we achieve highly tunable and switchable properties and functionalities, such as negative Poisson's ratio, and acoustic properties of the soft composite materials. We illustrate that the reported phenomenon of reversible pattern transformations in composite materials can be utilized for the design of highly tunable phononic crystals. The reported multiphase composite material system opens new ways for design of reconfigurable material and devices, including acoustic switches [4,6], actuators [21,143,144,203,204], soft robotics [2,205], and flexible electronics [7,153,206].

Chapter 6

Tunable microstructure transformations and auxetic behavior in multiphase composites: the role of inclusion distribution[*]

We experimentally and numerically investigate instability-induced pattern transformations and switchable auxetic behavior in multiphase composites consisted of circular voids and stiff inclusions periodically distributed in a soft elastomer. We specifically focus on the role of inclusion distribution on composite behaviors. We show that tailored positioning of the stiff inclusions can be exploited to expand the set of admissible switchable patterns in multiphase composites. Thus, extreme values of negative Poisson's ratio can be attained through applied strains; moreover, the onset of instabilities, and the corresponding switches to extremely soft behavior are shown to be controlled by the inclusion arrangements and volume fractions. Furthermore, the dependence of the microstructure buckling and post-buckling behavior on loading direction is investigated, and the composite anisotropic properties depending on the microstructure parameters are discussed.

---

[*] Based on the published paper: Li J, Rudykh S. Tunable microstructure transformations and auxetic behavior in 3D-printed multiphase composites: The role of inclusion distribution. Compos Part B Eng 2019;172:352–62.

6.1 Introduction

Owing to enhanced mechanical properties and functionalities, microstructured materials – such as, fiber-reinforced or cellular microstructures – have become attractive for various engineering applications [4,140,207–210]. The properties tailored through microstructure geometry can be further tuned by external stimuli, or, in case of deformable materials, by pre-stress. In the latter case, the large deformations lead to the evolution in composite microstructures accompanied by geometrical and materials nonlinearities [141,176,197]. Moreover, the materials may exhibit sudden changes in their microstructures due to elastic instabilities. The phenomenon holds significant potential for designing new materials with switchable properties and functionalities [18,94,157,211]. To predict the onset of instabilities and associated buckling modes various techniques have been developed and employed [24,122,127]; in the context of nonlinear elasticity theory, the framework of small deformation superimposed on the finitely deformed state is used [70]. Within the framework, the onset of macroscopic or long wave instabilities can be predicted through the loss of ellipticity analysis based on the homogenized response of the material [13,29–31,103,104]; while microscopic instabilities can be detected through the Bloch-Floquet analysis [11,12,25,37,68,107], which also allows detecting the long wave instabilities for a special limit. In this work, we employ the Bloch-Floquet technique to investigate the instability phenomenon and, then, post-buckling behavior in soft composite with various periodic distributions of voids and stiff inclusions – these structures can exhibit cooperative and controllable collapse of the voids leading to sudden pattern transformations, which hold the potential for responsive and reconfigurable functional materials and devices, such as highly stretchable metamaterials [149], switchable auxetic materials [194], and elastic wave filters [6,14,20,68,69], color displayers [160], and actuators [21].

Abeyaratne and Triantafyllidis [38] studied the onset of instability in porous solids detecting the loss of ellipticity in homogenized periodic porous elastomer under large strains. Triantafyllidis and Maker [23] examined layered composite with incompressible hyperelastic phases, and showed the connection between the microscopic instability analysis and loss of ellipticity. Geymonat et al. [26] established the rigorous theoretical foundation for Bloch-Floquet technique to detect microscopic and macroscopic instabilities in finitely strained periodic composites; it was shown that the long wave instability limit can be identified with the loss of ellipticity of the homogenized properties. Based on these results, Triantafyllidis et al. [40] numerically investigated the microscopic and macroscopic instabilities in porous structure with periodic distribution of circular voids. Michel et al. [212] predicted microscopic instabilities in porous system with periodic distribution of circular voids in a square unit cell. The development of the corresponding instability-induced pattern transformations was experimentally observed in an elastomeric system with a square array of circular voids by Mullin et al. [39]. The buckling mode at micrometer length scale was also realized in polymer structures with periodically distributed circular voids fabricated by interference lithography [41–43]. Later, Bertoldi et al. [159] investigated the instability-induced negative Poisson’s ratio behavior in the 2D porous systems, and this idea was extended to the design of 3D soft metamaterials with auxetic behavior [46]. In addition, the distribution [19,71] and shape [44,45] of voids were further employed to obtain complex new patterns and to tune Poisson's ratio. Shan et al. [6] employed the anisotropic property of composite structure to trigger multiple pattern transformations in an elastomeric porous structure comprising of a triangular periodic arrangement of circular voids. Florijn et al. [48,49] proposed a bi-void system comprising of larger and smaller circular voids to induce co-existing states and switches between these. Overvelde et al. [50] realized the instability-induced checkerboard pattern in soft metamaterial comprising a square array of circular voids under equibiaxial tensile load. Recently, Li et al. [14] introduced the design of switchable soft system comprising of arrays of circular voids and stiff inclusions distributed in a soft matrix. These materials showed new pattern transformations with a strong auxetic behavior.

In this study, we examine the role of the stiff inclusions, their positions and volume fraction, on the instabilities and post-buckling behaviors in the transformative composites; and explore the ways of using this composite design space for tailored performance and enriched instability-induced pattern transformations. Moreover, we examine the multiphase composite anisotropy, and study the response of the composites subjected to different loading directions. First, we discuss possible arrangements of circular stiff inclusions in the structure with periodically distributed circular voids, where new uniform buckling modes are observed. Then, guided by the numerical simulations, we experimentally realize and observe multiple pattern transformations depending on the distribution of inclusions and loading directions in the samples fabricated by multimaterial 3D printing. Next, simulations of infinite periodic and finite size structures are compared with the experimental results of 3D printed samples. Finally, the effect of the distribution of stiff inclusions, loading direction, phase volume fraction, and inclusion-to-matrix ratio of shear moduli on the responses of the composites is numerically studied to illustrate the tunability of the systems.

6.2 Specimen design and fabrication, and experimental testing

First, we discuss possible arrangements of circular stiff inclusions in the structure with periodically distributed circular voids. In the periodic void system a cooperative (or uniform) collapse of the voids happens when the ligaments undergo the same buckling mode simultaneously [19,47]. To achieve this behavior, the geometrical requirements for the void position are: (i) the distance between neighboring voids is identical; (ii) the number of ligaments around each void is an even number. Based on that, we consider two types of distributions of stiff inclusions in the porous structure with circular voids arranged in triangular configuration, while the stiff inclusions are arranged in square (a) and triangular (b) configurations as shown in Figure 32, which are denoted as *composite type A* and *composite type B*, respectively. The corresponding primitive unit cells are highlighted by light green color.

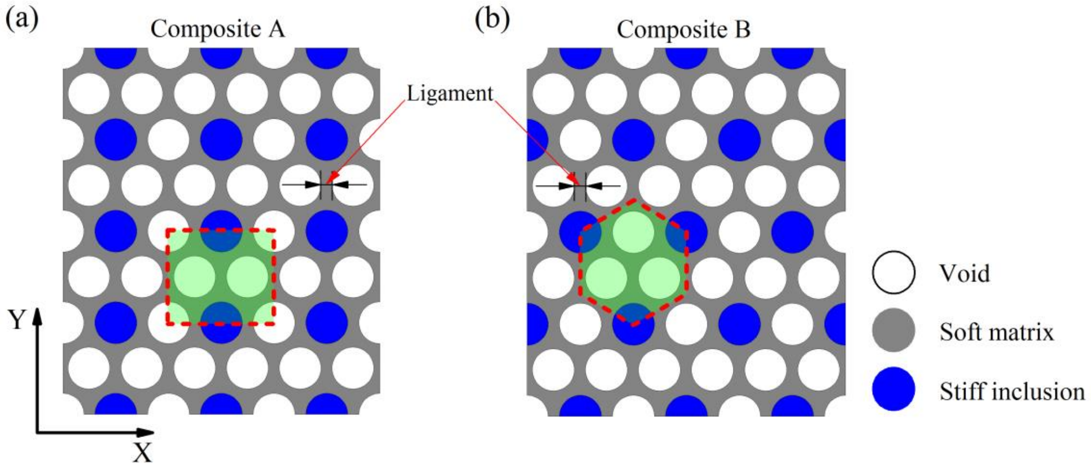

Figure 32. Schematics of periodic microstructures with circular stiff inclusions arranged in square (a) and triangular (b) configurations.

To investigate the effect of inclusion distribution on the mechanical responses of the proposed anisotropic multiphase composites under different loading directions, the specimens with circular voids and stiff inclusions periodically embedded in an elastomeric soft matrix were fabricated by using a multimaterial 3D printer (Object Connex 260-3). The soft matrix was printed in FLX9860 digital material with initial shear modulus $\mu^{(\mathrm{m})} = 0.6$ MPa, the stiff inclusion was printed in VeroWhite resin with initial shear modulus $\mu^{(\mathrm{i})} = 600$ MPa. The specimens were characterized with initial volume fraction of soft matrix $c^{(m)} = 0.25$, as well as identical void and inclusion radii $r = 3$ mm. For all specimens, the in-plane dimensions were 92.37 × 91.42 mm (width × height), the out-of-plane dimension was $t = 10$ mm (thickness). In order to track the positions of stiff inclusions during the deformation process, the centroids of stiff inclusions were marked by black dots.

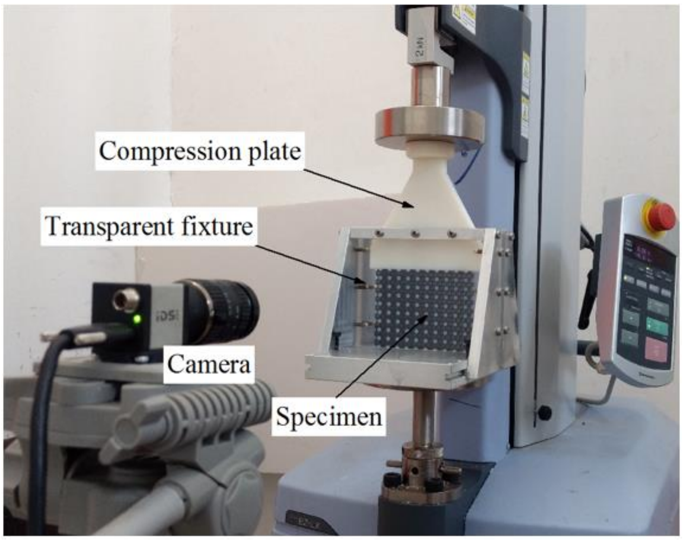

Figure 33. Experimental setup.

Uniaxial compression tests under plane strain conditions were conducted using the Shimadzu EZ-LX testing machine with maximum load 2 kN. The corresponding experimental setup is shown in Figure 33. The specimen was held between two transparent parallel fixtures mounted on a metal base to maintain the plane-strain conditions. A plate printed in VeroWhite material and thickness $t = 10$ mm was placed between the specimen and the testing machine to apply load on the specimen. The compression tests were performed at a constant strain rate of $4 \times 10^{-4}\ \mathrm{s}^{-1}$. Compression displacement and applied force were recorded to produce stress-strain curves. A high-resolution digital camera was placed in front of the specimen to monitor the deformation process capturing one frame at 0.01 mm compression displacement.

6.3 Simulations

To analyze the mechanical responses for the multiphase composites, numerical simulations are performed for both finite size structure and infinitely periodic structure.

The responses of soft matrix and stiff inclusion materials are modeled as neo-Hookean hyperelastic materials, whose strain energy density function is defined as

$$W = \frac{\mu}{2}(I_1 - 3) - \mu \ln J + \frac{\Lambda}{2}(\ln J)^2, \tag{26}$$

where μ and Λ denote the initial shear modulus and the first Lame constant, respectively. $I_1 = \mathrm{tr}(\mathbf{F}^{\mathrm{T}}\mathbf{F})$ and $J = \det(\mathbf{F})$, with $\mathbf{F}$ denoting the deformation gradient. The high ratio $\Lambda/\mu = 1000$ is used to maintain the nearly incompressible behavior of the material; for the soft matrix material the initial shear modulus is $\mu^{(\mathrm{m})} = 0.6$ MPa. The inclusion-to-matrix ratio of shear moduli is chosen as $\mu^{(\mathrm{i})}/\mu^{(\mathrm{m})} = 10^3$ so that the stiff inclusions almost do not deform.

To identify the onset of instability in infinite periodic composite under large deformations, Bloch-Floquet analysis superimposed on the deformed state is used [11,20,23,26,37,68]. The analysis is implemented in the nonlinear finite element code COMSOL 5.2a. To obtain the solution for the deformed state, we first apply the averaged macroscopic deformation through imposing periodic displacement boundary conditions on the edges of the primitive unit cell via $\mathbf{u}_B - \mathbf{u}_A = (\bar{\mathbf{F}} - \mathbf{1})(\mathbf{X}_B - \mathbf{X}_A)$, where $\mathbf{X}$ denotes the position vector in the undeformed configuration; $\mathbf{u}$ denotes the displacement vector; $\bar{\mathbf{F}}$ is the applied macroscopic deformation gradient; A and B are the paired nodes periodically located at the opposite edges of the primitive unit cell. Then, Bloch-Floquet conditions are superimposed on the edges of the deformed primitive unit cell via $\mathbf{u}(\mathbf{X} + \mathbf{R}) = \mathbf{u}(\mathbf{X})e^{-i\mathbf{K}\cdot\mathbf{R}}$, where $\mathbf{R}$ defines the distance between the paired nodes on the opposite edges of the unit cell; $\mathbf{K}$ is the wave vector. Through gradually increasing the applied deformation along the loading path and solving the corresponding eigenvalue problem, the microscopic instability is identified, when the lowest eigenvalue (of a non-trivial eigenmode) attains zero. The corresponding applied strain level and wavenumber are identified as the critical strain $\varepsilon^{\mathrm{cr}}$ and critical wavenumber $\mathbf{K}^{\mathrm{cr}}$. Note that macroscopic instability is detected when $\mathbf{K}^{\mathrm{cr}} \rightarrow \mathbf{0}$; this long wave instabilities can be identified through examining the loss of ellipticity analysis, and the corresponding conditions for the effective acoustic tensor or tensor of the elastic moduli [23,26]. Once the critical conditions are identified, the postbuckling analysis is performed. To this end, an updated unit cell is constructed – defined through the obtained critical wavenumber $\mathbf{K}^{\mathrm{cr}}$. To trigger the instability induced pattern transformations, small amplitude imperfections in the form of the buckling mode (obtained from Bloch-Floquet instability analysis) are introduced in the initial geometry of the updated unit cell.

Quadratic triangular plane strain elements are used in simulations for periodic structures and finite size structures; a mesh sensitive analysis has been performed, in accordance to the analysis, mesh density of approximately 4000 elements for each primitive unit cell has been used.

In addition, numerical simulations on finite size specimens are conducted using explicit nonlinear finite element code LS-DYNA. The mesh of finite size structure is disturbed by introducing a small amplitude imperfection in the form of the first buckling mode obtained by linear buckling analysis. In the analysis, the displacement of the top and bottom edges of the structure was constrained to be horizontally fixed. The contact between the edges for the collapsed voids is modeled using the CONTACT_AUTOMATIC_SINGLE_SURFACE option. The quasi-static loading conditions are maintained while monitoring the force response and deformation mode being independent of the loading rate.

6.4 Results and discussion

We start with studying of the deformation processes of the two types of the periodic composites A (as shown in Figure 32(a)) and B (as shown in Figure 32(b)) with a fixed volume fraction of the phases; next, we will examine the effect of the constituent volume fractions on the performance of the multiphase composites. Since the materials exhibit anisotropic behavior, we show their responses for different loading directions; in particular, each of the composite is tested under uniaxial compression in X- and Y-material directions.

Figure 34 shows the experimental and numerical results on deformation sequences for the composites at different deformation levels (the numerical results for infinite periodic and finite size specimens are given at the first and third rows, respectively; the experimental results are given at the second row). When the critical strain is reached, the voids collapse as the ligaments between them buckle. This leads to sudden microstructure transformations along with the breakage of composite symmetry and/or periodicity (see Figure 34(a-d) at $\varepsilon = 0.10$). As the deformation level is further increased, the instability-induced new patterns are rapidly accentuated (see Figure 34(a-d) at $\varepsilon = 0.15$) and start evolving. Remarkably, the significant lateral contraction with respect to the loading direction is observed both experimentally and numerically for all cases (see Figure 34(a-d) at $\varepsilon = 0.20$). This instability-induced negative Poisson's ratio or auxetic behavior is attributed to the microstructure transformation in the postbuckling regime. We note that the numerical simulations of the finite size samples nicely capture the boundary effects relevant to the experimental testing; due to the boundary effects only the central part of the specimens exhibit a nearly uniform deformation of the unit cells corresponding to the numerically modeled infinite periodic structures.

Moreover, both experiments and simulations show that the buckled patterns for *composite A* (with the square periodicity of inclusion distribution) loaded either in X- or Y-material directions consist of 1 × 2 primitive unit cell; while *composite B* (with the triangular periodicity of inclusion distribution) preserves its initial periodicity even after the onset of instability for both loading directions. Moreover, thanks to the anisotropy of the composite microstructures, the development of the buckling patterns can be tuned by altering the loading direction. For example, different pattern developments are observed for *composite A* loaded in X- and Y-material directions; as a result, different effective behaviors can be observed for these loading cases, in particular, *composite A* loaded in Y-material direction exhibits a more significant lateral contraction behavior. Thus, this illustrates that rich pattern transformations can be obtained through tuning the positions of stiff inclusions and loading directions. Finally, the initial microstructure of the composites is fully recovered after the release of applied loading, demonstrating that these instability-induced pattern transformations are fully reversible.

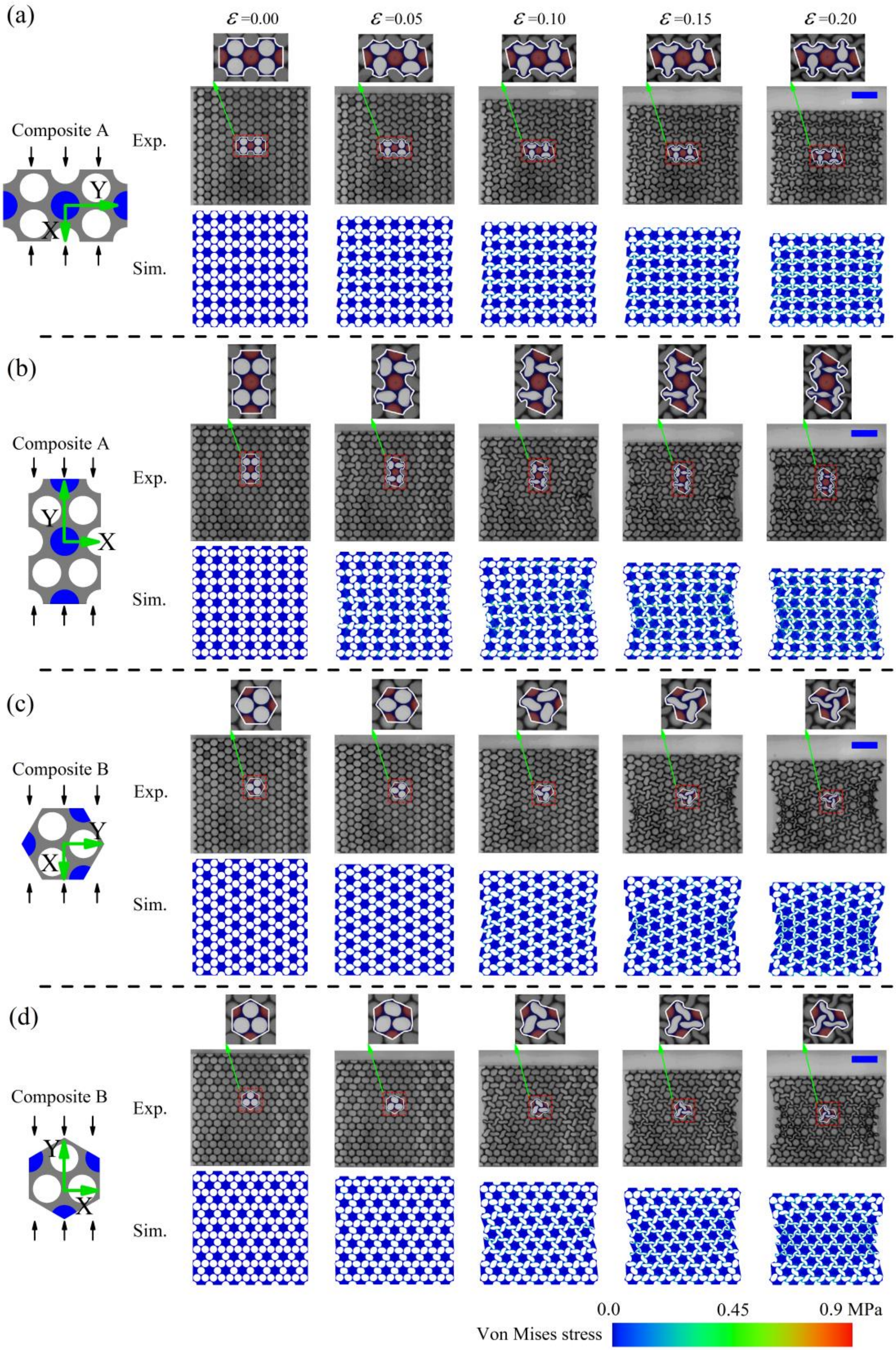

Figure 34. Deformation sequences in soft composites at different deformation levels. Scale bar: 20 mm.

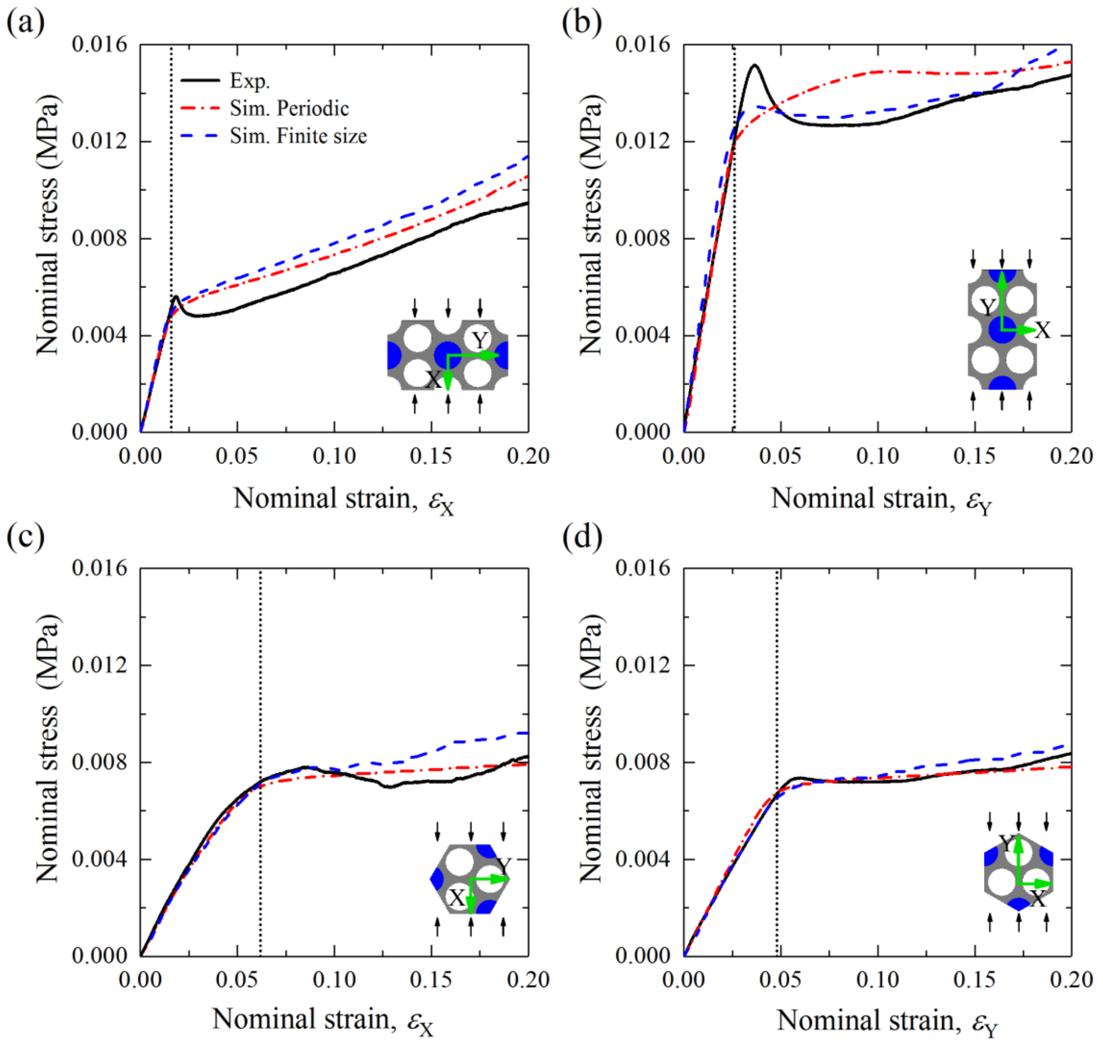

Figure 35. Experimental and numerical stress-strain curves. Dotted lines denote critical strains for infinite periodic composites.

Figure 35 shows the experimental and numerical results of the evolution of nominal stress as functions of applied strain. The dotted vertical lines refer to the critical strains of the corresponding infinite periodic composites. We observe that the buckling strain is significantly influenced by the positions of stiff inclusions and loading directions. The critical strains for *composite A* loaded in X- and Y-material directions are $\varepsilon_{cr} = 0.016$ and 0.026, respectively; while the critical strains for *composite B* loaded in X- and Y-material directions are $\varepsilon_{cr} = 0.062$ and 0.048, respectively. Prior to the onset of instability, the stress-strain relation is characterized by an initial nearly linear behavior of the curves; in this stable regime, *composite A* has a larger effective modulus as compared to the response of *composite B*, regardless of the loading direction. We note the agreement between the stress-strain curves observed in experiments and predicted by the finite element modeling for both finite size and infinite periodic structures. This is due to the fact that in the stable regime, each primitive unit cell undergoes a nearly identical deformation, which has been observed experimentally (see, for example, Figure 34(c, d) at $\varepsilon = 0.05$). However, upon achieving the critical strain, softening behavior is observed in all cases due to the development of elastic instability. We observe that *composites A* exhibits almost linear stress-strain curve behavior after buckling (for both loading directions); while for *composite B*, a plateau stress is observed following the onset of instabilities; this continues until the development of new patterns results in partial closure of the voids resulting in the increased overall stiffness. We note that a drop in the stress value is observed in the experiment after the applied deformation exceeds a critical level; this is more visible for *composite A* loaded in X-and Y-material directions; this phenomenon, however, is not captured by simulations. Similar differences between simulations and experiments were also reported in the system of periodic elastomeric array of circular voids [39]. There is a number of factors – stemming from the numerical model simplifications – that may contribute to the observed differences. These include the constitutive material model with the absence of inelastic behavior, strong plane strain constraint, absence of friction, and possible dynamic effects not accounted for in the numerical simulations.

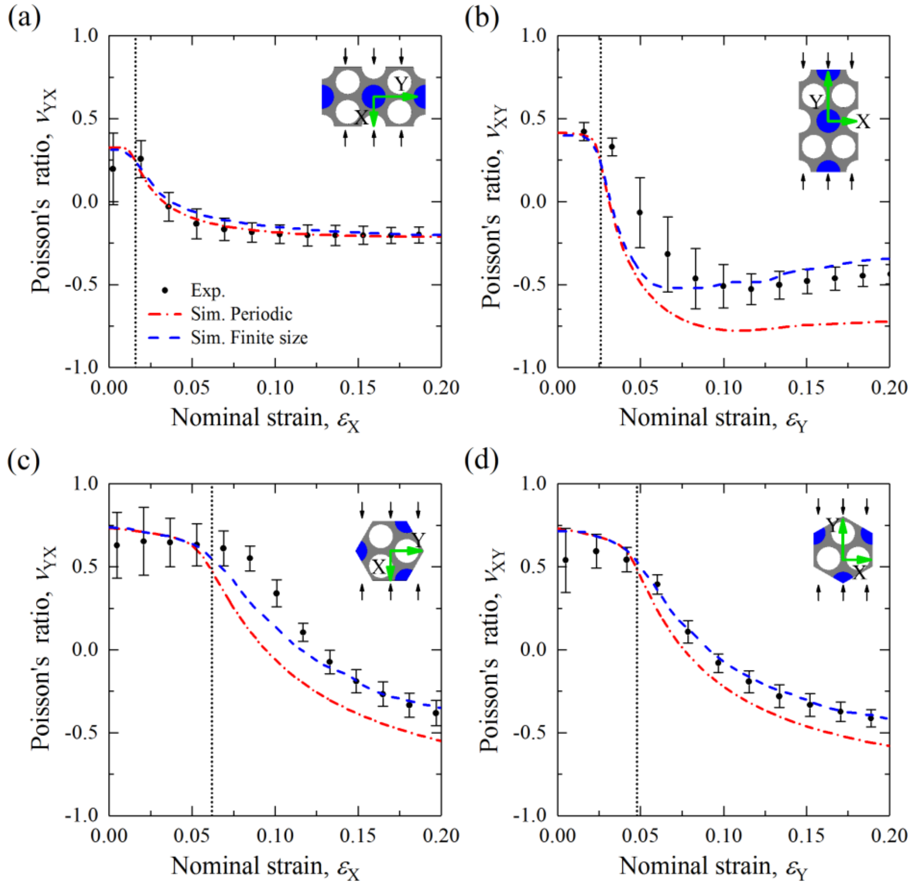

Figure 36. Effective Poisson's ratio vs strain level.

Figure 36 shows the dependence of the effective Poisson's ratio on the applied strain. The blue dashed and red dash-dotted curves correspond to the numerical results for finite size and infinite periodic structures, respectively; while the experimental results are denoted by the black points with error bar[5] symbols (the details about the calculation of the effective Poisson's ratio is given in Appendix F). We observe a good agreement between the trends of the curves for numerical results and experimental observations; however, some quantitative differences are observed, especially in the initial regime of relatively small deformations. In this regime, the displacement of stiff inclusion is relatively small, and the measurement inaccuracy influences the calculated value of the effective Poisson's ratio. After the applied deformation exceeds the critical strain, due to the buckling of the ligaments resulting in void collapse, a rapid drop in Poisson's ratio up to a negative regime is observed in both experiments and simulations for all cases. The drop in Poisson's ratio is followed by a slow decrease with a further increase in the applied deformation. While for *composite A* loaded in X-material direction excellent agreement between experiments and simulations is observed, for other cases, the simulations on finite size structures show a better agreement with experiments in comparison to the results from the simulations of the infinite periodic structures. This is due to the fact that the finite size specimen (of *composite A* loaded in X-material direction) exhibits nearly identical deformation of the unit cells up to $\varepsilon = 0.2$ (see Figure 34(a)). For other cases (*Composite A* loaded in Y-material direction, and *composite B* loaded in X- and Y-material directions), the lateral edges of the specimens significantly bend inward due to the strong negative Poisson's ratio behavior (see Figure 34(b-d) at $\varepsilon = 0.2$); this effect is not accounted for in the infinite periodic structure simulations. Finally, we note the significant dependence of the instability-induced negative Poisson's ratio behavior on the positions of stiff inclusions and loading directions. For example, at applied strain $\varepsilon = 0.2$, effective Poisson's ratios for infinite periodic *composite A* loaded in X- and Y-material directions are $\nu_{\mathrm{YX}} = -0.21$ and $\nu_{\mathrm{XY}} = -0.72$, respectively; while the Poisson's ratios for infinite periodic *composite B* loaded in X- and Y-material directions are $\nu_{\mathrm{YX}} = -0.55$ and $\nu_{\mathrm{XY}} = -0.58$, respectively.

---

[5] The error bars represent the standard deviations of the calculated effective Poisson's ratio values based on various selected representative elements; the calculation procedure is described in the Appendix F.

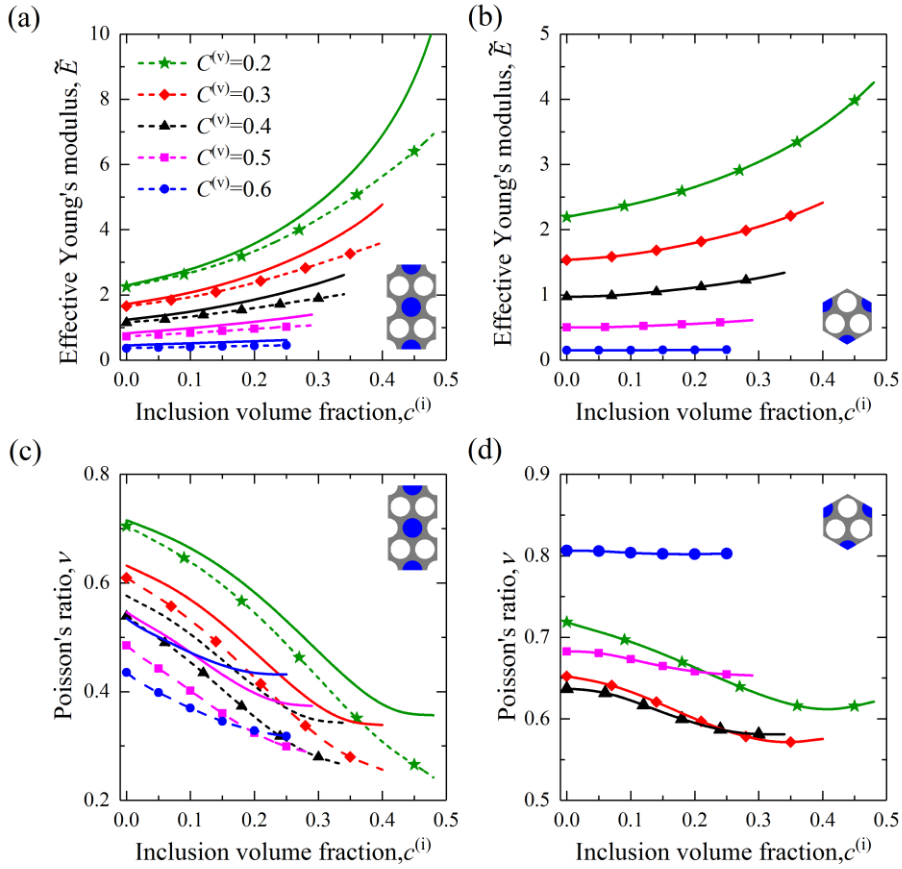

Figure 37. Dependence of effective Young's modulus and Poisson's ratio on inclusion volume fraction for composites with various void volume fractions in the stable regime of small deformations. The dashed curves with markers and the continuous curves refer to the results of the composite loaded in X- and Y-material directions, respectively.

For completeness, we show the effect of the inclusion distribution and loading direction on the initial responses (in the stable regime of small deformations) of the periodic composites. Figure 37 presents the dependence of effective Young's modulus and Poisson's ratio on inclusion volume fraction for the composites with various void volume fractions. The dashed curves with markers and the continuous curves refer to the results of the composite loaded in X- and Y-material directions, respectively. The effective Young's modulus is calculated as $E^{\text{eff}} = 2U\varepsilon^{-2}/A$, where U is the stored elastic energy; A is the area of the primitive unit cell; ε is the applied strain. The method has been verified against the analytical estimation for inclusion-reinforced composite with stiff inclusions periodically embedded in a softer matrix arranged in a hexagonal array [200]. The effective Young's modulus is normalized as $\tilde{E} = E^{\mathrm{eff}}/\mu^{(\mathrm{m})}$. We observe that the effective Young's modulus and Poisson's ratio for *composite A* loaded in X- and Y-material directions are clearly different (see Figure 37(a, c)); whereas the corresponding responses for *composite B* loaded in X- and Y-material directions are identical (see Figure 37(b, d)). *Composite A* shows a stiffer response when loaded in Y-material as compared to its response to loading in X-direction. For both cases, an increase in inclusion volume fraction leads to an increase in effective Young's modulus, and this effect is more significant for the composite with smaller void volume fraction. For example, an increase in stiff volume fraction of *composite B* from $c^{(\mathrm{i})}$ =0.05 to 0.25 results in an increase in effective Young's modulus from $\tilde{E}$ =0.148 to 0.160 for the case $c^{(\mathrm{v})} = 0.6$, from $\tilde{E} = 2.288$ to 2.832 for the case $c^{(\mathrm{v})} = 0.2$. Larger Poisson's ratios are observed for *composite A* loaded in Y-material direction in comparison to the load in X-material direction; and composites with higher inclusion volume fractions exhibit lower Poisson's ratios (see Figure 37(c)). The effect of inclusion volume fraction on Poisson's ratio in *composite B* is very different, and it strongly depends on the composite void volume fraction (see Figure 37(d)). For instance, the influence of inclusion volume fraction on Poisson's ratio for *composite B* with $c^{(\mathrm{v})} = 0.6$ is negligible; whereas an increase in inclusion volume fraction results in a significant decrease in Poisson's ratio for *composite B* with $c^{(\mathrm{v})} = 0.3$.

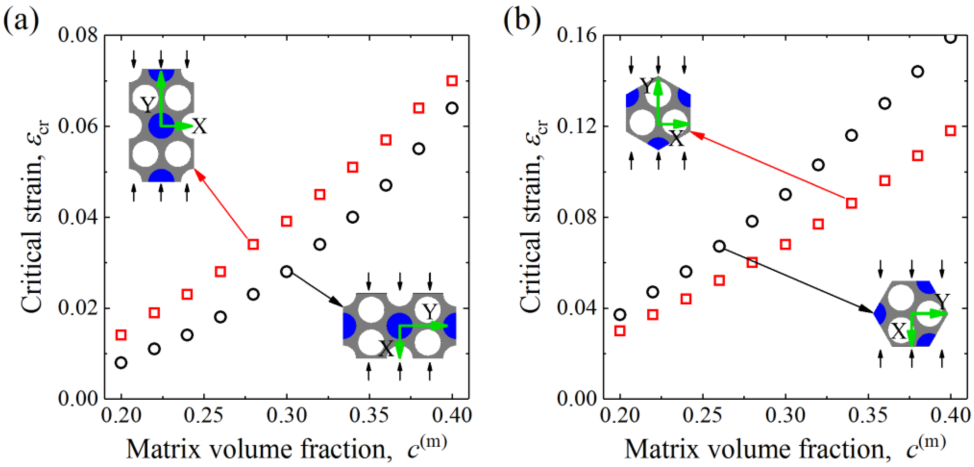

Figure 38. Dependence of critical strain on matrix volume fraction. The radii of circular voids and stiff inclusions are identical.

Next, we examine the influence of the phase volume fractions on the onset of instabilities. To this end, we perform the Bloch-Floquet analysis (described in the Numerical Modeling Section). Figure 38 shows the dependence of critical strain on the composite matrix volume fraction. Here, the radii of the circular voids and stiff inclusions are set to be identical. Note that in the considered range $c^{(v)} \in (0.2, 0.4)$, all composites experience microscopic instabilities, and the buckling mode of *composite A* consists of 1×2 primitive unit cell, while *composite B* preserves its initial 1×1 periodicity (see Figure 32). Regardless of the positions of the stiff inclusions and loading directions, we observe that a decrease in matrix volume fraction results in an earlier onset of instability. This is because the composites with lower matrix volume fractions have slender ligaments that are prone to buckling. We observe that *composite A* loaded in X-direction buckles earlier as compared to the response in Y-direction; whereas *composite B* is more stable when the applied load is in X-material direction. Moreover, we note that *composite A* is more prone to buckling than *composite B* for both loading directions.

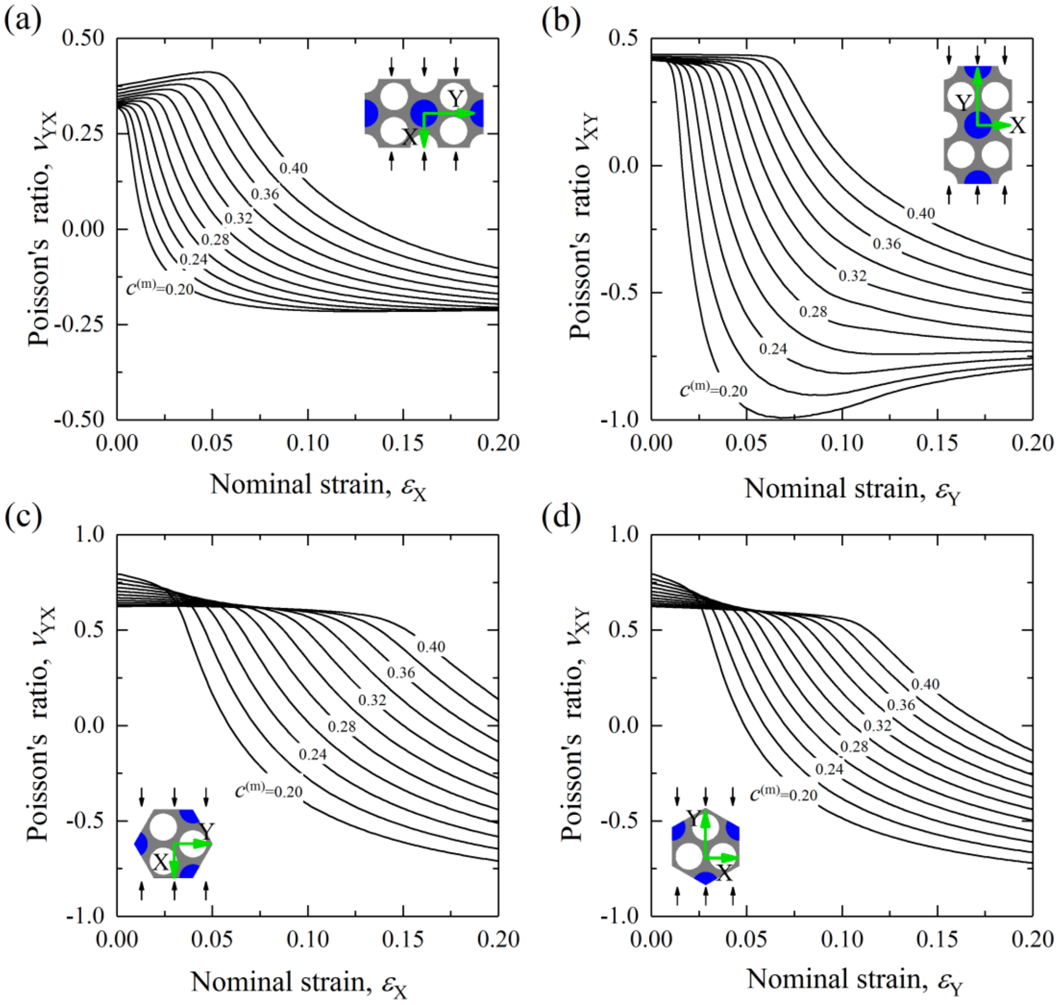

Figure 39. Dependence of Poisson's ratio on applied deformation for composites with various matrix volume fractions. The radii of voids and stiff inclusions are identical.

Figure 39 shows the evolution of Poisson's ratio with applied compressive strain for composites with various matrix volume fractions (with the radii of circular voids and stiff inclusions set to be identical). We note that, prior to the onset of instability, Poisson's ratio is positive for all considered cases. However, upon the onset of instabilities and microstructure transformations, an increase in deformation results in a dramatic drop in Poisson's ratio down to the negative regime. The analysis shows that a stronger auxetic or negative Poisson's ratio behavior can be obtained through decreasing the matrix volume fraction (i.e., increasing the void volume fraction).

Remarkable, for *composite A* loaded in X-material direction, the value of negative Poisson's ratio for the composite with lower matrix volume fraction is found to be nearly independent on applied strain after a certain deformation level. For instance, for *composite A* with $c^{(\mathrm{m})} = 0.2$, Poisson's ratio is nearly constant at $\nu_{\mathrm{YX}} \approx -0.21$ when applied strain $\varepsilon_{\mathrm{X}} \geq 0.08$. When *composite A* loaded in Y-material direction, we observe that Poisson's ratio for the case $c^{(\mathrm{m})} = 0.2$ can attain extreme values, for example, $\nu_{\mathrm{XY}} = -0.99$ at the applied strain $\varepsilon_{\mathrm{Y}} = 0.07$; however, this minimum is followed by an increase in Poison's ratio with further increase in the applied deformation. For *composite B*, we observe similar trends for loadings in X- and Y-material directions, especially for the composites with small matrix volume fractions.

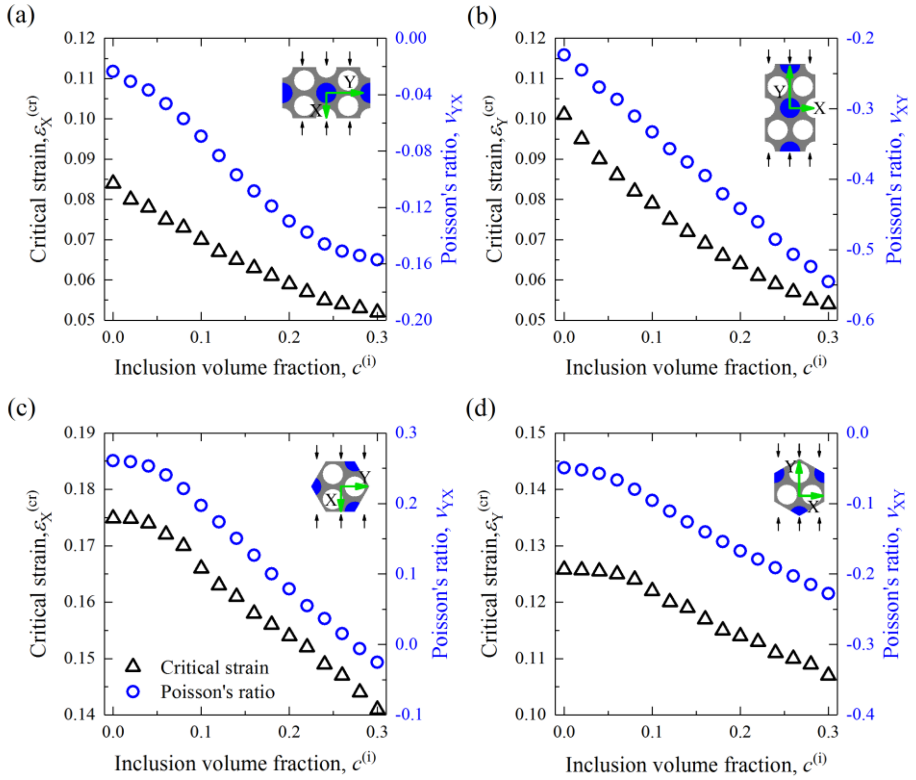

Figure 40. Dependence of critical strain and Poisson's ratio on inclusion volume fraction. Void volume fraction is fixed as $c^{(\mathrm{v})} = 0.45$. Poisson's ratio is evaluated at deformation level of $\varepsilon = 0.2$.

Furthermore, we examine the influence of the inclusion volume fraction on the composite behavior, while keeping the void volume fraction fixed. Figure 40 shows the dependence of the critical strain and Poisson's ratio on the inclusion volume fraction. The void volume fraction is fixed as $c^{(\mathrm{v})} = 0.45$ and Poisson's ratio is evaluated at $\varepsilon = 0.2$. Composites with larger stiff inclusions are observed to buckle earlier for all considered cases. Thus, a larger negative value of Poisson's ratio can be achieved at the same level of deformation by increasing the stiff inclusion volume fraction. For example, for *composite A* loaded in Y-material direction, an increase in the stiff inclusion volume fraction from $c^{(\mathrm{i})} = 0.0$ to 0.3 leads to a decrease in Poisson's ratio from $\nu_{\mathrm{XY}} = -0.22$ to -0.55. In *composite B* loaded in X-material direction, a change in the stiff inclusion volume fraction has a more significant influence on the buckling strain and Poisson's ratio in comparison to the composite loaded in Y-direction (compare Figure 40(c, d)). Moreover, it is notable that the effect of the inclusion volume fraction on the buckling strain and Poisson's ratio behavior can be stronger for composites with smaller radius of voids.

Finally, we investigate the role of shear modulus contrast on the soft composite behavior. Figure 41 shows the dependence of critical strain and Poisson's ratio on shear modulus contrast. The matrix volume fraction is fixed as $c^{(\mathrm{m})} = 0.65$ and the radii of voids and stiff inclusions are identical. Poisson's ratio is evaluated at $\varepsilon = 0.2$. Note that, for the considered range $\mu^{(\mathrm{i})}/\mu^{(\mathrm{m})}$ from 1 to 10^4, *composite A* buckles and forms the new periodicity consisted of 1×2 primitive unit cell, while *composite B* preserves its initial periodicity for both loading directions. We observe that the composite with a higher shear modulus contrast buckles earlier, resulting in a more significant negative Poisson’s ratio behavior. However, when the contrast $\mu^{(\mathrm{i})}/\mu^{(\mathrm{m})}$ is larger than 10^3, this effect becomes negligible. We note that a change in $\mu^{(\mathrm{i})}/\mu^{(\mathrm{m})}$ has more significant influence on the critical strain and Poisson’s ratio for the case of *composite A* loaded in Y-material direction (see Figure 41(b)). For example, an increase in the contrast $\mu^{(\mathrm{i})}/\mu^{(\mathrm{m})}$ from 1 to 10^3 can result in a decrease in critical strain from $\varepsilon_{cr} = 0.075$ to 0.054, and a decrease in Poisson’s ratio from $\nu_{\mathrm{XY}} = -0.397$ to -0.515. For the case of *composite B*, the composite loaded in X-material direction is more sensitive to a change in shear modulus contrast in comparison to the composite loaded in Y-material direction (compare Figure 41(c) with (d)).

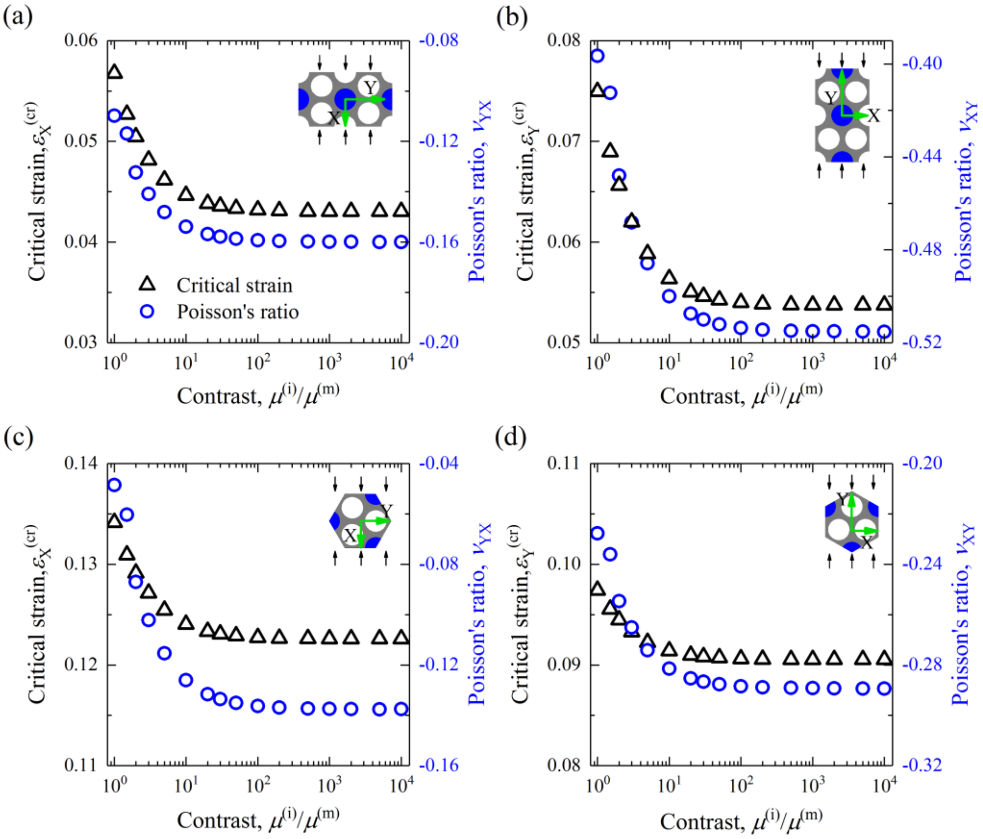

Figure 41. Dependence of critical strain and Poisson’s ratio on shear modulus contrast $\mu^{(\mathrm{i})}/\mu^{(\mathrm{m})}$. The matrix volume fraction is fixed as $c^{(\mathrm{m})} = 0.65$. The radii of voids and stiff inclusions are identical. Poisson’s ratio is evaluated at the deformation level of $\varepsilon = 0.2$.

6.5 Summary

We have investigated the instability-induced pattern transformations in multiphase composites consisted of circular voids and stiff inclusions periodically distributed in a soft elastomer. In this study, we specifically focused on the role of inclusion distribution and anisotropic property on the mechanical responses of the composites. We studied two types of stiff inclusion arrangements in the porous structure comprising of a triangular array of circular voids, where elastic instability can be exploited to trigger cooperative buckling of voids. Through the combination of simulations and experiments on the 3D printed composites, we have realized multiple new patterns. We showed that these new patterns can be tuned by altering the distribution of stiff inclusions, thus, switchable extremely soft and negative Poisson's ratio behavior can be tailored.

Furthermore, through the survey of the microstructure parameter space, we provide the trends for the changes in the effective properties as functions of the microstructure parameters. We have found that the composites may attain extreme values of negative Poisson's ratio for certain morphologies and loadings. Thus, the composites with square periodic arrangement of the stiff inclusions (*composite A*) with low matrix volume fractions have been identified as the advantageous configurations with high tunability of the effective properties by deformation. Moreover, the tailored composite morphologies allow to pre-design the onset of instabilities. Thus, we have found that the composites with larger void and/or stiff inclusion volume fractions, as well as a higher inclusion-to-matrix ratio of shear moduli, are more prone to buckling, and, hence, they exhibit a more pronounced negative Poisson’s ratio behavior. The composites with the square periodic inclusion arrangement (*composite A*) are more stable in comparison to the composites with the triangular periodic inclusion arrangement (*composite B*). Thus, the performance of the composites can be significantly tuned via altering the distribution of stiff inclusions, loading directions, phase volume fractions, and shear modulus contrast. The reported behavior of the soft microstructures can be potentially used in designing materials for energy dissipation and shock wave mitigation; vibration and noise management, and novel soft actuators with morphing abilities. These actuators can incorporate functionalized inclusions to respond to applied electrical [213] or magnetic field [137,140], potentially enabling future design of actively and/or remotely controlled functional materials. Finally, we note that – since the overall response of these materials is highly compressible, and even exhibiting auxetic behavior in the postbuckling regimes – the response to unidirectional tensile loadings may result in different behavior as compared to the compressive loading considered here. The effect of various loading conditions, such as tensile or bi-axial loadings, can be exploited to gain access to distinct pattern transformations, and, potentially, different behavior in the postbuckling regime [50,214,215].

Chapter 7

Oblique wave propagation in finitely deformed layered composite[*]

We study the influence of deformation on shear waves propagating at various angles in hyperelastic layered composites. We find that shear wave band gaps (forbidden frequency ranges) in periodic laminates exist only for waves propagating perpendicular to the layers, and the band gaps close suddenly if the incidence angle changes even slightly. However, the attenuation in the frequency range of the band gap decreases gradually with a change in the angle. Moreover, we observe the significant influence of deformation on the dispersion curves of oblique shear waves propagating in finitely deformed layered composites.

---

[*] Based on the published paper: Li J, Slesarenko V, Galich PI, Rudykh S. Oblique shear wave propagation in finitely deformed layered composites. Mech Res Commun 2018;87:21–8.

7.1 Introduction

Elastic wave propagation in solids has been an active topic of research due to its importance for many applications, such as seismology, nondestructive testing, acoustic filters, vibration damper, biomedical imaging, and acoustic cloaking. Recently, the field of architected microstructured metamaterials for manipulating elastic wave propagation has attracted significant attention [72–76,78,79,81–85,87,88,91,94,99]. Moreover, soft materials provide an opportunity to control elastic waves by deformation. This can be achieved through different effects of applied deformation – changes in microstructural geometry [69,92] and local material properties [57–59,97,216], or by a combination of these effects [65,80,217]. Furthermore, the influence of deformation can be further magnified by utilizing the elastic instability phenomenon. Buckling induced microstructure transformations can lead to formations of new periodic microstructures, thus, significantly influencing elastic wave propagation [6,62,93,102]. Experimental realization of such microstructured materials significantly depends on the development in material fabrications such as layer-by-layer fabricating and 3D printing techniques; these recently emerged techniques already allow manufacturing of microstructured materials at various length-scales [35,141,218–220].

Elastic wave propagation in finitely deformed homogeneous isotropic materials was pioneered by Biot [52], who investigated the influence of various cases of initial stress conditions on elastic wave propagations. Boulanger et al. [221] derived explicit expressions for phase velocities of shear and pressure waves propagation in compressible Hadamard materials. To account for the stiffening effects on elastic wave propagation, Galich et al. [57] studied the infinitesimal wave propagating in finitely deformed incompressible and compressible Gent materials and derived explicit expressions for phase velocities. By employing the homogenization method, Vinh and Merodio [222] investigated elastic wave propagation in soft tissue, which was considered as an incompressible transversely isotropic elastic solid. Vinh et al. [223] studied the influence of deformation and propagation direction on Rayleigh wave propagating in one family fiber-reinforced incompressible nonlinearly elastic half-space, this work was extended to two family fiber-reinforced elastic half-space by Nam et al. [224]. For the case of elastic waves propagating in layered composites (LCs), the pioneering work by Rytov [64] derived an explicit dispersion relation for steady state waves propagating perpendicular and parallel to the layers. In particular, for the case of waves propagating perpendicular to the layers, it was shown that the frequency spectrum consisted of an infinite number of modes with stop and pass bands. Recently, Galich et al. [65] investigated the influence of large deformation on the elastic waves in deformable laminates. Galich et al. [65] obtained estimates for long shear waves propagating in any direction of the finitely deformed laminates with incompressible neo-Hookean phases. In addition to the long wave estimates, classical results of Rytov [64] have been extended to account for the effects of finite deformations, thus, allowing investigation of the influence of deformation on shear and pressure wave band gaps in laminates. Galich et al. [21] also showed that the shear wave band gaps in (incompressible and compressible) neo-Hookean LCs do not depend on deformation, as the deformation induced change in the geometry is fully compensated by the change in the effective material properties.

In this work, we focus on oblique shear waves propagating in the finitely deformed LCs. We analyze the significant changes in the wave dispersion as the incidence angle starts to deviate from the normal case (wave propagation perpendicular to the layers) towards the oblique case. The most significant aspect is that the band gaps appear only for waves propagating perpendicular to the layers, and the band gaps do not appear if the propagation direction is changed even slightly. From the experimental point of view, it is extremely challenging to maintain the exact normal direction, so that the detection of the phenomenon may be affected by deviations in the actual propagation direction. While the band gaps close immediately, the transmission of the signal does not show a sudden change, but exhibit a gradual decrease with a change in the incidence angle from the normal direction. This was experimentally observed by Schneider et al [225], who found strong attenuation in the band gap area of normal elastic wave propagation in LCs with alternating poly (methyl methacrylate) and porous silica; moreover, Schneider et al [225] observed that the attenuation changed with a change in incidence angle. Here, we specifically focus on the influence of deformation on oblique shear wave propagation.

7.2 Simulations

Let us consider periodic LCs consisted of two alternating nearly incompressible neo-Hookean phases with volume fraction $v_a = d_a/d$ and $v_b = 1 - v_a$ (as shown in Figure 42(a)). Here and after, the quantities corresponding to phase a and phase b are denoted by subscripts $(\bullet)_a$ and $(\bullet)_b$, respectively. The constitutive behavior of each phase is defined through neo-Hookean strain energy function

$$W(\mathbf{F}_\xi) = \frac{\mu_\xi}{2}(\mathbf{F}_\xi : \mathbf{F}_\xi - 3) - \mu_\xi \ln(J_\xi) + \frac{\Lambda_\xi}{2}(J_\xi - 1)^2 , \tag{27}$$

where Λ_ξ is the first Lame constant, μ_ξ is the shear modulus, $\mathbf{F}_\xi$ is the deformation gradient, and $J_\xi \equiv \det(\mathbf{F}_\xi)$, where ξ stands for a and b. To maintain a nearly incompressible behavior of the phases, we set a high ratio between the first Lame constant and shear modulus ($\Lambda_\xi/\mu_\xi = 10^4$). Here we consider LCs in plane strain condition and apply macroscopic tension deformation along the layers (as shown in Figure 42(b)). The macroscopically applied deformation gradient is expressed as

$$\mathbf{F}_\xi = \lambda^{-1}\mathbf{e_1} \otimes \mathbf{e_1} + \lambda\mathbf{e_2} \otimes \mathbf{e_2} + \mathbf{e_3} \otimes \mathbf{e_3}, \tag{28}$$

where λ is the stretch ratio.

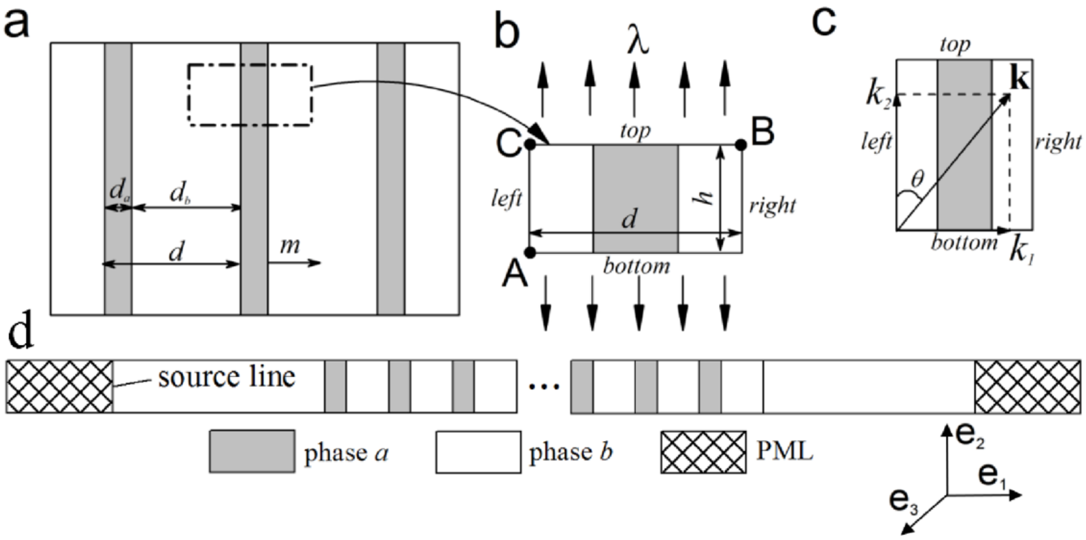

Figure 42. Schematic of the unit cell and boundary conditions. (a) Periodic LCs with alternating phases a and b, (b) Unit cell with periodic boundary conditions, (c) Bloch wave boundary conditions superimposed on the deformed state, (d) Schematic of calculating transmittance coefficient of shear wave propagating in periodic LCs.

To obtain the dispersion relations for shear waves propagating in finitely deformed LCs, we employ the Bloch wave analysis implemented in the finite element based code COMSOL 5.2a. A unit cell, as shown in Figure 42(b), is constructed for the simulations. The height of the unit cell, h, is set to be $0.1d$ to eliminate redundant eigenvalues and maintain reasonable computational time. The simulation procedures are performed in two steps: (**Step 1**) we apply an in-plane tension λ along the layer by the imposed periodic boundary conditions (Eq. (29)) to obtain the deformed state; (**Step 2**) we superimpose Bloch-Floquet periodic boundary conditions on the deformed unit cell (Eq. (30)). Then through solving the corresponding eigenvalue problems for a range of Bloch wave vectors [37,68,110], the dispersion relations for finitely deformed periodic LCs are obtained.

Step 1.

$$\begin{cases} u_1|_{right} = u_1|_{left} + u_1|_{\mathrm{B}} - u_1|_{\mathrm{C}} \\ u_2|_{right} = u_2|_{left} \end{cases}, \qquad \begin{cases} u_1|_{top} = u_1|_{bottom} \\ u_2|_{top} = u_2|_{bottom} + (\lambda - 1)h \\ u_1|_{\mathrm{A}} = u_2|_{\mathrm{A}} = 0 \end{cases}, \quad (29)$$

where the index *right*, *left*, *top,* and *bottom* denote the sides of the unit cell. A, B and C correspond to the nodes at the corner of the unit cell (see Figure 42(b)).

Step 2.

$$\begin{cases} u_1|_{right} = u_1|_{left} e^{-iK_1 d} \\ u_2|_{right} = u_2|_{left} e^{-iK_1 d} \end{cases}, \qquad \begin{cases} u_1|_{top} = u_1|_{bottom} e^{-iK_2 h} \\ u_2|_{top} = u_2|_{bottom} e^{-iK_2 h} \end{cases}, \quad (30)$$

where K_1 and K_2 are the components of Bloch wave vector $\mathbf{K}$ in the undeformed configuration. Note that the Bloch wave vectors in the undeformed ($\mathbf{K} = |\mathbf{K}|(\sin\theta_0 \mathbf{e_1} + \cos\theta_0 \mathbf{e_2})$) and deformed configurations ($\mathbf{k} = |\mathbf{k}|(\sin\theta \mathbf{e_1} + \cos\theta \mathbf{e_2})$) are related, namely, $\mathbf{k} = \mathbf{F}^{-\mathrm{T}}\mathbf{K}$ [226]. Here, the angles θ_0 and θ define the directions of Bloch wave vectors in the undeformed and deformed configurations (see Figure

42(c)), respectively. When the applied deformation takes the form of Eq. (28), the angles in the undeformed and deformed configurations are related as $\tan\theta = \lambda^2 \tan\theta_0$. Mesh sensitive analysis has been conducted to ensure that the relative error of the calculated frequency is less than 10^{-3}.

To analyze the transmittance spectra of the waves propagating in the periodic LCs, the standard frequency domain analysis is performed. A schematic representation of the numerical model is shown in Figure 42(d). An array of 32 unit cells is used in the numerical simulations. Two regions of homogenous matrix materials (4 times length of the period of the unit cell) are added to the left and right side of the LC. Perfectly matched layers (PMLs) are imposed on the two ends of the homogenous matrix regions to eliminate reflections. In addition, periodic boundary conditions are applied on the top and bottom boundaries. Finally, a harmonic vertical displacement with small amplitude is applied at the interface (denoted as the source line in Figure 42(d)) between the left perfectly matched layer (PML) and the homogeneous material region. By measuring the amplitudes of the displacements in the left and right homogenous matrix areas denoted as u_{out} and u_{in}, respectively, we obtain the transmittance coefficient defined as $\phi = 10\lg(u_{out}/u_{in})$.

7.3 Results and discussion

We start from consideration of the influence of small deviation in the wave propagation direction from the normal case (waves propagating perpendicular to the layers) on the dispersion relations. First, we compare the dispersion relations of shear waves propagating in undeformed and deformed LCs in the direction (a) perpendicular to the layers ($\theta_0 = \pi/2$) and (b) with a small deviation from the normal direction ($\theta_0 = 89\pi/180$). Here frequency is normalized as $f_n = \omega d\sqrt{\bar{\rho}/\tilde{\mu}}/(2\pi)$, where ω is the angular frequency, $\bar{\rho} = v_a\rho_a + v_b\rho_b$ is the average density, and $\tilde{\mu} = (v_a/\mu_\mathrm{a} + v_b/\mu_\mathrm{a})^{-1}$. In perfect agreement with the theoretical results [64,65], the dispersion structure for the normal case is periodic and possesses band gaps (denoted by the shaded grey areas in Figure 43(a, c)). The first shear wave band gap (BG) is in the range of the normalized frequency from 0.45 to 0.55 and it is not affected by deformation (see Figure 43(a, c)). This is in full agreement with the results by Galich et al [65] that showed that the BGs for shear waves propagating perpendicular to neo-Hookean layers are independent of the applied deformation. However, when the direction of propagation is changed even slightly, for example, $\theta_0 = 89\pi/180$, we observe the absence of BGs (see Figure 44(b) for the undeformed state and Figure 43(d) for the deformed state). We note that for relatively small normalized wavenumbers (see the range from 0 to 4 in Figure 43(b, d)), the dispersion curves for $\theta_0 = 89\pi/180$ are somewhat similar to the normal case. We also observe the peak frequencies of the lower branch increase with an increase in wavenumber (see Figure 43(b, d)), leading to the absence of the BGs as opposite to the normal case (see Figure 43(a, c)). Thus, the BGs of the undeformed and deformed LCs disappear immediately once the direction of wave propagation is changed from the perpendicular direction.

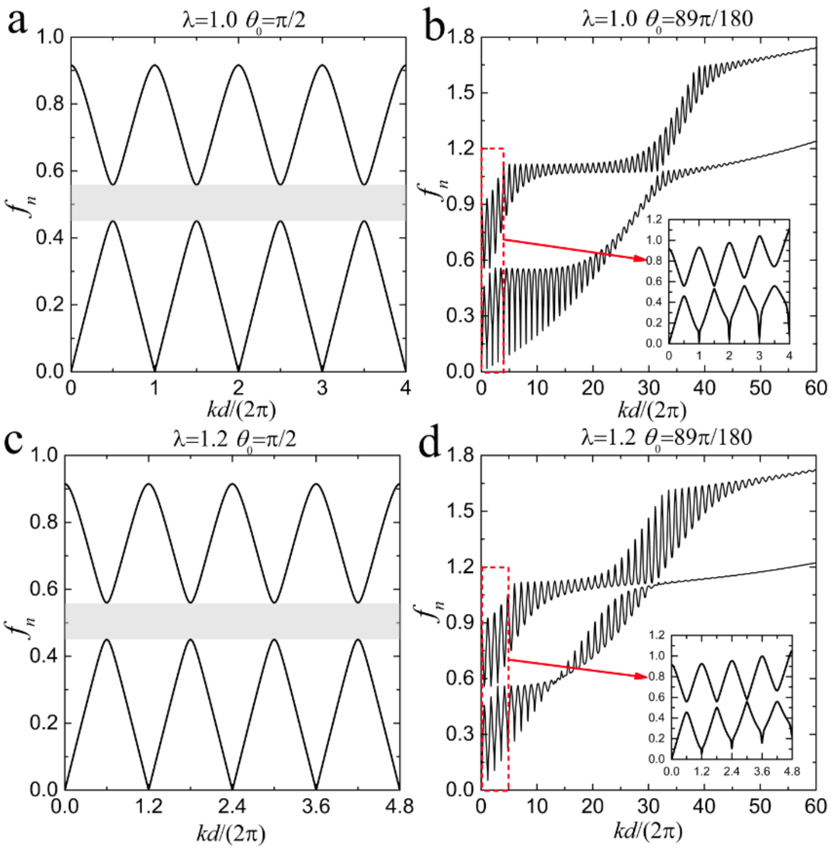

Figure 43. Dispersion diagram of shear waves propagating in LCs ($v_a = 0.20$, $\mu_a/\mu_b = 100$, $\rho_a/\rho_b = 1$).

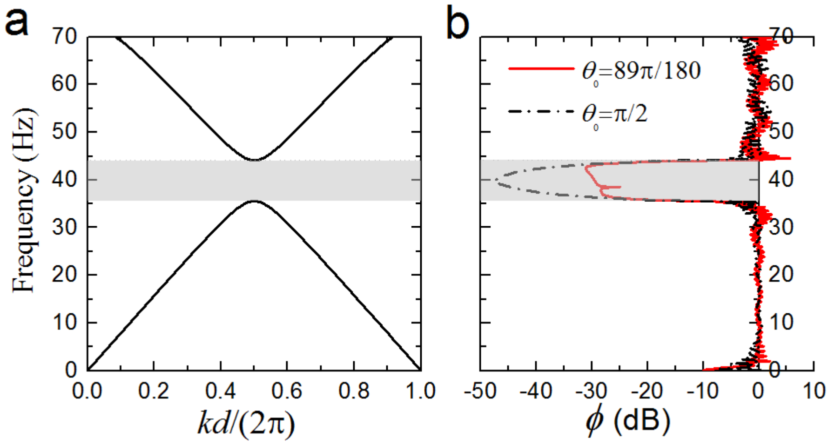

Figure 44. Band gaps and transmittance spectra for LC with $d = 1\text{m}, v_a = 0.20$, $\mu_a = 500\text{MPa}$, $\mu_b = 5\text{MPa}$, $\rho_a = \rho_b = 10^3\ \text{kg/m}^3$. (a) Band gaps of shear waves propagating perpendicular to the layers, (b) Transmittance spectra for shear waves propagating perpendicular to the layers ($\theta_0 = \pi/2$ – dash-dotted black curve) and at a slightly oblique angle ($\theta_0 = 89\pi/180$ – continuous red curve).

Next, we illustrate the attenuation characteristics for shear wave propagation in LCs for two cases: (a) normal case, (b) a small deviation from the normal case. The dispersion curves for shear waves propagating perpendicular to the layers are plotted in Figure 44(a), the transmittance spectra for different incidence angles are plotted in Figure 44(b). In the calculation of transmittance spectra of the LCs, the following geometrical and material parameters are used: $d = 1\text{m},\ v_a = 0.20,\ \mu_a = 500\text{MPa}$, $\mu_b = 5\text{MPa}$, $\rho_a = \rho_b = 10^3\ \text{kg/m}^3$. The continuous red curve corresponds to the case of $\theta_0 = 89\pi/180$, and the dash-dotted black curve is for the case of $\theta_0 = \pi/2$. When waves propagate perpendicular to the layers ($\theta_0 = \pi/2$), strong attenuations is observed in the frequency range of the band gap. Again, for the case with a slight deviation ($\theta_0 = 89\pi/180$), there is no band gap; however, the corresponding attenuations (in the band gap area of $\theta_0 = \pi/2$) are still significant, although it is reduced as compared to the normal case. Thus, the band gaps disappear immediately with a change in the incidence angle, but the transmittance characteristics change (decrease) gradually.

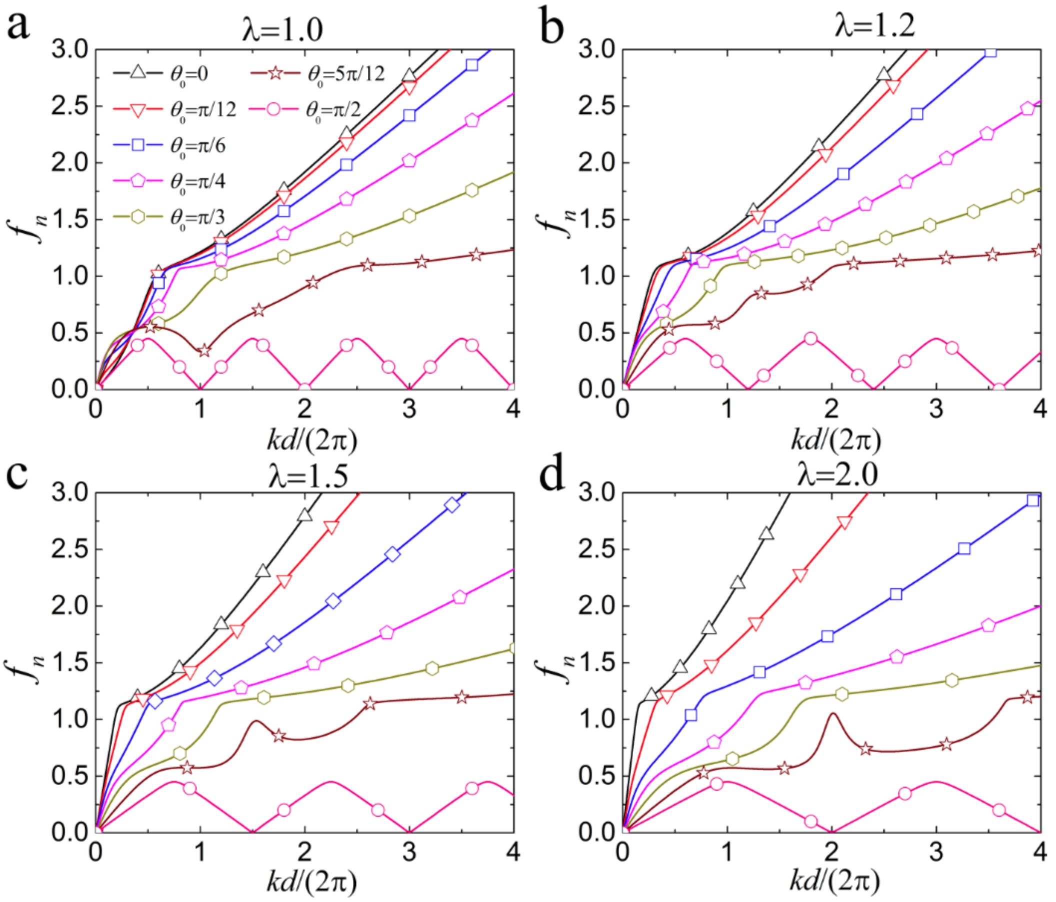

Figure 45. Dispersion curves for oblique shear waves propagating in LCs ($v_a = 0.20, \mu_a/\mu_b = 100$, $\rho_a/\rho_b = 1$) subjected to different deformation levels.

To clarify how the dispersion curves of shear wave propagation in LCs transform from perpendicular to parallel to the layer direction, we present the dispersion curves for various directions of shear wave propagation in Figure 45. We note that the dispersion curves are in good agreement with the long wave estimates [65]. Examples of comparisons between the long wave estimates and the Bloch wave numerical results are shown in Appendix G. Figure 45 shows that the dispersion curves gradually change from $\theta_0 = \pi/2$ to $\theta_0 = 0$ for the undeformed (a) and finitely stretched ($\lambda = 1.2$ (b), $\lambda = 1.5$ (c), and $\lambda = 2.0$ (d)) laminates. We note that in accordance with the previous results, the periodicity of the dispersion curves breaks once the incidence angle change from $\theta_0 = \pi/2$. We observe that for oblique cases the dispersion curves are characterized by the existence of two typical linear ranges (in the long wave range and in the short wave range). However, for the cases that are close to the normal case ($\theta_0 = \pi/2$), the transition range between these two linear regimes is characterized by significant nonlinearities (see, for example, the dispersion curves corresponding to $\theta_0 = 5\pi/12$ in Figure 45). Remarkably, the dispersion curves are significantly influenced by deformation (compare the corresponding curves in Figure 45(a, c)). For example, for $\theta_0 = 5\pi/12$, in the undeformed state, there is a prominent local minimum at $kd/2\pi \approx 1$; however, application of deformation of $\lambda = 1.5$ eliminates this local minimum. Also, for smaller angles, such as $\theta_0 \leq \pi/3$, we clearly find the applied tensile deformation in the direction of the layers leads to a sharper transition between these two linear regimes.

Figure 46 shows the examples of the influence of deformation on the dispersion curves for shear waves propagating at $\theta = \pi/6$ in LCs with various volume fractions and stiffness ratio of the phases. In agreement with our previous results, we also observe that the dispersion curves have two typical linear ranges, and the nonlinearities of the transition range between these two linear regimes increase with an increasing role of stiffer layers (higher shear modulus contrast and/or volume fraction of the stiffer layer). Meanwhile, the tensile deformation shifts the dispersion curves towards higher frequencies. For example, the LC with $v_a = 0.20$ and $\mu_a/\mu_b = 500$, the applied deformation of $\lambda = 1.5$ shifts the dispersion curve from $f_n = 0.99$ up to 1.47 as compared to the undeformed LC with $v_a = 0.05$, $\mu_a/\mu_b = 10$. Moreover, we observe that for longer waves the influence of deformation becomes less pronounced after certain deformation level (which depends on the material composition). For example, the frequency (at $kd/2\pi = 0.3$) from $f_n = 0.56$ (in the undeformed LC) up to 1.15; whereas the frequency increases only up to 1.20 with further increase of deformation up to $\lambda = 2.0$. The corresponding deformation level (after which the influence of deformation becomes less pronounced) is lower for LCs with more significant role of the stiffer layers (compare Figure 46(a, d)).

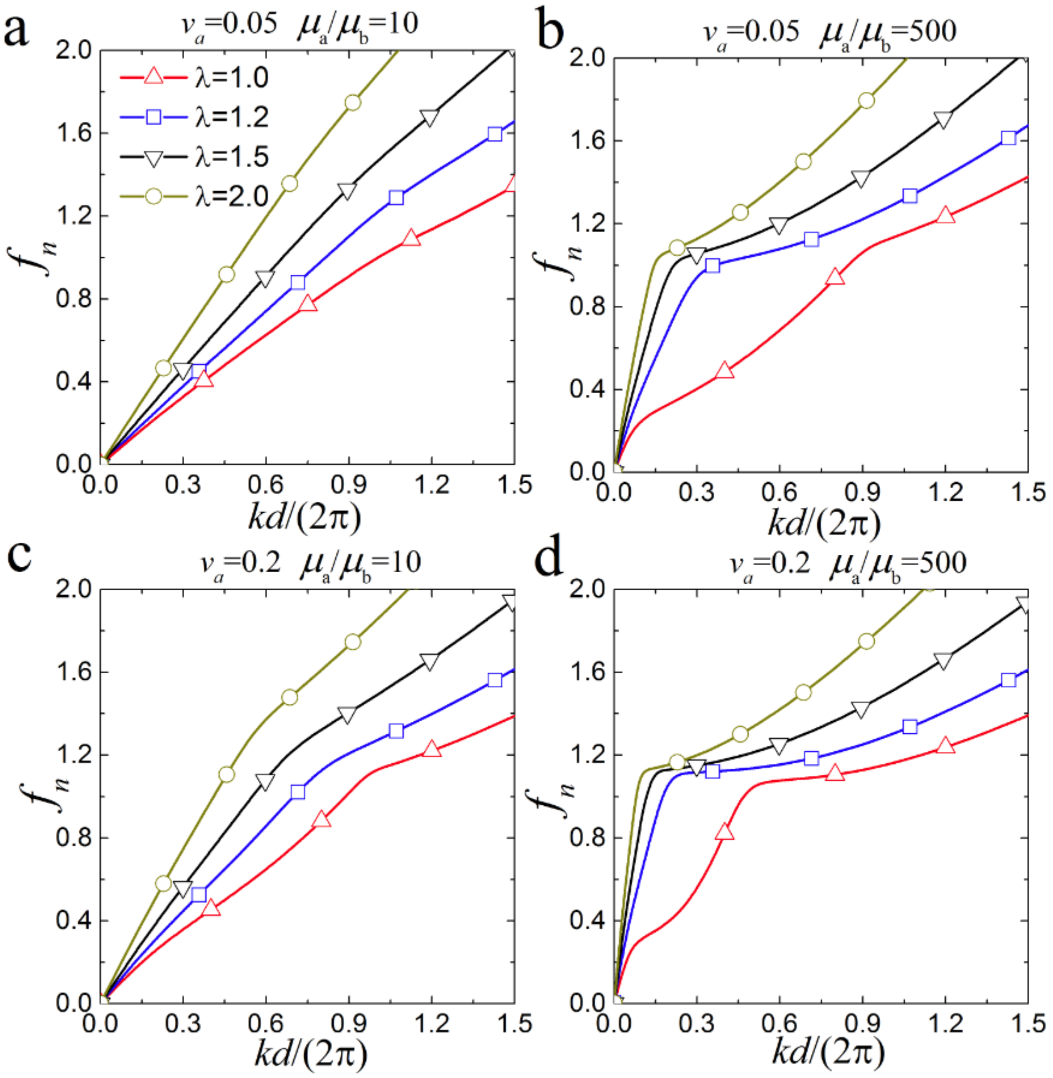

Figure 46. Dispersion curves for oblique shear waves propagating at $\theta = \pi/6$ in LCs with $\rho_a/\rho_b = 1$ and (a) $v_a = 0.05$, $\mu_a/\mu_b = 10$; (b) $v_a = 0.05$, $\mu_a/\mu_b = 500$; (c) $v_a = 0.20$, $\mu_a/\mu_b = 10$; (d) $v_a = 0.20$, $\mu_a/\mu_b = 500$.

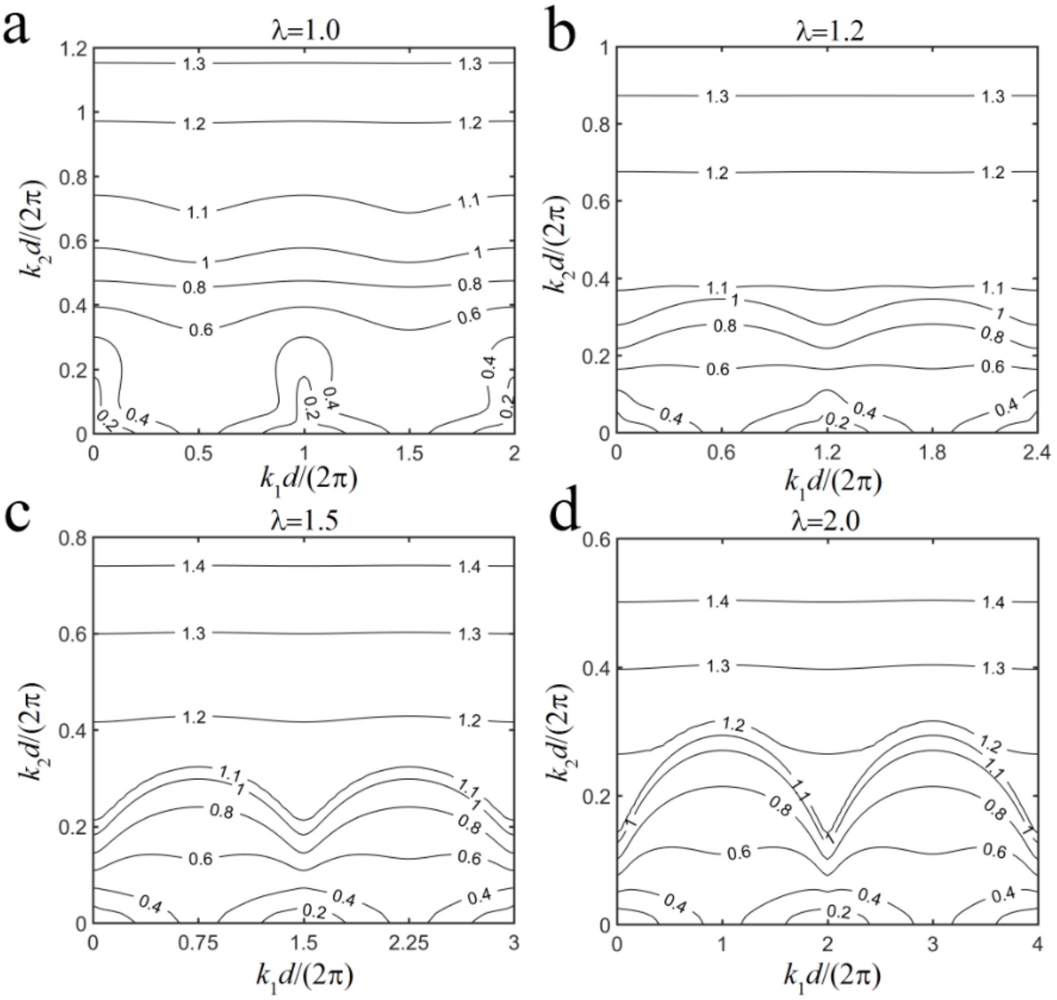

Figure 47. Equifrequency curves of shear waves propagating in undeformed (a) and deformed (b, c and d) LCs ($v_a = 0.20$, $\mu_a/\mu_b = 100$, $\rho_a/\rho_b = 1$).

To provide more details on the oblique shear waves, we plot the equifrequency curves in Figure 47. Due to the periodic laminate structure, the equifrequency curves are periodic in the direction of k_1, and are not periodic in the direction of k_2. Specially, for the equifrequency curves of undeformed LC in a period ($0 \leq k_1 d/(2\pi) \leq 1$), we find that the maximum and minimum frequency at a certain k_2 are always located at $k_1 d/(2\pi) = 0.5$ and $k_1 d/(2\pi) = 0$, respectively (see Figure 47(a)). However, an increase in k_2, leads to the situation when the equifrequncy curves become smooth, and the prominent minima/maxima points disappear. Furthermore, applied deformation leads to a change in the periodicity due to the change in the layer thicknesses, namely, the period of k_1 changes from $\Delta k_1 d/(2\pi) = 1$ (in the undeformed state) to $\Delta k_1 d/(2\pi) = 1.5$ for the laminates stretched to $\lambda = 1.5$ level (see Figure 47(c)). The applied deformation significantly influences the shape of the equifrequency curves. For example, compared with the contour lines at $f_n = 0.4, 0.6, 0.8$ in the undeformed state (see Figure 47(a)), we observe maximum frequency for a certain k_2 gradually changes from $k_1 d/(2\pi) = 0.5$ to $k_1 d/(2\pi) = 0$ in the deformed state (see Figure 47(c)). In addition, the deformation also shifts the equifrequency curves towards higher frequencies. For instance, the curves corresponding to $f_n = 1.2$ in the undeformed and deformed ($\lambda = 2.0$) sates are located at $k_2 d/(2\pi) \approx 0.97$ and 0.30, respectively.

7.4 Summary

We have studied shear waves propagating in finitely deformed LCs with nearly incompressible neo-Hookean phases. By application of Bloch wave analysis superimposed on large deformation, we obtained the dispersion curves for shear waves propagating at normal and oblique angles relative to the layers. We have found that the band gaps close immediately when the direction of wave propagation changes even slightly from the normal propagation direction – this is for both undeformed and deformed laminates. The attenuation, however, decreases gradually with a change in the direction of wave propagation. We have observed that the dispersion curves of shear waves propagating in LCs change suddenly when the direction of propagation changes (even slightly) from perpendicular to the layer direction. Further change in the propagation direction leads to a graduate change in the dispersion curves. For small deviation angles (from the normal case), the dispersion curves exhibit significant nonlinearities; and prominent picks are observed. These picks evolve with the further change in the angle, and, at certain oblique propagation direction, the dispersion curves are characterized by two linear ranges. The transition wavenumber between these two linear regimes depends on the LC composition, and the corresponding transition wavenumber is observed to increase with an increasing role of stiffer layers (higher shear modulus contrast and larger volume fraction of the stiffer layer).

The dispersion curves for the oblique waves are found to be significantly affected by the applied deformation. In particular, the highly nonlinear behavior of dispersion curves (for waves propagating at the angles close to the normal case), is significantly transformed through the applied deformation. More specifically, the local minima can be significantly smoothened and even transformed into local maxima by increasing the applied deformation level. Furthermore, for oblique waves propagating at large angles (relative to the normal case) corresponding to the “bi-linear” regime, we have observed that the increased tensile deformation shifted the dispersion curves towards higher frequencies. This is valid for both linear ranges (short and long wave ranges) of the oblique waves. For longer waves, however, the influence of deformation becomes less pronounced after certain deformation level, which is defined by LC composition (the deformation level is lower for LCs with more significant role of the stiffer layers).

Chapter 8

Conclusions and discussion

This thesis investigates the elastic instability phenomena in microstructured soft composites undergoing large deformations; in addition the work explores the application of large deformation-induced microstructure transformations to the control of small amplitude elastic wave propagation. In this thesis, the onset of instability, as well as the instability-induced pattern transformations in layered composites, 3D fiber composites, particulate composites, and multiphase composites are examined. Moreover, the thesis illustrates an application of employing these reversible microstructure transformations in periodic hyperelastic layered composites and multiphase composites to manipulate small amplitude elastic wave propagation.

Microscopic instabilities and small amplitude elastic wave propagation in finitely deformed laminates with compressible hyperelastic phases are first investigated. By means of Bloch-Floquet instability analysis implemented in the finite element code, the onset of instability in compressible hyperelastic layered composites is examined. It is found that compressible layered composites are observed to be more stable, and the critical stretch ratio increases with a decrease in phase compressibility. This stabilizing effect can be contributed by the additional freedom in accommodating deformation in compressible layered composites as compared to the constrained incompressible layered composites. Moreover, microscopic instability-induced wavy patterns are utilized to tune the band gap of elastic waves propagating in layered composites perpendicular to the layer direction. It is shown that instability-induced wavy patterns expand the widths of shear wave band gaps and shift them to higher frequency ranges. However, the compressive deformation significantly shifts pressure wave band gaps to lower frequency ranges and narrow the widths of pressure wave band gaps.

Then, the elastic instabilities and pattern formations in single stiff fiber and periodically distributed stiff fiber embedded in a soft matrix subjected to axial compressive loads are considered. For single 3D fiber-reinforced composite, an explicit expression predicting the buckled wavelength is derived based on the Winker foundation model, showing that the critical wavelength has a linear dependence on the stiff fiber diameter. This prediction is further verified by experimental observations on 3D-printed single fiber composites. For composites with periodically distributed 3D fibers, through a combination of experiments on 3D-printed fiber composites and rigorous Bloch-Floquet numerical instability analyses, it is observed that the critical wavenumber and critical strain decrease with an increase in fiber volume fraction. In particular, since the interactions between stiff fibers weaken with a decrease in stiff fiber volume fraction, the critical wavenumber and critical strain of periodic fiber composite in the dilute limit are found to attain the value given by the derived theoretical formulas for single fiber system. For composites with the rectangular in-plane periodicity of fibers, it is found that the buckling mode develops in the direction, where the fibers are close to each other; and an increase in the periodicity aspect ratio leads to a decrease in critical wavenumber and critical strain.

Next, Instability-induced pattern transformations in soft particulate composites are studied. Experiments on 3D-printed samples show that the system of stiff inclusions periodically distributed in a soft elastomeric matrix experiences dramatic microstructure changes upon the development of elastic instabilities. In particular, the formation of domain microstructures is observed in the composites with a dense arrangement of stiff inclusions, for which macroscopic instabilities are predicted. Moreover, an increase in periodicity aspect ratio or decrease in concentration of the inclusions can result in a transition from domain patterns to cooperatively wavy pattern. These experimental observations on the buckled strain and buckled wavelength are in a qualitative agreement with numerical instability results. However, it is noted that macroscopic instability analysis only predicts the critical strain for the domain pattern, while the prediction on the pattern length-scale requires more detailed microscopic analysis.

After that, the instability phenomena in auxetic multiphase composites consisting of stiff inclusions and voids periodically distributed in a soft matrix are examined. The instability-induced pattern transformations lead to the collapses of circular voids, thus giving rise to the Negative Poisson’s ratio behaviors. Thanks to the anisotropic property of the composite microstructure, identical composite can morph into distinct patterns depending on the loading direction. These distinct patterns are characterized by significantly different auxetic behaviors. Moreover, it is illustrated that these reversible pattern transformations open significant complete band gaps (i.e., both shear and pressure band gaps) in remarkable low-frequency ranges.

Furthermore, the role of inclusion distribution on the behaviors of multiphase composites is discussed. To ensure a uniform collapse of voids, the inclusions are distributed in either square or triangular periodic configurations, while the voids are distributed in the triangular periodic array. In a combination of simulation and experiment on 3D-printed composites, multiple new patterns are realized by altering the distribution of inclusions and loading direction. Comparison of experimental and numerical results on deformation sequences, stress-strain curves, and Poisson's ratio shows good agreements. Then, a survey of microstructure space in periodic composite shows that the composites with larger void and/or stiff inclusion volume fractions, as well as a higher inclusion-to-matrix ratio of shear moduli, are more prone to buckling, thus exhibiting a more pronounced negative Poisson's ratio behavior; and the composites with the square periodic inclusion arrangement are more stable in comparison to the composites with the triangular periodic inclusion arrangement. Therefore, the performance of the composites can be significantly tuned through altering the distribution of stiff inclusions, loading direction, phase volume fraction, and shear modulus contrast.

Finally, the oblique shear wave propagation in finitely deformed layered composites with nearly incompressible neo-Hookean phases is investigated. By application of Bloch wave analysis superimposed on the deformed state, it is found that the band gaps close immediately when the direction of wave propagation deviates even slightly from the normal (i.e., perpendicular to the layers) propagation direction

– this is for laminate in the undeformed and deformed state. However, the attenuation decreases gradually with a change in the wave propagation direction. It is observed that the dispersion curves of oblique waves have the linear short and long wave ranges, and the nonlinearities of the transition regimes between these two linear regimes significantly depend on the applied deformation and laminate compositions (i.e., shear modulus contrast and stiffer layer volume fraction).

In conclusion, this work illustrates that various pattern formations can be pre-designed in microstructured soft composites through the elastic instability phenomenon. The instability-induced changes in microstructural geometry and local material properties can be employed to tune the propagation of small amplitude elastic waves in these composites. It is noted that the material systems considered here are assumed to be hyperelastic, and inelastic behavior is not examined here. The analytical and numerical predictions are in good agreement with the experimental realizations of the microstructure transformations in soft 3D printed-composites under low strain-rate or quasi-static loadings.

Appendix

A. Approximation of the effective stiffness K of Winkler foundation model for incompressible material

Winkler foundation model is employed to investigate the buckling behavior of a stiff fiber embedded in a soft matrix subjected to a compressive load along the fiber. The matrix is approximated as an array of springs with effective stiffness *K* acting only in the radial direction. An elastic circular stiff fiber with radius *r* buckles in the mode of $u(z) = A\cos(kz)$, where A and $k = 2\pi/l$ are the amplitude and wave number, respectively; l is the wavelength. The effective stiffness *K* can be expressed as [127]

$$K = \frac{16\pi G_m(1-\nu_m)}{2(3-4\nu_m)K_0(\tilde{k})+K_1(\tilde{k})\tilde{k}}, \tag{A1}$$

where $\tilde{k} = kr$, K_0 and K_1 are the modified Bessel functions of the second kind.

We note that for the buckling of an infinite length stiff fiber embedded in a soft matrix, $\tilde{k} \ll 1$, Eq. (A1) can be significantly simplified. At first, $K_0(\tilde{k})$ can be expanded as [227]

$$\begin{aligned} K_0(\tilde{k}) = &-\left\{\ln\left(\frac{\tilde{k}}{2}\right) + \gamma\right\}\left(1 + \frac{\tilde{k}^2}{2^2} + \frac{\tilde{k}^4}{2^2\times 4^2} + \frac{\tilde{k}^6}{2^2\times 4^2\times 6^2} + \cdots\right) + \frac{\tilde{k}^2}{2^2} + \frac{\tilde{k}^4}{2^2\times 4^2}\left(1 + \frac{1}{2}\right) \\ &+ \frac{\tilde{k}^6}{2^2\times 4^2\times 6^2}\left(1 + \frac{1}{2} + \frac{1}{3}\right) + \cdots, \end{aligned} \tag{A2}$$

where γ=0.577 is the Euler's constant.

Since $\tilde{k} \ll 1$, we neglect the terms of the order higher than 2, then Eq. (A2) is approximated as

$$K_0(\tilde{k}) \approx -\left\{\ln\left(\frac{\tilde{k}}{2}\right) + \gamma\right\} = -\ln\left(\frac{e^\gamma}{2}\tilde{k}\right). \tag{A3}$$

Furthermore, $K_1(\tilde{k})\tilde{k}$ has the following approximation [228] when $\tilde{k} \ll 1$,

$$K_1(\tilde{k})\tilde{k} \approx 1. \tag{A4}$$

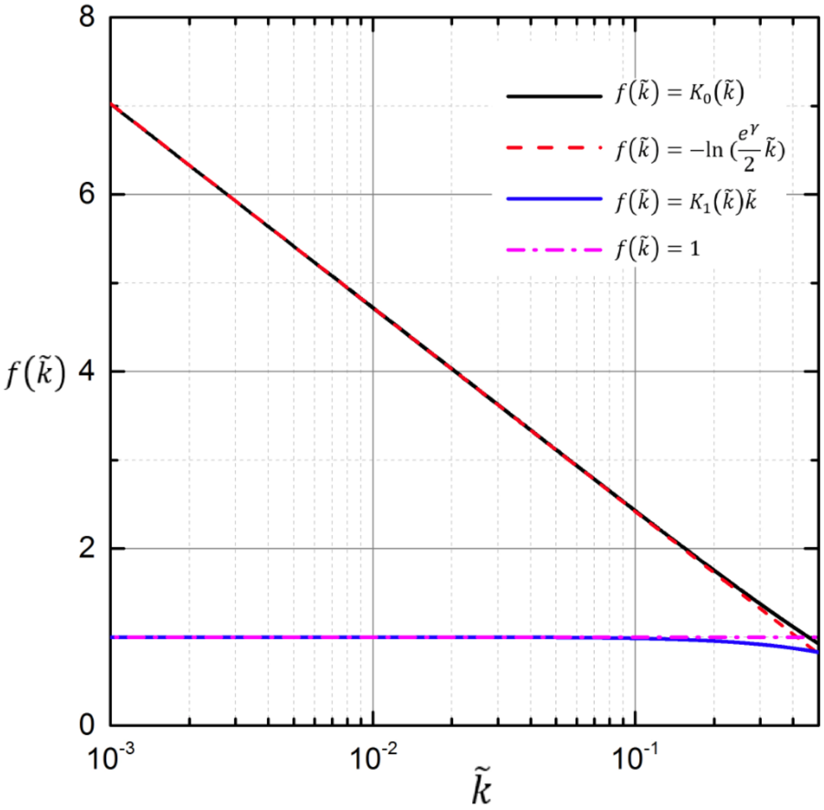

Figure A1. Comparison of the approximated value with the exact value.

Figure A1 shows the values of the modified Bessel function of second kind $K_0(\tilde{k})$ and $K_1(\tilde{k})$ and their estimates for the argument $10^{-3} < \tilde{k} < 0.4$. In the considered range, the estimates (A3) and (A4) provide very accurate approximation for the exact values of Bessel functions. For instance, for $\tilde{k}$=0.1, the estimates (A3) and (A4) produce the values of 2.419 and 1, respectively, while the exact values of $K_0(0.1) =$2.427 and $0.1K_1(0.1) =$0.985. We note that although $K_0(\tilde{k}) \to \infty$ with $\tilde{k} \to 0$, the convergence $K_0(\tilde{k}) \to \infty$ is very slow, for example, $K_0(10^{-10})$ =23.14.

Then, under the soft matrix incompressibility assumption (ν_m=0.5), substitution of (A3) and (A4) into (A1) yields

$$K \approx \frac{8\pi G_m}{-2\ln\left(\frac{e^{\gamma}}{2}\tilde{k}_{cr}\right)+1} = \frac{4\pi G_m}{-\ln\left(\frac{e^{\gamma-\frac{1}{2}}}{2}\tilde{k}_{cr}\right)}. \qquad \text{(A5)}$$

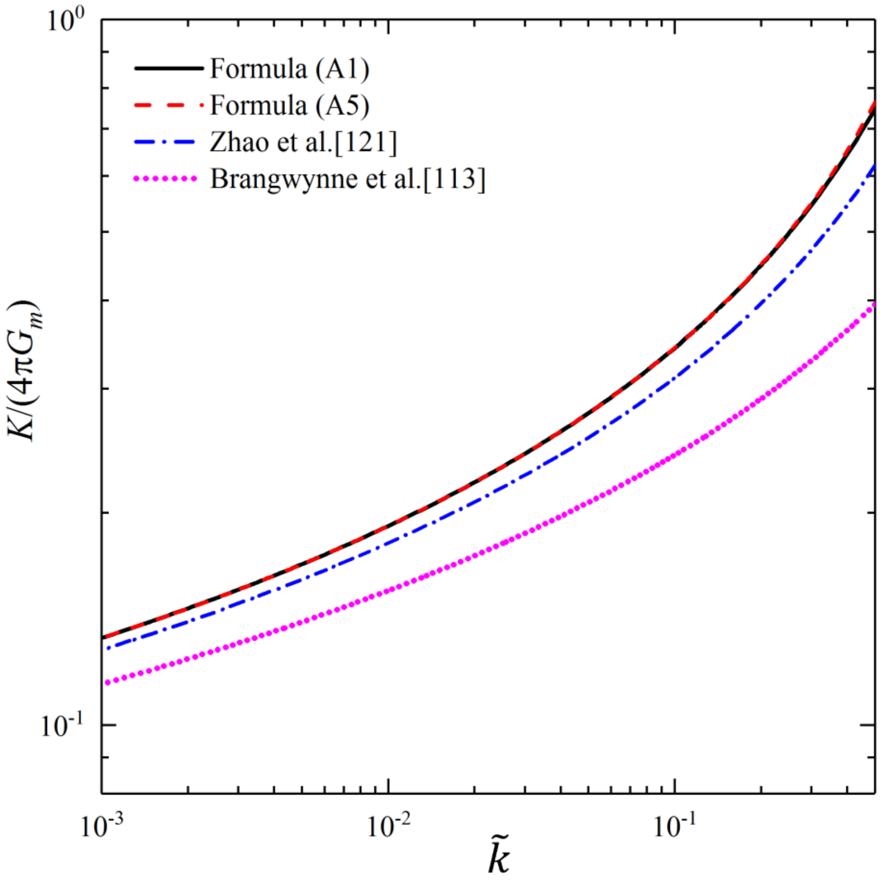

Figure A2. Comparison of effective stiffness K obtained by the approximate expressions Eq. (A5), Brangwynne et al.[113] and Zhao et al. [121] with the original formula (A1).

Different ways to simplify the expression (A1) are reported in the literature (see, for example, Brangwynne et al.[113] and Zhao et al. [121]), where the second term in the denominator is usually neglected. However, according to the results presented in Figure 17 and Figure A1, even for relatively high shear modulus contrast, both terms in the denominator of expression (A1) are of the same order, and should not be neglected. For example, for incompressible fiber and soft matrix ($\nu_f = \nu_m$=0.5), and shear modulus contrast $G_f/G_m = 10^6$, the normalized critical wavenumber $\tilde{k}_{cr}$ is 0.033, and $2K_0\big(\tilde{k}_{cr}\big) \approx 7K_1(\tilde{k}_{cr})\tilde{k}_{cr}$. Figure A2 shows a comparison of the exact value of effective stiffness K with estimate (A5) as well as the approximations reported in [113] and [121] plotted as functions of $\tilde{k}$. We observe that the derived in this work expression (A5) shows an excellent accuracy in approximations of the original expression (A1). Moreover, we note that the inaccuracy of the approximations of the original expression decrease with a decrease in the normalized wavenumber. Since the normalized wavenumber decreases with an increase in shear modulus contrast (see Figure 17), it means that the approximate expressions ((A5), [113], [121]) provide more accurate results in the range of higher shear modulus contrast.

B. The energy landscape and instability of particulate composite

The simulations are performed by using the finite element code COMSOL 5.2a. The material behavior of the soft matrix and stiff inclusion are modeled as nearly incompressible neo-Hookean hyperelastic model, whose strain energy density function is defined as

$$W(\mathbf{F}) = \frac{\mu}{2}(\mathbf{F}:\mathbf{F} - 2) - \mu \ln(\det(\mathbf{F})) + \frac{\Lambda}{2}(\ln(\det(\mathbf{F})))^2, \qquad \text{(B1)}$$

where μ and Λ denote the initial shear modulus and the first Lame constant, respectively. $\mathbf{F} = \frac{\partial \mathbf{x}}{\partial \mathbf{X}}$ is the deformation gradient, with mapping of a material point from the reference position $\mathbf{X}$ to its current location $\mathbf{x}$. The ratio $\Lambda/\mu = 10^3$ is set resulting in a nearly incompressible response of the material. The soft matrix material is modeled with the initial shear modulus $\mu_m = 0.2\,\mathrm{MPa}$; the inclusion-to-matrix contrast ratio in shear moduli is chosen as $\mu_i/\mu_m = 10^3$ so that the deformation mostly develops in the soft matrix material. The plane-strain conditions are imposed in the simulations.

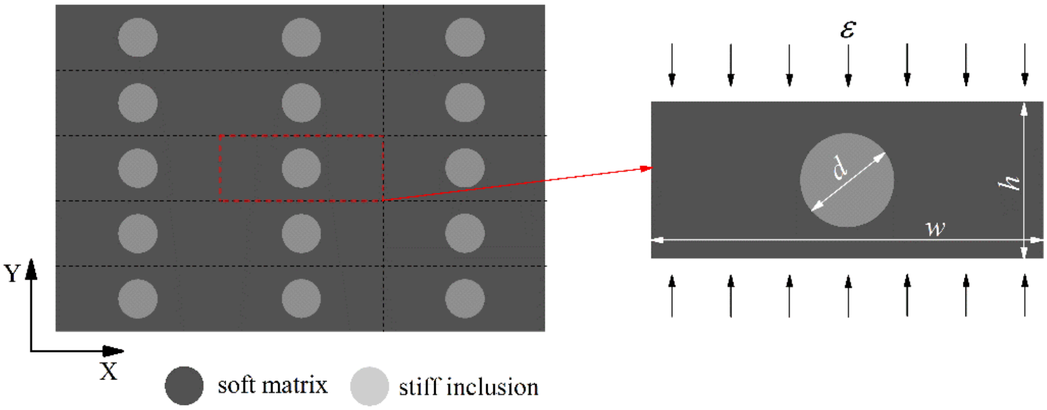

Figure B1. Schematic illustration of the primitive unit cell and applied loading.

To detect the onset of instability in periodic particulate soft composite and the associated critical strain ε_{cr} and critical wavenumber k_{cr}, we employ the Bloch-Floquet technique superimposed on the deformed state.[1,2] We consider the primitive unit cell (as shown in Figure B1), characterized by the periodicity aspect ratio $\eta = w/h$, and inclusion spacing ratio $\xi = d/h$. The procedures to identify the onset of instability are performed in two steps.

Step 1: The primary solution for a finitely deformed state is obtained numerically. The macroscopic deformation is applied through imposing the periodic displacement boundary conditions on the edges of the unit cell; the periodic boundary conditions are defined as

$$\mathbf{u}_B - \mathbf{u}_A = (\bar{\mathbf{F}} - \mathbf{1})(\mathbf{X}_B - \mathbf{X}_A), \tag{B2}$$

where A and B are the paired nodes periodically located at the opposite edges of the unit cell; $\mathbf{u} = \mathbf{x}(\mathbf{X}) - \mathbf{X}$ is the displacement field; $\bar{\mathbf{F}}$ is the macroscopic deformation gradient, which can be given as

$$\bar{\mathbf{F}} = \lambda_1 \mathbf{e}_1 \otimes \mathbf{e}_1 + \lambda_2 \mathbf{e}_2 \otimes \mathbf{e}_2, \tag{B3}$$

where $\mathbf{e}_1$ and $\mathbf{e}_2$ are the unit vectors in X and Y directions. $\lambda_2 = 1 - \varepsilon$ and λ_1 is obtained from the solution of the boundary value problem. Moreover, rigid body motions are prevented by fixing a node at the corner of the unit cell.

Step 2: the Bloch-Floquet boundary conditions are imposed on the edges of the deformed unit cell as follows:

$$\mathbf{u}(\mathbf{X} + \mathbf{R}) = \mathbf{u}(\mathbf{X})e^{-i\mathbf{K}\cdot\mathbf{R}}, \tag{B4}$$

where **R** defines the distance between the paired nodes on the opposite edges of the unit cell; **K** is the wave vector. Then, we solve the corresponding eigenvalue problem for a range of wave vectors **K**. These steps are repeated with gradually increased macroscopic deformation until a non-trivial zero eigenvalue is detected at a certain deformation level. Then, the corresponding applied deformation and wavenumber at which the appearance of the non-trivial zero eigenvalue is identified as the critical strain ε_{cr} and critical wavenumber $\mathbf{K}_{cr}$. In particular, when $\mathbf{K}_{cr} \to \mathbf{0}$, the macroscopic instability or so-called long wave mode is detected.[3]

Once the primary solution is obtained, the average energy density can be calculated through integration over the unit cell area S, namely,

$$W(\bar{\mathbf{F}}) = \frac{1}{S}\int_{\Omega} W(\bar{\mathbf{F}}, \mathbf{X})dS. \tag{B5}$$

Figure B2 (a) shows the composite energy as a function of the applied deformation for the composite with $\eta = 1.0$, $\xi = 0.8$; the average energy density is normalized by the matrix shear modulus. The average energy function (shown in Figure B2 (a)) is convex for the considered compressive strain range. However, when the compressive strain exceeds a certain value, an addition of the shearing deformation results in a decrease in the composite average strain energy, thus indicating that by developing shearing deformation the composite can attain a lower energy state, upon achieving the critical value of the compressive strain. This is illustrated in Figure B2 (b) showing the normalized average strain energy density as functions of the compressive strain ε and amount of shear γ.

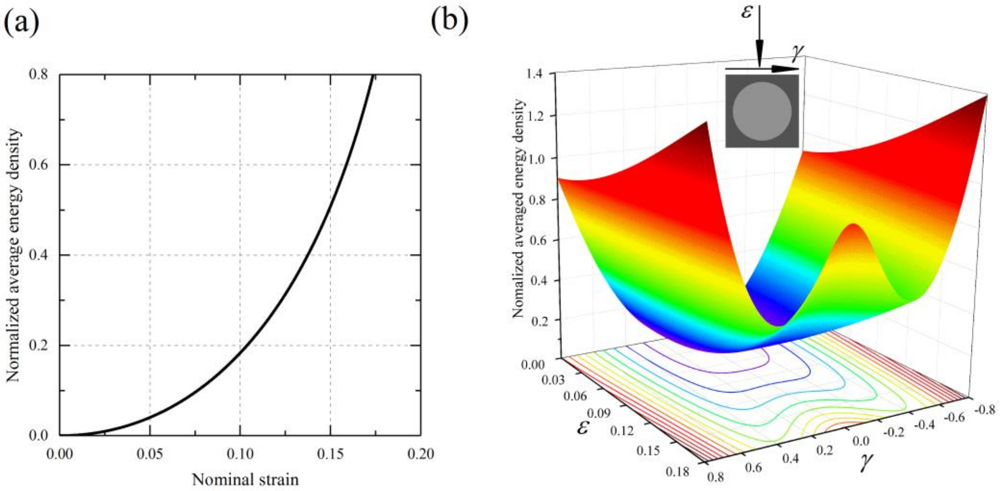

Figure B2. (a) Energy curve of the primary solution. (b) Average energy surface of the composite subjected to the combined compressive strain ε and shear γ. The results are given for the composite with $\eta = 1.0$, $\xi = 0.8$.

C. Visualization of deformed configuration

The distinct deformed configurations of the composite loaded in X-direction (a, c, e, g) or in Y-direction (b, d, f, h) are shown in Figure C1. For completeness, we show the deformed configuration in two selections of the enlarged unit cell: the stiff inclusions located in the middle of the unit cell (a, b, e, f); and the stiff inclusions located in the corners of the unit cell (c, d, g, h) (as shown in Figure C1). Although, the buckled patterns for the composite loaded in X- or Y-direction are similar in the initially post-buckling deformation stage (compare the deformed configuration in Figure C1 at $\varepsilon = 0.05$); at larger deformation levels, clearly distinct deformed void shapes are formed in the composite (compare the deformed configuration in Figure C1 at $\varepsilon = 0.2$). Thus, the composite develops different patterns when loaded in different directions.

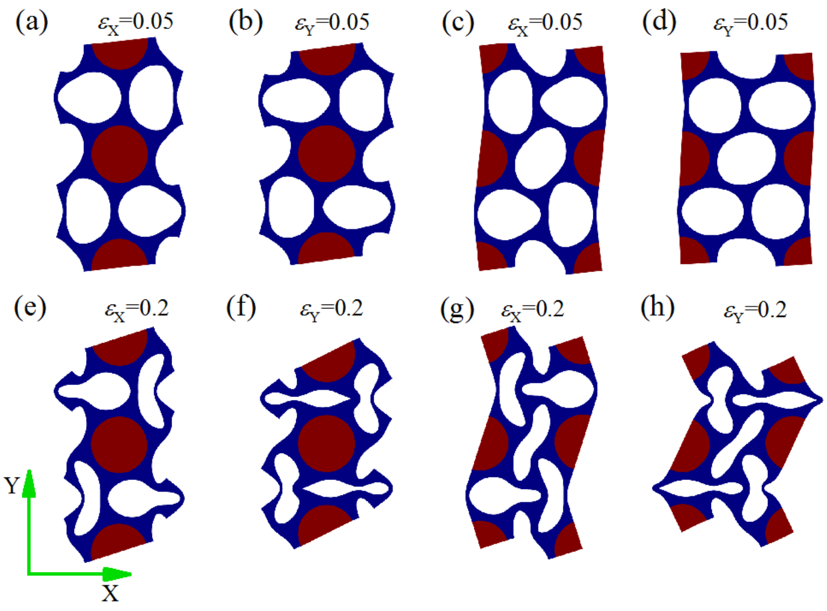
(a) ε_X=0.05
(b) ε_Y=0.05
(c) ε_X=0.05
(d) ε_Y=0.05
(e) ε_X=0.2
(f) ε_Y=0.2
(g) ε_X=0.2
(h) ε_Y=0.2
Y
X

Figure C1. Distinct pattern formation in the composite loaded in X- and Y- material directions.

D. Effect of matrix volume fraction on composite effective Young’s modulus

The dependence of effective Young’s moduli of the composite loaded in X- and Y- material directions on matrix volume fraction is shown in Figure D1. The effective Young’s modulus is calculated as the initial slope of the stress-strain curve in small deformations. The numerical simulations have been verified against the analytical estimates for matrix-inclusion composite with hexagonal periodic unit cell [200]. Here, we consider nearly incompressible material for matrix and inclusion, and $\mu^{(i)}/\mu^{(m)} = 10^3$. The reported effective Young’s modulus is normalized by the corresponding maximum value of the modulus. We observe that the effective modulus of the composite increases with an increase in matrix volume fraction for both X- or Y- material loading directions, and the effective modulus of the composite loaded in Y- material direction is always larger than that of the composite loaded in X-material direction. Moreover, for the geometrical limits, namely, $c^{(m)} = 0.093 \text{ and } 1$, the normalized effective modulus attains 0 and 1, respectively.

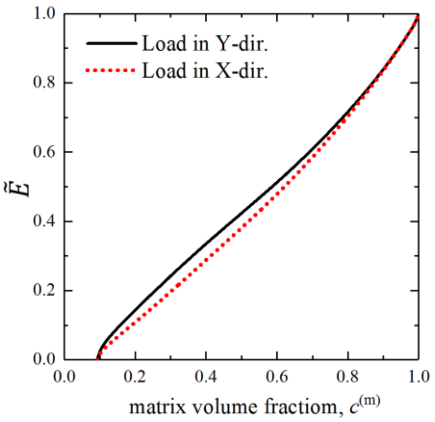

Figure D1. Dependence of normalized effective Young’s moduli of the composite loaded in X- and Y- material directions on matrix volume fraction.

E. Evaluation of Poisson's ratio

To evaluate the value of Poisson's ratio at different levels of applied compressive strain in experimentally observed pattern transformations, we identified the selected stiff inclusion centroids and representative elements by their row and column indices (see Figure E1). Considering the rotational symmetry of the buckled patterns (see Figure 29 (a, d)), the nominal strain for each considered representative element is calculated as

$$\varepsilon_{\mathrm{X}}^{[i,j]} = \frac{x^{(i,j+1)} - x^{(i,j)} + x^{(i+1,j+1)} - x^{(i+1,j)}}{4a_0} - 1, \tag{E1}$$

$$\varepsilon_{\mathrm{Y}}^{[i,j]} = \frac{y^{(i+1,j)} - y^{(i,j)} + y^{(i+1,j+1)} - y^{(i,j+1)}}{2\sqrt{3}a_0} - 1. \tag{E2}$$

The corresponding Poisson's ratio for each representative element is defined as

$$\upsilon_{\mathrm{XY}}^{[i,j]} = -\frac{\varepsilon_{\mathrm{X}}^{[i,j]}}{\varepsilon_{\mathrm{Y}}^{[i,j]}}, \quad \upsilon_{\mathrm{YX}}^{[i,j]} = -\frac{\varepsilon_{\mathrm{Y}}^{[i,j]}}{\varepsilon_{\mathrm{X}}^{[i,j]}}. \tag{E3}$$

Then, the average Poisson's ratio $\upsilon_{\mathrm{XY}} = \langle \upsilon_{\mathrm{XY}}^{[i,j]} \rangle$ and $\upsilon_{\mathrm{YX}} = \langle \upsilon_{\mathrm{YX}}^{[i,j]} \rangle$ for the considered 15 representative elements are computed.

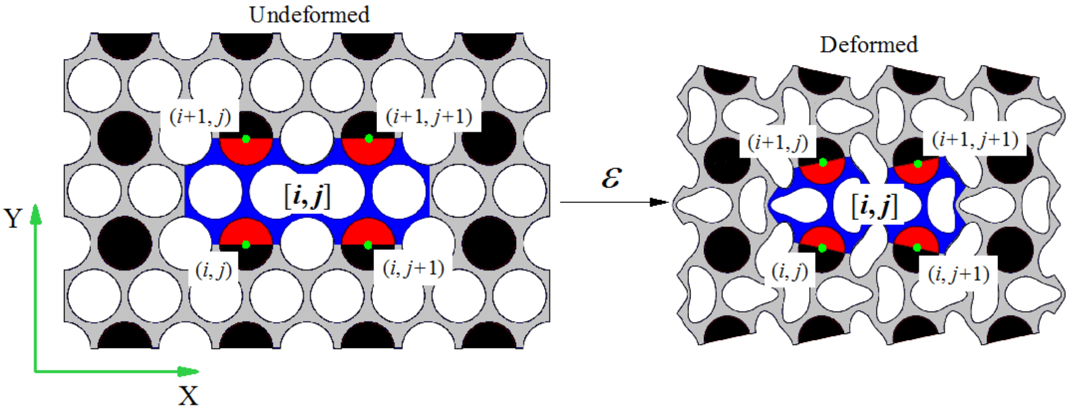

Figure E1. Schematic diagram of the method for experiments to calculate Poisson's ratio.

F. Calculation of the effective Poisson's ratio

Here we describe the procedure for calculating the effective Poisson's ratio based on the experimental testing. In experiments, the deformation process was recorded by a high-resolution digital camera producing a sequence of frames at increasing strain levels. The position for the centroid of each circular stiff inclusion, marked by black dot, is tracked through the digital image analysis of the recorded frames. To diminish the boundary effect, we focus on the central part of the finite size specimens, where more uniform deformation is observed for each updated unit cell. The selected areas for the tested specimens are highlighted in green color in Figure F1 (b-e). The selected representative elements and stiff inclusions are numbered by their row and column indices. The applied strain for the representative element is calculated as

$$\varepsilon_{\mathrm{XX}}^{[i,j]} = \frac{x^{(i,j+1)} - x^{(i,j)} + x^{(i+1,j+1)} - x^{(i+1,j)} - 2L_{\mathrm{X}}^{0}}{2L_{\mathrm{X}}^{0}}, \tag{F1}$$

$$\varepsilon_{\mathrm{YY}}^{[i,j]} = \frac{y^{(i+1,j)} - y^{(i,j)} + y^{(i+1,j+1)} - y^{(i,j+1)} - 2L_{\mathrm{Y}}^{0}}{2L_{\mathrm{Y}}^{0}}, \tag{F2}$$

where L_{X}^{0} and L_{Y}^{0} are defined in undeformed state, given in Figure F1 (a). The Poisson's ratios for the considered representative element $[i,j]$ when loaded in X- and Y-material directions are calculated as

$$\upsilon_{\mathrm{YX}}^{[i,j]} = -\frac{\varepsilon_{\mathrm{YY}}^{[i,j]}}{\varepsilon_{\mathrm{XX}}^{[i,j]}}, \tag{F3}$$

$$\upsilon_{\mathrm{XY}}^{[i,j]} = -\frac{\varepsilon_{\mathrm{XX}}^{[i,j]}}{\varepsilon_{\mathrm{YY}}^{[i,j]}}. \tag{F4}$$

Finally, the effective Poisson's ratio is given as the averaged value for nine selected representative elements.

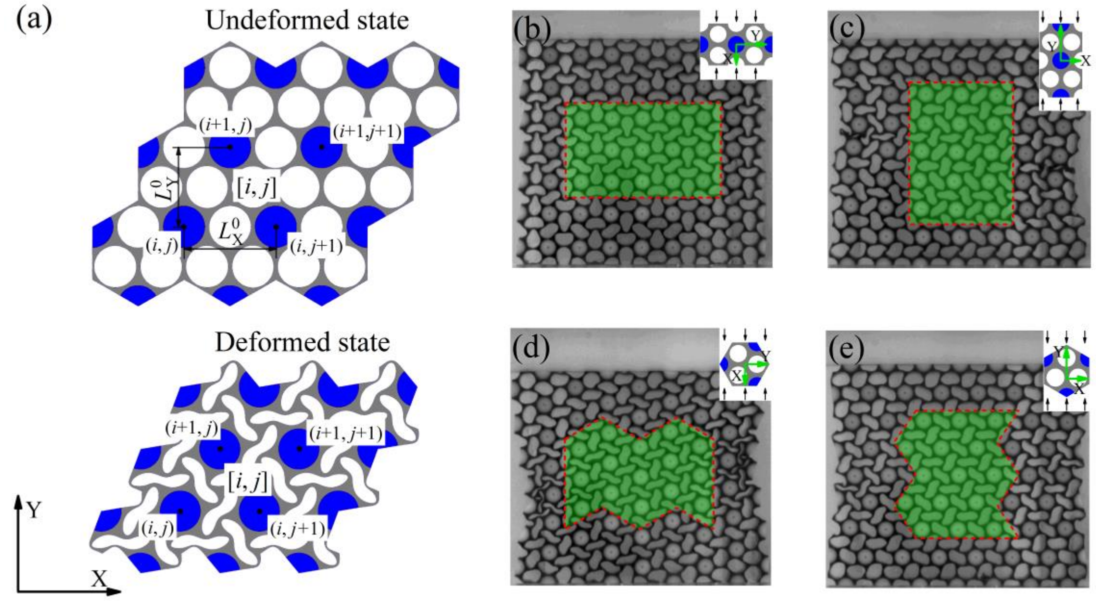
(a)
Undeformed state
(i+1, j)
(i+1,j+1)
[i, j]
L_Y^0
L_X^0
(i, j)
(i, j+1)
Deformed state
(i+1, j)
(i+1, j+1)
[i, j]
(i, j)
(i, j+1)
Y
X
(b)
(c)
(d)
(e)
Y
X

Figure F1. Schematic diagrams (a) and selected areas (b-e) for calculation of the effective Poisson's ratio.

G. Comparisons of long wave estimates and Bloch wave numerical analyses

The long wave estimates of shear waves propagating in LCs subjected to any homogeneous deformation can be expressed as

$$\omega = \sqrt{b/\bar{\rho}}\,, \tag{G1}$$

where

$$b = \overline{\mu}\left(\mathbf{k}\cdot\overline{\mathbf{B}}\cdot\mathbf{k}\right) + (\tilde{\mu} - \overline{\mu})\left(\mathbf{k}\cdot\overline{\mathbf{F}}\cdot\mathbf{m}\right)^2 + + \frac{\overline{\mu}-\tilde{\mu}}{\alpha^2}\left(\frac{4\beta_k^2}{\alpha} - k^2\right)\left(\alpha - \frac{\beta_k^2}{k^2}\right) \tag{G2}$$

where $\mathbf{k}$ is the wave vector, $k = |\mathbf{k}|$ is the wavenumber, $\overline{\mathbf{F}} = v_a\mathbf{F}_a + v_b\mathbf{F}_b$ is the average deformation gradient; $\overline{\mathbf{B}} = \overline{\mathbf{F}}\cdot\overline{\mathbf{F}}^{\mathrm{T}}$ is the average left Cauchy-Green deformation tensor; $\mathbf{m}$ is the direction of LCs (see Figure 42 (a)); $\alpha = \mathbf{m}\cdot\overline{\mathbf{C}}^{-1}\cdot\mathbf{m}$, $\beta_k = \mathbf{k}\cdot\overline{\mathbf{F}}^{\mathrm{T}}\cdot\mathbf{m}$, $\overline{\mu} = v_a\mu_{\mathrm{a}} + v_b\mu_{\mathrm{b}}$.

Here we show the comparison of the analytical long wave estimates and Bloch wave numerical results for shear waves propagating in LCs in the direction of Bloch wave vector $\theta_0 = \pi/12$. The examples are given for LCs subjected to a deformation of $\lambda = 1.5$. Figure E1 (a, b) shows the comparisons for LCs with $v_a = 0.20$, $\mu_a/\mu_b = 10$ and $\mu_a/\mu_b = 500$, respectively; Figure E1 (c, d) shows the results for $v_a = 0.05$, $\mu_a/\mu_b = 10$ and $\mu_a/\mu_b = 500$, respectively. Here we consider LCs with the phases characterized by identical densities. The continuous black curves represent the Bloch wave numerical results, and the dash-dotted red curves correspond to the long wave estimates. For LCs with small volume fractions and shear modulus contrasts, such as shown in Figure E1 (c), $v_a = 0.05$, $\mu_a/\mu_b = 10$, the long wave estimate is in good agreement with the result of simulation up to the wavelengths comparable to the period of LC. However, with an increase in volume fraction and shear modulus contrast, the difference increases. For instance, for LCs with $\mu_a/\mu_b = 10, v_a = 0.05$ and $v_a = 0.20$, the long wave estimate curves and Bloch wave numerical curves start to differ after wavenumber $kd/(2\pi) \approx 0.4$ and 0.2, respectively. For LCs with $\mu_a/\mu_b = 1000$, the significant differences are observed after the wavenumber $kd/(2\pi) \approx 0.05$ $(v_a = 0.05)$ and 0.03 $(v_a = 0.20)$, respectively. Thus, the difference of long wave estimates increases with an increase in volume fraction and shear modulus contrast. This observation is similar to the one for three dimensional hyperelastic fiber composites [110].

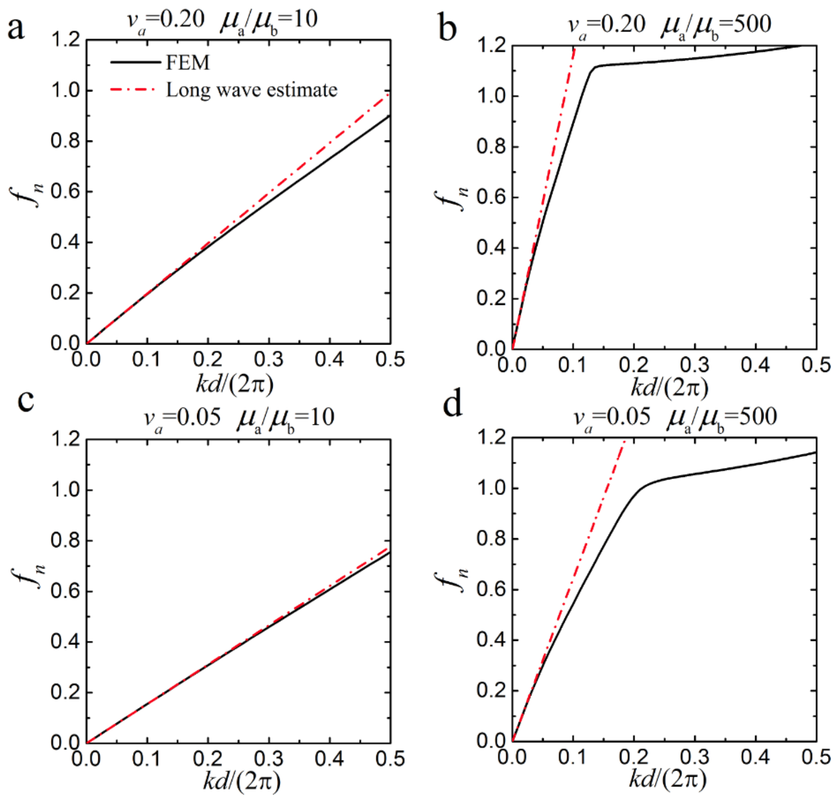

Figure E1. Comparisons of long wave estimates and numerical analyses for shear waves propagating in LCs with $\theta_0 = \pi/12$. LCs are considered as $\rho_a/\rho_b = 1$ and (a) $v_a = 0.20$, $\mu_a/\mu_b = 10$ (b) $v_a = 0.20$, $\mu_a/\mu_b = 500$ (c) $v_a = 0.05$, $\mu_a/\mu_b = 10$ (d) $v_a = 0.05$, $\mu_a/\mu_b = 500$. The LCs are subjected to a tension of $\lambda = 1.5$.

Bibliography

[1] Shan S, Kang SH, Raney JR, Wang P, Fang L, Candido F, et al. Multistable Architected Materials for Trapping Elastic Strain Energy. Adv Mater 2015;27:4296–301.

[2] Acome E, Mitchell SK, Morrissey TG, Emmett MB, Benjamin C, King M, et al. Hydraulically amplified self-healing electrostatic actuators with muscle-like performance. Science 2018;359:61–5.

[3] Kim Y, Yuk H, Zhao R, Chester SA, Zhao X. Printing ferromagnetic domains for untethered fast-transforming soft materials. Nature 2018;558:274–9.

[4] Yuan C, Mu X, Dunn CK, Haidar J, Wang T, Qi HJ. Thermomechanically Triggered Two-Stage Pattern Switching of 2D Lattices for Adaptive Structures. Adv Funct Mater 2018;28:1705727.

[5] Zhao Z, Wu J, Mu X, Chen H, Qi HJ, Fang D. Desolvation Induced Origami of Photocurable Polymers by Digit Light Processing. Macromol Rapid Commun 2017;38:1600625.

[6] Shan S, Kang SH, Wang P, Qu C, Shian S, Chen ER, et al. Harnessing Multiple Folding Mechanisms in Soft Periodic Structures for Tunable Control of Elastic Waves. Adv Funct Mater 2014;24:4935–42.

[7] Fu H, Nan K, Bai W, Huang W, Bai K, Lu L, et al. Morphable 3D mesostructures and microelectronic devices by multistable buckling mechanics. Nat Mater 2018;17:268–76.

[8] Wang Y, Yang R, Shi Z, Zhang L, Shi D, Wang E, et al. Super-Elastic Graphene Ripples for Flexible Strain Sensors. ACS Nano 2011;5:3645–50.

[9] Overvelde JTB, Kloek T, D'haen JJA, Bertoldi K. Amplifying the response of soft actuators by harnessing snap-through instabilities. Proc Natl Acad Sci 2015;112:10863–8.

[10] Chan EP, Smith EJ, Hayward RC, Crosby AJ. Surface Wrinkles for Smart Adhesion. Adv Mater 2008;20:711–6.

[11] Li J, Slesarenko V, Rudykh S. Microscopic instabilities and elastic wave propagation in finitely deformed laminates with compressible hyperelastic phases. Eur J Mech - A/Solids 2019;73:126–36.

[12] Li J, Slesarenko V, Galich PI, Rudykh S. Instabilities and pattern formations in 3D-printed deformable fiber composites. Compos Part B Eng 2018;148:114–22.

[13] Li J, Pallicity TD, Slesarenko V, Goshkoderia A, Rudykh S. Domain Formations and Pattern Transitions via Instabilities in Soft Heterogeneous Materials. Adv Mater 2019;31:1807309.

[14] Li J, Slesarenko V, Rudykh S. Auxetic multiphase soft composite material design through instabilities with application for acoustic metamaterials. Soft Matter 2018;14:6171–80.

[15] Li J, Rudykh S. Tunable microstructure transformations and auxetic behavior in 3D-printed multiphase composites: The role of inclusion distribution. Compos Part B Eng 2019;172:352–62.

[16] Li J, Slesarenko V, Galich PI, Rudykh S. Oblique shear wave propagation in finitely deformed layered composites. Mech Res Commun 2018;87:21–8.

[17] Bushnell D. Buckling of Shells-Pitfall for Designers. AIAA J 1981;19:1183–226.

[18] Kochmann DM, Bertoldi K. Exploiting Microstructural Instabilities in Solids and Structures: From Metamaterials to Structural Transitions. Appl Mech Rev 2017;69:050801.

[19] Shim J, Shan S, Košmrlj A, Kang SH, Chen ER, Weaver JC, et al. Harnessing instabilities for design of soft reconfigurable auxetic/chiral materials. Soft Matter 2013;9:8198.

[20] Shim J, Wang P, Bertoldi K. Harnessing instability-induced pattern transformation to design tunable phononic crystals. Int J Solids Struct 2015;58:52–61.

[21] Yang D, Mosadegh B, Ainla A, Lee B, Khashai F, Suo Z, et al. Buckling of Elastomeric Beams Enables Actuation of Soft Machines. Adv Mater 2015;27:6323–7.

[22] Rosen BW. Mechanics of composite strengthening. In: Fibre Composite Materials. Am. Soc. Met., Ohio: 1965, p. 37–75.

[23] Triantafyllidis N, Maker BN. On the Comparison Between Microscopic and Macroscopic Instability Mechanisms in a Class of Fiber-Reinforced Composites. J Appl Mech 1985;52:794.

[24] Parnes R, Chiskis A. Buckling of nano-fibre reinforced composites: a re-examination of elastic buckling. J Mech Phys Solids 2002;50:855–79.

[25] Nestorović MD, Triantafyllidis N. Onset of failure in finitely strained layered composites subjected to combined normal and shear loading. J Mech Phys Solids 2004;52:941–74.

[26] Geymonat G, Müller S, Triantafyllidis N. Homogenization of nonlinearly elastic materials, microscopic bifurcation and macroscopic loss of rank-one convexity. Arch Ration Mech Anal 1993;122:231–90.

[27] Kittel C. Introduction to solid state physics. New York: Wilely; 1996.

[28] Qiu GY, Pence TJ. Loss of Ellipticity in Plane Deformation of a Simple Directionally Reinforced Incompressible Nonlinearly Elastic Solid. J Elast 1997;49:31–63.

[29] Merodio J, Ogden RW. Material instabilities in fiber-reinforced nonlinearly elastic solids under plane deformation. Arch Mech 2002;54:525–52.

[30] Merodio J, Ogden RW. Instabilities and loss of ellipticity in fiber-reinforced compressible non-linearly elastic solids under plane deformation. Int J Solids Struct 2003;40:4707–27.

[31] Merodio J, Ogden RW. Remarks on instabilities and ellipticity for a fiber-reinforced compressible nonlinearly elastic solid under plane deformation. Quart Appl Math 2005;63:325–33.

[32] Merodio J, Ogden RW. On tensile instabilities and ellipticity loss in fiber-reinforced incompressible non-linearly elastic solids. Mech Res Commun 2005;32:290–9.

[33] Merodio J, Ogden RW. Tensile instabilities and ellipticity in fiber-reinforced compressible non-linearly elastic solids. Int J Eng Sci 2005;43:697–706.

[34] Volokh KY. Loss of ellipticity in elasticity with energy limiters. Eur J Mech - A/Solids 2017;63:36–42.

[35] Li Y, Kaynia N, Rudykh S, Boyce MC. Wrinkling of interfacial layers in stratified composites. Adv Eng Mater 2013;15:921–6.

[36] Slesarenko V, Rudykh S. Harnessing viscoelasticity and instabilities for tuning wavy patterns in soft layered composites. Soft Matter 2016;12:3677–82.

[37] Slesarenko V, Rudykh S. Microscopic and macroscopic instabilities in hyperelastic fiber composites. J Mech Phys Solids 2017;99:471–82.

[38] Abeyaratne R, Triantafyllidis N. An Investigation of Localization in a Porous Elastic Material Using Homogenization Theory. J Appl Mech 1984;51:481–5.

[39] Mullin T, Deschanel S, Bertoldi K, Boyce MC. Pattern Transformation Triggered by Deformation. Phys Rev Lett 2007;99:084301.

[40] Triantafyllidis N, Nestorović MD, Schraad MW. Failure Surfaces for Finitely Strained Two-Phase Periodic Solids Under General In-Plane Loading. J Appl Mech 2006;73:505–15.

[41] Zhang Y, Matsumoto EA, Peter A, Lin P, Kamien RD, Yang S. One-Step Nanoscale Assembly of Complex Structures via Harnessing of an Elastic Instability. Nano Lett 2008;8:1192–6.

[42] Singamaneni S, Bertoldi K, Chang S, Jang JH, Thomas EL, Boyce MC, et al. Instabilities and Pattern Transformation in Periodic, Porous Elastoplastic Solid Coatings. ACS Appl Mater Interfaces 2009;1:42–7.

[43] Singamaneni S, Bertoldi K, Chang S, Jang JH, Young SL, Thomas EL, et al. Bifurcated Mechanical Behavior of Deformed Periodic Porous Solids. Adv Funct Mater 2009;19:1426–36.

[44] Overvelde JTB, Bertoldi K. Relating pore shape to the non-linear response of periodic elastomeric structures. J Mech Phys Solids 2014;64:351–66.

[45] Overvelde JTB, Shan S, Bertoldi K. Compaction Through Buckling in 2D Periodic, Soft and Porous Structures: Effect of Pore Shape. Adv Mater 2012;24:2337–42.

[46] Babaee S, Shim J, Weaver JC, Chen ER, Patel N, Bertoldi K. 3D Soft Metamaterials with Negative Poisson's Ratio. Adv Mater 2013;25:5044–9.

[47] Shim J, Perdigou C, Chen ER, Bertoldi K, Reis PM. Buckling-induced encapsulation of structured elastic shells under pressure. Proc Natl Acad Sci 2012;109:5978–83.

[48] Florijn B, Coulais C, van Hecke M. Programmable Mechanical Metamaterials. Phys Rev Lett 2014;113:175503.

[49] Florijn B, Coulais C, van Hecke M. Programmable mechanical metamaterials: the role of geometry. Soft Matter 2016;12:8736–43.

[50] Overvelde JTB, Dykstra DMJ, de Rooij R, Weaver J, Bertoldi K. Tensile Instability in a Thick Elastic Body. Phys Rev Lett 2016;117:094301.

[51] Li J, Wang Y, Chen W, Wang YS, Bao R. Harnessing inclusions to tune post-buckling deformation and bandgaps of soft porous periodic structures. J Sound Vib 2019;459:114848.

[52] Biot MA. The Influence of Initial Stress on Elastic Waves. J Appl Phys 1940;11:522–30.

[53] Hayes M, Rivlin RS. Propagation of a plane wave in an isotropic elastic material subjected to pure homogeneous deformation. Arch Ration Mech Anal 1961;8:15–22.

[54] Currie P, Hayes M. Longitudinal and Transverse Waves in Finite Elastic Strain. Hadamard and Green Materials. IMA J Appl Math 1969;5:140–61.

[55] Boulanger P, Hayes M. Finite-amplitude waves in deformed Mooney-Rivlin materials. Q J Mech Appl Math 1992;45:575–93.

[56] Boulanger P, Hayes M, Trimarco C. Finite-amplitude plane waves in deformed Hadamard elastic materials. Geophys J Int 1994;118:447–58.

[57] Galich PI, Rudykh S. Influence of stiffening on elastic wave propagation in extremely deformed soft matter: from nearly incompressible to auxetic materials. Extrem Mech Lett 2015;4:156–61.

[58] Chang Z, Guo HY, Li B, Feng XQ. Disentangling longitudinal and shear elastic waves by neo-Hookean soft devices. Appl Phys Lett 2015;106:161903.

[59] Galich PI, Rudykh S. Comment on “Disentangling longitudinal and shear elastic waves by neo-Hookean soft devices” [Appl. Phys. Lett. 106, 161903 (2015)]. Appl Phys Lett 2015;107:056101.

[60] Kushwaha MS, Halevi P, Dobrzynski L, Djafari-Rouhani B. Acoustic band structure of periodic elastic composites. Phys Rev Lett 1993;71:2022–5.

[61] Wang Z, Zhang Q, Zhang K, Hu G. Tunable Digital Metamaterial for Broadband Vibration Isolation at Low Frequency. Adv Mater 2016;28:9857–61.

[62] Wang P, Casadei F, Shan S, Weaver JC, Bertoldi K. Harnessing Buckling to Design Tunable Locally Resonant Acoustic Metamaterials. Phys Rev Lett 2014;113:014301.

[63] Maurin F, Claeys C, Deckers E, Desmet W. Probability that a band-gap extremum is located on the irreducible Brillouin-zone contour for the 17 different plane crystallographic lattices. Int J Solids Struct 2018;135:26–36.

[64] Rytov S. Acoustical properties of a thinly laminated medium. Sov Phys Acoust 1956;2:68–80.

[65] Galich PI, Fang NX, Boyce MC, Rudykh S. Elastic wave propagation in finitely deformed layered materials. J Mech Phys Solids 2017;98:390–410.

[66] Slesarenko V, Galich PI, Li J, Fang NX, Rudykh S. Foreshadowing elastic instabilities by negative group velocity in soft composites. Appl Phys Lett 2018;113:031901.

[67] Bertoldi K, Boyce MC. Mechanically triggered transformations of phononic band gaps in periodic elastomeric structures. Phys Rev B 2008;77:052105.

[68] Bertoldi K, Boyce MC. Wave propagation and instabilities in monolithic and periodically structured elastomeric materials undergoing large deformations. Phys Rev B 2008;78:184107.

[69] Wang P, Shim J, Bertoldi K. Effects of geometric and material nonlinearities on tunable band gaps and low-frequency directionality of phononic crystals. Phys Rev B 2013;88:014304.

[70] Ogden RW. Non-linear Elastic Deformations. New York: Dover Publications; 1997.

[71] Bertoldi K, Boyce MC, Deschanel S, Prange SM, Mullin T. Mechanics of deformation-triggered pattern transformations and superelastic behavior in periodic elastomeric structures. J Mech Phys Solids 2008;56:2642–68.

[72] Babaee S, Viard N, Wang P, Fang NX, Bertoldi K. Harnessing Deformation to Switch On and Off the Propagation of Sound. Adv Mater 2016;28:1631–5.

[73] Bigoni D, Guenneau S, Movchan AB, Brun M. Elastic metamaterials with inertial locally resonant structures: Application to lensing and localization. Phys Rev B 2013;87:174303.

[74] Xu J, Jiang X, Fang N, Georget E, Abdeddaim R, Geffrin JM, et al. Molding acoustic, electromagnetic and water waves with a single cloak. Sci Rep 2015;5:10678.

[75] Zhu R, Liu XN, Hu GK, Sun CT, Huang GL. Negative refraction of elastic waves at the deep-subwavelength scale in a single-phase metamaterial. Nat Commun 2014;5:1–8.

[76] Zigoneanu L, Popa BI, Cummer SA. Three-dimensional broadband omnidirectional acoustic ground cloak. Nat Mater 2014;13:352–5.

[77] Harne RL, Urbanek DC. Enhancing Broadband Vibration Energy Suppression Using Local Buckling Modes in Constrained Metamaterials. J Vib Acoust 2017;139:061004.

[78] Celli P, Gonella S. Manipulating waves with LEGO ® bricks: A versatile experimental platform for metamaterial architectures. Appl Phys Lett 2015;107:081901.

[79] Celli P, Gonella S, Tajeddini V, Muliana A, Ahmed S, Ounaies Z. Wave control through soft microstructural curling: bandgap shifting, reconfigurable anisotropy and switchable chirality. Smart Mater Struct 2017;26:035001.

[80] Chen Q, Elbanna A. Modulating Elastic Band Gap Structure in Layered Soft Composites Using Sacrificial Interfaces. J Appl Mech 2016;83:111009.

[81] Chen Y, Wang L. Bio-inspired heterogeneous composites for broadband vibration mitigation. Sci Rep 2016;5:17865.

[82] Matlack KH, Bauhofer A, Krödel S, Palermo A, Daraio C. Composite 3D-printed metastructures for low-frequency and broadband vibration absorption. Proc Natl Acad Sci 2016;113:8386–90.

[83] Miniaci M, Krushynska A, Movchan AB, Bosia F, Pugno NM. Spider web-inspired acoustic metamaterials. Appl Phys Lett 2016;109:071905.

[84] Srivastava A. Metamaterial properties of periodic laminates. J Mech Phys Solids 2016;96:252–63.

[85] Trainiti G, Rimoli JJ, Ruzzene M. Wave propagation in undulated structural lattices. Int J Solids Struct 2016;97–98:431–44.

[86] Casadei F, Delpero T, Bergamini A, Ermanni P, Ruzzene M. Piezoelectric resonator arrays for tunable acoustic waveguides and metamaterials. J Appl Phys 2012;112.

[87] Javid F, Wang P, Shanian A, Bertoldi K. Architected Materials with Ultra-Low Porosity for Vibration Control. Adv Mater 2016;28:5943–8.

[88] Zhang S, Xia C, Fang N. Broadband Acoustic Cloak for Ultrasound Waves. Phys Rev Lett 2011;106:024301.

[89] Wood B, Pendry JB, Tsai DP. Directed subwavelength imaging using a layered metal-dielectric system. Phys Rev B 2006;74:115116.

[90] Zhu J, Christensen J, Jung J, Martin-Moreno L, Yin X, Fok L, et al. A holey-structured metamaterial for acoustic deep-subwavelength imaging. Nat Phys 2011;7:52–5.

[91] Zhang P, Parnell WJ. Band Gap Formation and Tunability in Stretchable Serpentine Interconnects. J Appl Mech 2017;84:091007.

[92] dell'Isola F, Giorgio I, Pawlikowski M, Rizzi NL. Large deformations of planar extensible beams and pantographic lattices: heuristic homogenization, experimental and numerical examples of equilibrium. Proc R Soc A Math Phys Eng Sci 2016;472:20150790.

[93] Li GY, Zheng Y, Cao YP, Feng XQ, Zhang WY. Controlling elastic wave propagation in a soft bilayer system via wrinkling-induced stress patterns. Soft Matter 2016;12:4204–13.

[94] Meaud J, Che K. Tuning elastic wave propagation in multistable architected materials. Int J Solids Struct 2017;122–123:69–80.

[95] Gei M, Roccabianca S, Bacca M. Controlling bandgap in electroactive polymer-based structures. IEEE/ASME Trans Mechatronics 2011;16:102–7.

[96] Bayat A, Gordaninejad F. Band-Gap of a Soft Magnetorheological Phononic Crystal. J Vib Acoust 2015;137:011013.

[97] Galich PI, Rudykh S. Manipulating pressure and shear waves in dielectric elastomers via external electric stimuli. Int J Solids Struct 2016;91:18–25.

[98] Galich PI, Rudykh S. Shear Wave Propagation and Band Gaps in Finitely Deformed Dielectric Elastomer Laminates: Long Wave Estimates and Exact Solution. J Appl Mech 2017;84:091002.

[99] Jandron MA, Henann D. Exploring phononic crystal tunability using dielectric elastomers. J Acoust Soc Am 2017;141:3743.

[100] Yang WP, Chen LW. The tunable acoustic band gaps of two-dimensional phononic crystals with a dielectric elastomer cylindrical actuator. Smart Mater Struct 2008;17:015011.

[101] Huang Y, Zhang CL, Chen WQ. Tuning Band Structures of Two-Dimensional Phononic Crystals With Biasing Fields. J Appl Mech 2014;81:091008.

[102] Rudykh S, Boyce MC. Transforming Wave Propagation in Layered Media via Instability-Induced Interfacial Wrinkling. Phys Rev Lett 2014;112:034301.

[103] Merodio J, Ogden RW. Mechanical response of fiber-reinforced incompressible non-linearly elastic solids. Int J Non Linear Mech 2005;40:213–27.

[104] Rudykh S, DeBotton G. Instabilities of Hyperelastic Fiber Composites: Micromechanical Versus Numerical Analyses. J Elast 2012;106:123–47.

[105] Agoras M, Lopez-Pamies O, Ponte Castañeda P. Onset of macroscopic instabilities in fiber-reinforced elastomers at finite strain. J Mech Phys Solids 2009;57:1828–50.

[106] Gao C, Li Y. Tuning the wrinkling patterns of an interfacial/coating layer via a regulation interphase. Int J Solids Struct 2017;104–105:92–102.

[107] Galich PI, Slesarenko V, Li J, Rudykh S. Elastic instabilities and shear waves in hyperelastic composites with various periodic fiber arrangements. Int J Eng Sci 2018;130:51–61.

[108] Wu ML, Wu LY, Yang WP, Chen LW. Elastic wave band gaps of one-dimensional phononic crystals with functionally graded materials. Smart Mater Struct 2009;18:115013.

[109] Fomenko SI, Golub M V., Zhang C, Bui TQ, Wang YS. In-plane elastic wave propagation and band-gaps in layered functionally graded phononic crystals. Int J Solids Struct 2014;51:2491–503.

[110] Galich PI, Slesarenko V, Rudykh S. Shear wave propagation in finitely deformed 3D fiber-reinforced composites. Int J Solids Struct 2017;110–111:294–304.

[111] Shang X, Lakes RS. Stability of elastic material with negative stiffness and negative Poisson’s ratio. Phys Status Solidi Basic Res 2007;244:1008–26.

[112] Sammak PJ, Borisy GG. Direct observation of microtubule dynamics in living cells. Nature 1988;332:724–6.

[113] Brangwynne CP, MacKintosh FC, Kumar S, Geisse NA, Talbot J, Mahadevan L, et al. Microtubules can bear enhanced compressive loads in living cells because of lateral reinforcement. J Cell Biol 2006;173:733–41.

[114] Kringelbach ML, Jenkinson N, Owen SLF, Aziz TZ. Translational principles of deep brain stimulation. Nat Rev Neurosci 2007;8:623–35.

[115] L'Heureux N, Pâquet S, Labbé R, Germain L, Auger FA. A completely biological tissue-engineered human blood vessel. FASEB J 1998;12:47–56.

[116] Ku H, Wang H, Pattarachaiyakoop N, Trada M. A review on the tensile properties of natural fiber reinforced polymer composites. Compos Part B Eng 2011;42:856–73.

[117] Li W, Cai H, Li C, Wang K, Fang L. Micro-mechanics of failure for fatigue strength prediction of bolted joint structures of carbon fiber reinforced polymer composite. Compos Struct 2015;124:345–56.

[118] Spackman CC, Frank CR, Picha KC, Samuel J. 3D printing of fiber-reinforced soft composites: Process study and material characterization. J Manuf Process 2016;23:296–305.

[119] Beloshenko V, Voznyak Y, Voznyak A, Savchenko B. New approach to production of fiber reinforced polymer hybrid composites. Compos Part B Eng 2017;112:22–30.

[120] Shan WL, Chen Z, Broedersz CP, Gumaste AA, Soboyejo WO, Brangwynne CP. Attenuated short wavelength buckling and force propagation in a biopolymer-reinforced rod. Soft Matter 2013;9:194–9.

[121] Zhao Y, Li J, Cao YP, Feng XQ. Buckling of an elastic fiber with finite length in a soft matrix. Soft Matter 2016;12:2086–94.

[122] Andrianov I V., Kalamkarov AL, Weichert D. Buckling of fibers in fiber-reinforced composites. Compos Part B Eng 2012;43:2058–62.

[123] Lu H, Li J, Nie C, Duan B, Yin W, Yao Y, et al. Study on buckling response in electrospun fiber with periodic structure. Compos Part B Eng 2017;113:270–7.

[124] Greco F, Lonetti P, Luciano R, Nevone Blasi P, Pranno A. Nonlinear effects in fracture induced failure of compressively loaded fiber reinforced composites. Compos Struct 2018;189:688–99.

[125] Kong XY, Wang ZL. Spontaneous Polarization-Induced Nanohelixes, Nanosprings, and Nanorings of Piezoelectric Nanobelts. Nano Lett 2003;3:1625–31.

[126] Silverberg JL, Noar RD, Packer MS, Harrison MJ, Henley CL, Cohen I, et al. 3D imaging and mechanical modeling of helical buckling in Medicago truncatula plant roots. Proc Natl Acad Sci 2012;109:16794–9.

[127] Herrmann LR, Mason WE, Chan STK. Response of Reinforcing Wires to Compressive States of Stress. J Compos Mater 1967;1:212–26.

[128] Su T, Liu J, Terwagne D, Reis PM, Bertoldi K. Buckling of an elastic rod embedded on an elastomeric matrix: planar vs. non-planar configurations. Soft Matter 2014;10:6294–302.

[129] Chen Y, Liao X, Liu Y, Chen X. Helical buckling of wires embedded in a soft matrix under axial compression. Extrem Mech Lett 2017;17:71–6.

[130] Winkler E. Die Lehre von der Elastizität und Festigkeit. Verlag H. Dominikus, Prag; 1867.

[131] Greco F, Leonetti L, Medaglia CM, Penna R, Pranno A. Nonlinear compressive failure analysis of biaxially loaded fiber reinforced materials. Compos Part B Eng 2018;147:240–51.

[132] Merodio J, Haughton DM. Bifurcation of thick-walled cylindrical shells and the mechanical response of arterial tissue affected by Marfan’s syndrome. Mech Res Commun 2010;37:1–6.

[133] Haughton DM, Merodio J. The elasticity of arterial tissue affected by Marfan’s syndrome. Mech Res Commun 2009;36:659–68.

[134] Timoshenko SP, Gere JM. Theory of Elastic Stability. 2nd ed. New York: McGraw-Hill; 1961.

[135] Goshkoderia A, Rudykh S. Electromechanical macroscopic instabilities in soft dielectric elastomer composites with periodic microstructures. Eur J Mech A/Solids 2017;65:243–56.

[136] Balakrisnan B, Nacev A, Smela E. Design of bending multi-layer electroactive polymer actuators. Smart Mater Struct 2015;24:045032.

[137] Ciambella J, Stanier DC, Rahatekar SS. Magnetic alignment of short carbon fibres in curing composites. Compos Part B Eng 2017;109:129–37.

[138] Psarra E, Bodelot L, Danas K. Two-field surface pattern control via marginally stable magnetorheological elastomers. Soft Matter 2017;13:6576–84.

[139] Ciambella J, Favata A, Tomassetti G. A nonlinear theory for fibre-reinforced magneto-elastic rods. Proc R Soc A Math Phys Eng Sci 2018;474:20170703.

[140] Goshkoderia A, Rudykh S. Stability of magnetoactive composites with periodic microstructures undergoing finite strains in the presence of a magnetic field. Compos Part B Eng 2017;128:19–29.

[141] Che K, Yuan C, Wu J, Qi HJ, Meaud J. Three-Dimensional-Printed Multistable Mechanical Metamaterials With a Deterministic Deformation Sequence. J Appl Mech 2016;84:011004.

[142] Ding Z, Weeger O, Qi HJ, Dunn ML. 4D rods: 3D structures via programmable 1D composite rods. Mater Des 2018;137:256–65.

[143] Yuan C, Roach DJ, Dunn CK, Mu Q, Kuang X, Yakacki CM, et al. 3D printed reversible shape changing soft actuators assisted by liquid crystal elastomers. Soft Matter 2017;13:5558–68.

[144] Kellaris N, Gopaluni Venkata V, Smith GM, Mitchell SK, Keplinger C. Peano-HASEL actuators: Muscle-mimetic, electrohydraulic transducers that linearly contract on activation. Sci Robot 2018;3:eaar3276.

[145] Yu K, Fang NX, Huang G, Wang Q. Magnetoactive Acoustic Metamaterials. Adv Mater 2018;30:1706348.

[146] Tipton CR, Han E, Mullin T. Magneto-elastic buckling of a soft cellular solid. Soft Matter 2012;8:6880.

[147] Wang Z, Li K, He Q, Cai S. A Light-Powered Ultralight Tensegrity Robot with High Deformability and Load Capacity. Adv Mater 2018:1806849.

[148] Liu J, Gu T, Shan S, Kang SH, Weaver JC, Bertoldi K. Harnessing Buckling to Design Architected Materials that Exhibit Effective Negative Swelling. Adv Mater 2016;28:6619–24.

[149] Tang Y, Lin G, Han L, Qiu S, Yang S, Yin J. Design of Hierarchically Cut Hinges for Highly Stretchable and Reconfigurable Metamaterials with Enhanced Strength. Adv Mater 2015;27:7181–90.

[150] Lee DW, Lee JH, Jin JH. Innovative evolution of buckling structures for flexible electronics. Compos Struct 2018;204:487–99.

[151] Guo X, Wang X, Ou D, Ye J, Pang W, Huang Y, et al. Controlled mechanical assembly of complex 3D mesostructures and strain sensors by tensile buckling. Npj Flex Electron 2018;2:14.

[152] Xu S, Yan Z, Jang KI, Huang W, Fu H, Kim J, et al. Assembly of micro/nanomaterials into complex, three-dimensional architectures by compressive buckling. Science 2015;347:154–9.

[153] Zarek M, Layani M, Cooperstein I, Sachyani E, Cohn D, Magdassi S. 3D Printing of Shape Memory Polymers for Flexible Electronic Devices. Adv Mater 2016;28:4449–54.

[154] Krishnan D, Johnson HT. Optical properties of two-dimensional polymer photonic crystals after deformation-induced pattern transformations. J Mech Phys Solids 2009;57:1500–13.

[155] Raney JR, Nadkarni N, Daraio C, Kochmann DM, Lewis JA, Bertoldi K. Stable propagation of mechanical signals in soft media using stored elastic energy. Proc Natl Acad Sci 2016;113:9722–7.

[156] Deng B, Raney JR, Tournat V, Bertoldi K. Elastic Vector Solitons in Soft Architected Materials. Phys Rev Lett 2017;118:204102.

[157] Guttag M, Boyce MC. Locally and Dynamically Controllable Surface Topography Through the Use of Particle-Enhanced Soft Composites. Adv Funct Mater 2015;25:3641–7.

[158] Chen T, Bilal OR, Shea K, Daraio C. Harnessing bistability for directional propulsion of soft, untethered robots. Proc Natl Acad Sci 2018;115:5698–702.

[159] Bertoldi K, Reis PM, Willshaw S, Mullin T. Negative Poisson's Ratio Behavior Induced by an Elastic Instability. Adv Mater 2010;22:361–6.

[160] Li J, Shim J, Deng J, Overvelde JTB, Zhu X, Bertoldi K, et al. Switching periodic membranes via pattern transformation and shape memory effect. Soft Matter 2012;8:10322.

[161] Gao C, Hasseldine BPJ, Li L, Weaver JC, Li Y. Amplifying Strength, Toughness, and Auxeticity via Wavy Sutural Tessellation in Plant Seedcoats. Adv Mater 2018;30:1800579.

[162] Ball JM, James RD. Fine phase mixtures as minimizers of energy. Arch Ration Mech Anal 1987;100:13–52.

[163] Bhattacharya K. Microstructure of Martensite: Why it forms and how it gives rise to the shape–memory effect. New York: Oxford University Press; 2003.

[164] Blinov LM. Domain instabilities in liquid crystals. Le J Phys Colloq 1979;40:247.

[165] Tran L, Lavrentovich MO, Durey G, Darmon A, Haase MF, Li N, et al. Change in Stripes for Cholesteric Shells via Anchoring in Moderation. Phys Rev X 2017;7:041029.

[166] DeSimone A, Dolzmann G. Material instabilities in nematic elastomers. Phys D Nonlinear Phenom 2000;136:175–91.

[167] Conti S. Soft elastic response of stretched sheets of nematic elastomers: a numerical study. J Mech Phys Solids 2002;50:1431–51.

[168] Chen X, Hutchinson JW. Herringbone Buckling Patterns of Compressed Thin Films on Compliant Substrates. J Appl Mech 2004;71:597.

[169] Cai S, Breid D, Crosby AJ, Suo Z, Hutchinson JW. Periodic patterns and energy states of buckled films on compliant substrates. J Mech Phys Solids 2011;59:1094–114.

[170] Yin J, Yagüe JL, Eggenspieler D, Gleason KK, Boyce MC. Deterministic Order in Surface Micro-Topologies through Sequential Wrinkling. Adv Mater 2012;24:5441–6.

[171] Furer J, Ponte Castañeda P. Macroscopic instabilities and domain formation in neo-Hookean laminates. J Mech Phys Solids 2018;118:98–114.

[172] Zheng Z, Zola RS, Bisoyi HK, Wang L, Li Y, Bunning TJ, et al. Controllable Dynamic Zigzag Pattern Formation in a Soft Helical Superstructure. Adv Mater 2017;29:1701903.

[173] Wang W, Timonen JVI, Carlson A, Drotlef DM, Zhang CT, Kolle S, et al. Multifunctional ferrofluid-infused surfaces with reconfigurable multiscale topography. Nature 2018;559:77–82.

[174] Zhao Z, Kuang X, Yuan C, Qi HJ, Fang D. Hydrophilic/Hydrophobic Composite Shape-Shifting Structures. ACS Appl Mater Interfaces 2018;10:19932–9.

[175] Milton GW. Composite materials with poisson’s ratios close to - 1. J Mech Phys Solids 1992;40:1105–37.

[176] Che K, Yuan C, Qi HJ, Meaud J. Viscoelastic multistable architected materials with temperature-dependent snapping sequence. Soft Matter 2018;14:2492–9.

[177] Argatov II, Guinovart-Díaz R, Sabina FJ. On local indentation and impact compliance of isotropic auxetic materials from the continuum mechanics viewpoint. Int J Eng Sci 2012;54:42–57.

[178] Imbalzano G, Linforth S, Ngo TD, Lee PVS, Tran P. Blast resistance of auxetic and honeycomb sandwich panels: Comparisons and parametric designs. Compos Struct 2018;183:242–61.

[179] Alderson A, Rasburn J, Ameer-Beg S, Mullarkey PG, Perrie W, Evans KE. An Auxetic Filter: A Tuneable Filter Displaying Enhanced Size Selectivity or Defouling Properties. Ind Eng Chem Res 2000;39:654–65.

[180] Grimmelsmann N, Meissner H, Ehrmann A. 3D printed auxetic forms on knitted fabrics for adjustable permeability and mechanical properties. IOP Conf Ser Mater Sci Eng 2016;137:012011.

[181] Hou S, Liu T, Zhang Z, Han X, Li Q. How does negative Poisson’s ratio of foam filler affect crashworthiness? Mater Des 2015;82:247–59.

[182] LAKES R. Foam Structures with a Negative Poisson’s Ratio. Science 1987;100:1038–40.

[183] Sanami M, Ravirala N, Alderson K, Alderson A. Auxetic Materials for Sports Applications. Procedia Eng 2014;72:453–8.

[184] Zhang SL, Lai YC, He X, Liu R, Zi Y, Wang ZL. Auxetic Foam-Based Contact-Mode Triboelectric Nanogenerator with Highly Sensitive Self-Powered Strain Sensing Capabilities to Monitor Human Body Movement. Adv Funct Mater 2017;27:1606695.

[185] Alderson A, Rasburn J, Evans KE, Grima JN. Auxetic polymeric filters display enhanced de-fouling and pressure compensation properties. Membr Technol 2001;2001:6–8.

[186] Kuribayashi K, Tsuchiya K, You Z, Tomus D, Umemoto M, Ito T, et al. Self-deployable origami stent grafts as a biomedical application of Ni-rich TiNi shape memory alloy foil. Mater Sci Eng A 2006;419:131–7.

[187] Ren X, Shen J, Tran P, Ngo TD, Xie YM. Auxetic nail: Design and experimental study. Compos Struct 2018;184:288–98.

[188] Papadopoulou A, Laucks J, Tibbits S. Auxetic materials in design and architecture. Nat Rev Mater 2017;2:17078.

[189] Shan S, Kang SH, Zhao Z, Fang L, Bertoldi K. Design of planar isotropic negative Poisson’s ratio structures. Extrem Mech Lett 2015;4:96–102.

[190] Gatt R, Mizzi L, Azzopardi JI, Azzopardi KM, Attard D, Casha A, et al. Hierarchical Auxetic Mechanical Metamaterials. Sci Rep 2015;5:8395.

[191] Taylor M, Francesconi L, Gerendás M, Shanian A, Carson C, Bertoldi K. Low Porosity Metallic Periodic Structures with Negative Poisson’s Ratio. Adv Mater 2014;26:2365–70.

[192] Grima JN, Gatt R. Perforated Sheets Exhibiting Negative Poisson’s Ratios. Adv Eng Mater 2010;12:460–4.

[193] Grima JN, Gatt R, Ellul B, Chetcuti E. Auxetic behaviour in non-crystalline materials having star or triangular shaped perforations. J Non Cryst Solids 2010;356:1980–7.

[194] Mizzi L, Azzopardi KM, Attard D, Grima JN, Gatt R. Auxetic metamaterials exhibiting giant negative Poisson’s ratios. Phys Status Solidi - Rapid Res Lett 2015;9:425–30.

[195] Grima JN, Mizzi L, Azzopardi KM, Gatt R. Auxetic Perforated Mechanical Metamaterials with Randomly Oriented Cuts. Adv Mater 2016;28:385–9.

[196] Jiang Y, Li Y. Novel 3D-Printed Hybrid Auxetic Mechanical Metamaterial with Chirality-Induced Sequential Cell Opening Mechanisms. Adv Eng Mater 2018;20:1700744.

[197] Cho H, Weaver JC, Pöselt E, in't Veld PJ, Boyce MC, Rutledge GC. Engineering the Mechanics of Heterogeneous Soft Crystals. Adv Funct Mater 2016;26:6938–49.

[198] Slesarenko V, Rudykh S. Towards mechanical characterization of soft digital materials for multimaterial 3D-printing. Int J Eng Sci 2018;123:62–72.

[199] Frenzel T, Kadic M, Wegener M. Three-dimensional mechanical metamaterials with a twist. Science 2017;358:1072–4.

[200] Sun CT, Vaidya RS. Prediction of composite properties from a representative volume element. Compos Sci Technol 1996;56:171–9.

[201] Krushynska AO, Kouznetsova VG, Geers MGD. Visco-elastic effects on wave dispersion in three-phase acoustic metamaterials. J Mech Phys Solids 2016;96:29–47.

[202] Lewińska MA, Kouznetsova VG, van Dommelen JAW, Krushynska AO, Geers MGD. The attenuation performance of locally resonant acoustic metamaterials based on generalised viscoelastic modelling. Int J Solids Struct 2017;126–127:163–74.

[203] Liu R, Kuang X, Deng J, Wang YC, Wang AC, Ding W, et al. Shape Memory Polymers for Body Motion Energy Harvesting and Self-Powered Mechanosensing. Adv Mater 2018;30:1705195.

[204] Patel DK, Sakhaei AH, Layani M, Zhang B, Ge Q, Magdassi S. Highly Stretchable and UV Curable Elastomers for Digital Light Processing Based 3D Printing. Adv Mater 2017;29:1606000.

[205] Mosadegh B, Polygerinos P, Keplinger C, Wennstedt S, Shepherd RF, Gupta U, et al. Pneumatic Networks for Soft Robotics that Actuate Rapidly. Adv Funct Mater 2014;24:2163–70.

[206] Deng J, Kuang X, Liu R, Ding W, Wang AC, Lai YC, et al. Vitrimer Elastomer-Based Jigsaw Puzzle-Like Healable Triboelectric Nanogenerator for Self-Powered Wearable Electronics. Adv Mater 2018;30:1705918.

[207] Lau K, Hung PY, Zhu MH, Hui D. Properties of natural fibre composites for structural engineering applications. Compos Part B Eng 2018;136:222–33.

[208] Compton BG, Lewis JA. 3D-Printing of Lightweight Cellular Composites. Adv Mater 2014;26:5930–5.

[209] Mohan VB, Lau K, Hui D, Bhattacharyya D. Graphene-based materials and their composites: A review on production, applications and product limitations. Compos Part B Eng 2018;142:200–20.

[210] Scarponi C, Messano M. Comparative evaluation between E-Glass and hemp fiber composites application in rotorcraft interiors. Compos Part B Eng 2015;69:542–9.

[211] Rafsanjani A, Akbarzadeh A, Pasini D. Snapping Mechanical Metamaterials under Tension. Adv Mater 2015;27:5931–5.

[212] Michel JC, Lopez-Pamies O, Ponte Castañeda P, Triantafyllidis N. Microscopic and macroscopic instabilities in finitely strained porous elastomers. J Mech Phys Solids 2007;55:900–38.

[213] Yan J, Han M, Zhang J, Xu C, Luijten E, Granick S. Reconfiguring active particles by electrostatic imbalance. Nat Mater 2016;15:1095–9.

[214] Gao C, Slesarenko V, Boyce MC, Rudykh S, Li Y. Instability-Induced Pattern Transformation in Soft Metamaterial with Hexagonal Networks for Tunable Wave Propagation. Sci Rep 2018;8:11834.

[215] Gao N, Li J, Bao R, Chen W. Harnessing uniaxial tension to tune Poisson's ratio and wave propagation in soft porous phononic crystals: an experimental study. Soft Matter 2019.

[216] Destrade M, Ogden RW. On stress-dependent elastic moduli and wave speeds. IMA J Appl Math 2013;78:965–97.

[217] Nam NT, Merodio J, Ogden RW, Vinh PC. The effect of initial stress on the propagation of surface waves in a layered half-space. Int J Solids Struct 2016;88–89:88–100.

[218] Kolle M, Lethbridge A, Kreysing M, Baumberg JJ, Aizenberg J, Vukusic P. Bio-Inspired Band-Gap Tunable Elastic Optical Multilayer Fibers. Adv Mater 2013;25:2239–45.

[219] Rudykh S, Ortiz C, Boyce MC. Flexibility and protection by design: imbricated hybrid microstructures of bio-inspired armor. Soft Matter 2015;11:2547–54.

[220] Slesarenko V, Kazarinov N, Rudykh S. Distinct failure modes in bio-inspired 3D-printed staggered composites under non-aligned loadings. Smart Mater Struct 2017;26:035053.

[221] Boulanger P, Hayes M, Trimarco C. Finite-amplitude plane waves in deformed Hadamard elastic materials. Geophys J Int 1994;118:447–58.

[222] Vinh PC, Merodio J. On acoustoelasticity and the elastic constantsof soft biological tissues 2013;8:359–367.

[223] Vinh PC, Merodio J, Hue TTT, Nam NT. Non-principal Rayleigh waves in deformed transversely isotropic incompressible non-linearly elastic solids. IMA J Appl Math 2014;79:915–28.

[224] Nam NT, Merodio J, Vinh PC. International Journal of Non-Linear Mechanics The secular equation for non-principal Rayleigh waves in deformed incompressible doubly fiber-reinforced nonlinearly elastic solids. Int J Non Linear Mech 2016;84:23–30.

[225] Schneider D, Liaqat F, El Boudouti EH, El Hassouani Y, Djafari-Rouhani B, Tremel W, et al. Engineering the Hypersonic Phononic Band Gap of Hybrid Bragg Stacks. Nano Lett 2012;12:3101–8.

[226] Zhang P, Parnell WJ. Soft phononic crystals with deformation-independent band gaps. Proc R Soc A Math Phys Eng Sci 2017;473:20160865.

[227] Spiegel MR, Lipschutz S, Liu J. Mathematical handbook of formulas and tables. 2nd ed., McGraw-Hill; 1998, p. 137–9.

[228] Abramowitz M, Stegun I. Handbook of mathematical functions with Formulas, Graphs, and Mathematical Tables, National Institute of Standards and Technology; 1964, p. 375.